

## TOPICAL REVIEW

# Electromagnetic reactions on light nuclei

Sonia Bacca<sup>1,2</sup> and Saori Pastore<sup>3</sup>

<sup>1</sup>TRIUMF, 4004 Wesbrook Mall, Vancouver, BC, V6T 2A3, Canada

<sup>2</sup>Department of Physics and Astronomy, University of Manitoba, Winnipeg, MB, R3T 2N2, Canada

<sup>3</sup>Department of Physics and Astronomy, University of South Carolina, Columbia, SC 29208, USA

E-mail: bacca@triumf.ca, pastores@mailbox.sc.edu

**Abstract.** Electromagnetic reactions on light nuclei are fundamental to advance our understanding of nuclear structure and dynamics. The perturbative nature of the electromagnetic probes allows to clearly connect measured cross sections with the calculated structure properties of nuclear targets. We present an overview on recent theoretical *ab-initio* calculations of electron-scattering and photonuclear reactions involving light nuclei. We encompass both the conventional approach and the novel theoretical framework provided by chiral effective field theories. Because both strong and electromagnetic interactions are involved in the processes under study, comparison with available experimental data provides stringent constraints on both many-body nuclear Hamiltonians and electromagnetic currents. We discuss what we have learned from studies on electromagnetic observables of light nuclei, starting from the deuteron and reaching up to nuclear systems with mass number  $A = 16$ .

Submitted to: *J. Phys. G: Nucl. Phys.*

## Contents

<b>1</b>	<b>Introduction</b>	<b>2</b>
<b>2</b>	<b>Nuclear Hamiltonians and electromagnetic currents</b>	<b>5</b>
2.1	The conventional approach . . . . .	6
2.2	The chiral effective field theory approach . . . . .	10
2.3	Conventions and notations . . . . .	18
<b>3</b>	<b>Electron scattering reactions</b>	<b>19</b>
3.1	Formalism . . . . .	21
3.2	Ground-state properties: electromagnetic moments . . . . .	23
3.3	Ground-state properties: elastic form factors . . . . .	26
3.3.1	The deuteron . . . . .	27
3.3.2	The three-body nuclei . . . . .	30
3.3.3	The <sup>4</sup> He nucleus . . . . .	32
3.3.4	Nuclei with $A > 4$ . . . . .	34
3.4	Inelastic scattering . . . . .	35
3.4.1	The deuteron and the $A = 3$ nuclei . . . . .	36
3.4.2	The <sup>4</sup> He nucleus . . . . .	38
3.4.3	Transition form factors and sum rules in $A > 4$ nuclei . . . . .	42

<b>4</b>	<b>Photonuclear reactions</b>	<b>44</b>
4.1	Photoabsorption reactions . . . . .	44
4.1.1	The deuteron . . . . .	46
4.1.2	The three-body nuclei . . . . .	47
4.1.3	The ${}^4\text{He}$ nucleus . . . . .	49
4.1.4	The $A = 6$ and $7$ nuclei . . . . .	52
4.1.5	Towards medium-mass nuclei . . . . .	54
4.2	Radiative capture reactions . . . . .	55
4.2.1	Systems with $A \leq 4$ . . . . .	56
4.2.2	Systems with $A > 4$ . . . . .	58
4.3	Electromagnetic transitions in low-lying nuclear states . . . . .	60
<b>5</b>	<b>Summary and outlook</b>	<b>62</b>

## 1. Introduction

In this review we report on recent theoretical *ab-initio* calculations of electromagnetic (e.m.) reactions on light nuclei. E.m. reactions are particularly suited to test the extent and predictive power of nuclear theories. In fact, the small e.m. coupling strength, characterized by the fine-structure constant  $\alpha \sim 1/137$ , allows for a perturbative treatment of the e.m. interaction. Contributions beyond the leading order term in the  $Z\alpha$ -expansion, where  $Z$  is the number of protons, that is beyond the Born approximation, are sufficiently small to be safely disregarded in light nuclei. This leaves us with relatively simple reaction mechanisms and with formal expressions for the cross sections in which the nuclear structure content can be easily isolated from the well know one associated with the external structureless probes [1–3]. In many cases, experimental data of e.m. observables can be accessed with great accuracy, providing us with stringent constraints on nuclear models. A theoretical understanding and control of nuclear e.m. structure and dynamics is a necessary prerequisite for studies on weak induced reactions. The experimental data acquisition for this kind of processes is comparatively more involved owing to the tinier cross sections and to the fact that neutrinos are chargeless particles and, thus, they are hard to collimate and detect. Therefore, in order to address important issues, such as the recently observed anomaly in the measured cross section of quasi-elastic neutrino scattering off  ${}^{12}\text{C}$  [4], it is imperative to first validate our theoretical understanding of e.m. reactions on light nuclei.

In this review we discuss mainly electron scattering reactions and photonuclear reactions as possible doorways to access nuclear properties. Alternative e.m. reactions, very useful especially in the case of exotic nuclei, are, *e.g.*, Coulomb scattering processes. We refer to them in a few instances, and redirect the reader to dedicated reviews (see, *e.g.*, Ref. [5] for more details).

In the Born approximation for the electron and photonuclear cross sections, the single photon exchanged transfers a four-momentum  $q^\mu = (\omega, \mathbf{q})$  to the target nucleus (with  $\omega = |\mathbf{q}|$ , for real photons)<sup>†</sup>. Photons, then, probe the e.m. charge and current distributions of nuclei with spatial resolution  $\propto 1/|\mathbf{q}|$ . In this review, we are concerned with processes occurring below the pion production threshold, that is we consider transferred energies  $\omega < m_\pi$ , where  $m_\pi \sim 140$  MeV is the pion mass. At these energies, pions only appear as virtual particles being exchanged among nucleons. Ground-states properties, such as nuclear elastic form factors, are accessed via elastic electron-scattering reactions (where  $\omega = 0$ ). Observables

<sup>†</sup> Here and in what follows we use the convention  $\hbar = c = 1$ .

associated with inelastic processes (where  $\omega \neq 0$ ) are, for example, e.m. transition strengths and inelastic response functions. Other interesting e.m. processes, not covered in the present review, are, for example, Compton scattering reactions on light nuclei, for which we refer the reader to the review article of Ref. [6].

In the theoretical framework we discuss, commonly referred to as *ab-initio*, nuclei are described in terms of point-like nucleons interacting among themselves via many-body forces. Nuclear forces are in practice phenomenological, in that they are constructed so as to reproduce available experimental data. For example, nucleon-nucleon (NN) potentials invoke parameters which are fitted, with a  $\chi^2/\text{datum}$  close to one, to a wide number of NN scattering data and to the deuteron binding energy. Potentials fulfilling the characteristics outlined above are called realistic. Most of the potentials utilized in the calculations we present explicitly include one-pion exchange (OPE) mechanisms to describe the long-range part of the nuclear interaction, and, while being phase-shift equivalent, they implement different schemes to parametrize the intermediate- and short-range parts, including multiple-pion or heavy-meson exchanges [7]. In view of their crucial role in reproducing the energy spectrum of light nuclei, three-nucleon (3N) forces are accounted for in most of the results we present. Models for 3N potentials involve, for example, multiple-meson exchanges and virtual excitations of nucleonic degrees of freedom, *e.g.*,  $\Delta$ -resonances [7].

We discuss non-relativistic theoretical frameworks (for recent reviews on relativistic calculations of e.m. properties of  $A = 2$  and 3 nuclei see, *e.g.*, Refs. [8–10] and references therein). Nuclear wave functions are then solutions of the Schrödinger equation with a Hamiltonian consisting of the sum of the nucleons' kinetic energies along with NN and 3N potentials. The average nucleon velocity, for example, in  $A = 8$  nuclei is of the order of  $\sim 0.2$ . This motivates the non-relativistic description of nuclear systems. Relativistic effects are taken into account as kinematic corrections to the non-relativistic nuclear operators that act on the nuclear wave functions, and they are given by higher order terms in the  $|\mathbf{p}|/m$  expansion of the corresponding covariant operators, where  $\mathbf{p}$  and  $m$  are the nucleon's momentum and mass, respectively.

Implicit in the definition of *ab-initio* calculations is the requirement that the computational methods utilized to solve the many-body Schrödinger equation provide solutions that are numerically exact or obtained within controlled approximation schemes.

Within the microscopic description outlined above, nuclear e.m. currents are also expressed as an expansion in many-body operators. The major contribution to this expansion is provided by the non-relativistic single-nucleon e.m. current operator, referred to as the non-relativistic Impulse Approximation (IA) operator. Thus, in the limit of  $|\mathbf{q}| \rightarrow 0$ , the time-like component of the nuclear e.m. current reduces to the protons' charges inside the nucleus to give the total nuclear charge, while the space-like component consists of the single-nucleon vector current generated by moving protons (convection current) and that associated with the nucleons' spins (spin-magnetization current).

Nuclear e.m. currents and nuclear potentials are linked by the continuity equation, resulting from the gauge invariance of the theory, and expressing that the charge is a conserved quantity. For example, to the long-range OPE part of the NN interaction correspond two-body OPE e.m. currents, which involve a photon interacting with virtual pions being exchanged among the nucleons in a pair. Currents relying on meson-exchange mechanisms are called meson-exchange currents (MEC). The seminal derivations of MEC corrections date back to the late '40s, and were carried out by Villars in Ref. [11] and Miyazawa in Ref. [12] for nuclear static magnetic moments. The 1972 work by Riska and Brown [13] provided the first strong evidence for the need to incorporate two-body OPE e.m. currents, in addition to the IA terms. That study was focused on evaluating the cross section of thermal neutron

radiative capture on proton, and MEC contributions were found to provide the missing  $\sim 10\%$  correction required to reach agreement with the experimental datum. MEC have been widely studied to high levels of sophistication and accuracy (see, for example, Refs. [14–20] for early developments on the topic). In their most recent formulation, described, for example, in Refs. [21, 22] and references therein, MEC include, in addition to the standard convection and spin-magnetization single-nucleon operators, two- and three-body components constructed from NN and 3N nuclear potentials so as to satisfy the continuity equation. This ensures that e.m. currents and nuclear interactions are consistent in describing the short and intermediate range dynamics. The continuity equation does not uniquely constrain components of e.m. currents that are orthogonal to the momentum carried by the external photon field. This introduces a degree of model dependence in that transverse MEC are not uniquely defined.

The theoretical method described above, which is here referred to as the ‘conventional’ approach<sup>†</sup>, has been successfully applied to study a wide variety of nuclear e.m. observables. The most comprehensive review on its application to light nuclei was released in 1998 by Carlson and Schiavilla in Ref. [23]. Since then, a number of additional calculations have appeared in the literature. Among these, we highlight the very recent and computationally demanding *ab-initio* Green’s function Monte Carlo calculations of the  $^{12}\text{C}$  elastic e.m. form factors and sum rules of longitudinal and transverse response functions, that include MEC corrections and 3N forces, carried out by Lovato and collaborators in Ref. [24]. In their study, the calculated MEC contribution to the transverse sum rule is found to significantly increase (by up to  $\sim 50\%$ ) the IA results, corroborating the importance of many-body effects in nuclear systems.

The recent history of few-body nuclear physics has witnessed the tremendous development of chiral effective field theories ( $\chi\text{EFTs}$ ) that systematically describe the interactions of nucleons among themselves and with external electroweak probes.  $\chi\text{EFTs}$  present the advantage of providing a direct connection between the theory of nuclei, expressed in terms of non-relativistic nucleons interacting via many-body potentials, and quantum chromodynamics (QCD), describing the dynamics of the underlying constituents of matter, *i.e.*, quarks and gluons. The effective nuclear Lagrangians are expressed in terms of degrees of freedom which are bound states of QCD, such as nucleons, pions, and  $\Delta$ -isobars, and are constructed so as to preserve all the symmetries, in particular chiral symmetry, exhibited by the underlying theory of QCD in the low-energy regime relevant to nuclear physics. In this energy regime, QCD does not have a simple solution because the strong coupling constant becomes too large and perturbative techniques cannot be applied to solve it. However, chiral symmetry dictates that pions couple among themselves and to other composite degrees of freedom by powers of momenta generically denoted by  $Q$ . The effective Lagrangians describing these interactions can be expanded in powers of  $Q/\Lambda_\chi$ , where  $\Lambda_\chi \sim 1$  GeV represents the chiral-symmetry breaking scale and characterizes the convergence of the expansion. Therefore,  $\chi\text{EFTs}$  provide an expansion of the Lagrangian in powers of a small momentum as opposed to an expansion in the strong coupling constant, restoring, in practice, the possibility of applying perturbative techniques also in the low-energy regime of interest. The coefficients of the chiral expansion are called Low Energy Constants (LECs). They are unknown and need to be fixed by comparison with the experimental data. The transition amplitudes obtained from the effective Lagrangians are also expanded in terms of  $(Q/\Lambda_\chi)^\nu$ . This, in principle, allows to evaluate nuclear observables to any degree  $\nu$  of desired accuracy,

<sup>†</sup> The conventional approach is in the literature often referred to as the ‘Standard Nuclear Physics Approach’ or SNPA.

with an associated theoretical error roughly given by  $(Q/\Lambda_\chi)^{(v+1)}$ .

Since the pioneering work of Weinberg [25–27] released in the early nineties, this calculational scheme has been widely utilized in nuclear physics and nuclear  $\chi$ EFT has developed into an intense and prolific field of research. Here, we focus on calculations of nuclear e.m. observables carried out within  $\chi$ EFT formulations in which pions and nucleons are retained as relevant degrees of freedom, and limit the discussion to reactions occurring within the low-energy regime of applicability of the theory. Nuclear many-body operators constructed from pion and nucleon interactions, involve multiple pion exchange contributions as well as contact-like interaction terms. Heavier degrees of freedom, such as nucleons' excited states and/or heavier mesons, are 'integrated out' and their interactions are implicitly accounted for through the LECs of the theory. Nuclear two- and three-body interactions were first investigated in the late '90s by Ordóñez, Ray, and van Kolck within the standard time ordered perturbation theory framework [28–30]. Currently, chiral NN (3N) potentials commonly used in *ab-initio* calculations include up to next-to-next-to-next-to leading order or N3LO (next-to-next-to leading order or N2LO) corrections in the chiral expansion [31–33]. Work is in progress to explicitly incorporate the  $\Delta$ -isobar among the relevant degrees of freedom of nuclear  $\chi$ EFTs to develop both nuclear potentials (see, *e.g.*, Refs. [34–36]) and e.m. currents (see, *e.g.*, Ref. [37] for preliminary work on this topic). For comprehensive reviews on EFTs applied to few-body nuclear systems we remind, *e.g.*, to Refs. [31–33, 38–43].

Electroweak currents have also been described in  $\chi$ EFT formulations with pions and nucleons. Interactions of nuclei with external electroweak probes have been first studied in covariant perturbation theory by Park, Min, and Rho in Refs. [44, 45], where two-body electroweak current operators have been constructed up to N3LO accuracy, that is up one-loop corrections. More recently,  $\chi$ EFT e.m. currents up to N3LO have been derived within two different implementations of time ordered perturbation theory: one is by the JLab-Pisa group (see Refs. [37, 46–48]) and the other one is by the Bochum-Bonn group (see Refs. [49, 50]). Two-body  $\chi$ EFT e.m. currents have been recently used in a number of *ab-initio* calculations of e.m. observables in  $A = 2$ – $9$  nuclei. These calculations constitute one of the topics discussed in the present review.

With this review we hope to provide a general presentation of *ab-initio* calculations of e.m. observables of nuclear systems with mass number up to  $A = 16$ . Because the scope of this review is rather wide, topics are not covered exhaustively. We focus on investigations developed in the years after the release of the 1998 review by Carlson and Schiavilla [23]. We highlight results (where available) that are comprehensive of many-body components in the e.m. current operators, and results (where available) that use chiral potentials and/or chiral e.m. currents. The emphasis is on comparing theoretical calculations with experimental data. We hope that this review will prove to be a useful and compact report on the present status of theoretical *ab-initio* studies on nuclear e.m. reactions at low-energies.

This review is structured as follows: in Section 2 we briefly present nuclear potentials and e.m. currents commonly utilized in *ab-initio* calculations; Sections 3 and 4 are devoted to electron scattering reactions and e.m. reactions involving real photons, respectively; we summarize and present an outlook in Section 5. In the very last section of this review a list of acronyms and abbreviations is provided.

## 2. Nuclear Hamiltonians and electromagnetic currents

This section is devoted to briefly describe the theoretical framework of *ab-initio* calculations, and we divide it into three subsections. The first one discusses the conventional approach

developed to construct nuclear potentials and consistent e.m. currents. The second one presents nuclear potentials and e.m. currents from a  $\chi$ EFT perspective, in which nuclear dynamics are given in terms of pion and nucleon degrees of freedom. In the last subsection, we define conventions and notations utilized throughout the course of this review.

### 2.1. The conventional approach

Within the *ab-initio* framework, nuclei are conceived as a collection of non-relativistic nucleons interacting via many-body potentials. Thus, nuclear wave functions are solution of the Schrödinger equation

$$H|\Psi_n\rangle = E_n|\Psi_n\rangle, \quad (1)$$

with a nuclear Hamiltonian  $H$  given by

$$H = \sum_i t_i + \sum_{i<j} v_{ij} + \sum_{i<j<k} V_{ijk} + \dots \quad (2)$$

Here,  $t_i$  is the non-relativistic single-nucleon kinetic energy, while  $v_{ij}$  and  $V_{ijk}$  are NN and 3N potentials, respectively. Higher order terms in the many-body expansion are represented by the dots.

Many computational techniques (for a review see, *e.g.*, Ref. [51]) have been developed to obtain accurate solutions of Eq. (1). Methods commonly utilized in  $A \leq 4$  systems rely on the Faddeev decomposition of the Schrödinger equation. Among these are, for example, the Faddeev-Yakubovsky scheme [52] and the hyperspherical harmonics (HH) method [53–58]. A method that can also tackle nuclei with mass number  $A > 4$  is the Lorentz integral transform (LIT) [59, 60] used in combination with the effective interaction hyperspherical harmonics (EIH) expansion [61, 62]. Other powerful and accurate *ab-initio* methods employed to solve the few- and many-body nuclear problem include, for example, Quantum Monte Carlo (QMC) methods [63–68], such as the variational (VMC) and the Green's function Monte Carlo (GFMC) approaches (currently available for  $A \leq 12$  systems), no-core shell model (NCSM) methods [69, 70], coupled-cluster (CC) methods [71–73], and the Fermionic Molecular Dynamics (FMD) approach [74].

Calculations of the energy spectrum of light nuclei show that, while 3N forces are essential to reach agreement with the experimental data, their net contribution is much smaller than that associated with NN forces. For example, in GFMC calculations of  $A = 3 - 8$  nuclei ground-state energies [67], the  $V_{ijk}$  contribution is found to be up to  $\sim 8\%$  of that due to  $v_{ij}$ . The convergence pattern exhibited by the NN and 3N nuclear operators emerges naturally in the chiral expansion of nuclear forces (see next subsection), and 4N forces are predicted to be suppressed with respect to leading 3N forces. 4N forces are neglected in all the results shown here. However, one has to keep in mind that, due to a significant cancellation between the kinetic and the  $v_{ij}$  terms of the nuclear Hamiltonian, 3N forces can provide up to  $\sim 30\%$  of the total calculated energy [67].

The calculations we present use several modern NN and 3N potentials. In particular, at large inter-nucleon distances, they all assume that the NN interaction results from the exchange of one pion among the nucleons, as it is schematically represented by the diagram illustrated in panel (b) of Figure 2 (appearing in the next subsection). In the static limit where  $m \rightarrow \infty$  (a standard approximation utilized in nuclear physics consisting of neglecting nucleonic kinetic energies), evaluation of the transition amplitude associated with this diagram leads to the expression of the standard OPE potential, which in momentum space reads

$$v_\pi(\mathbf{k}) = -\frac{g_A^2}{F_\pi^2} \boldsymbol{\tau}_i \cdot \boldsymbol{\tau}_j \frac{\boldsymbol{\sigma}_i \cdot \mathbf{k} \boldsymbol{\sigma}_j \cdot \mathbf{k}}{\omega_k^2}. \quad (3)$$

In the equation above, the potential is obtained in the center-of-mass frame where the nucleons' initial and final relative momenta are  $\mathbf{p}$  and  $\mathbf{p}'$ , respectively. We also define  $\mathbf{k} = \mathbf{p}' - \mathbf{p}$ , then the energy of the exchanged pion is  $\omega_k = \sqrt{k^2 + m_\pi^2}$ , while  $\sigma_i$  and  $\tau_i$  are the nucleonic spin and isospin Pauli matrices, respectively. The  $\pi NN$  coupling is given in terms of the nucleon axial coupling constant  $g_A \simeq 1.27$  and the pion decay amplitude  $F_\pi \simeq 186$  MeV †.

Intermediate- and short-range components of the NN interaction present a rich structure, which is expressed in terms of nucleonic momenta, spin and isospin operators. Realistic potentials involve a number of parameters that are constrained to fit  $pp$  and  $np$  scattering data up to energies of  $\simeq 350$  MeV in the laboratory frame, along with the binding energy of the deuteron. Common conventional NN potentials describe intermediate- and short-range parts in terms of one-boson exchange contributions, as done in the CD-Bonn potential [75], or parameterizations in terms of operator structures with strengths specified by special functions as done, for example, in the series of Argonne NN potentials whose latest implementation is the Argonne- $v_{18}$  (AV18) version developed in Ref. [76].

Unlike NN potentials, 3N forces are not fixed to 3N scattering data yet. Static properties of few-nucleon systems, such as binding energies, and nuclear-matter saturation properties are instead exploited to constrain them. Then, the values of the fitted parameters entering 3N forces necessarily depend on the particular NN potential utilized in the calculations. For example, 3N forces constructed in combination with the AV18 NN interaction belong to the Urbana series [77], whose latest version is called Urbana IX (UIX), and to the more recently developed Illinois series [78, 79], whose latest implementation is called Illinois-7 (IL7). Both these 3N interactions include the Fujita-Miyazawa term [80, 81]—a two-pion exchange contribution involving the excitation of a virtual  $\Delta$ -isobar—and a short-ranged repulsive phenomenological term [77]. The Illinois interaction adds to the Urbana one the contributions due to an S-wave two-pion exchange term plus so called ring diagrams which involve the exchanges of three pions combined with excitations of one virtual  $\Delta$ -isobar [78, 79]. When used with the AV18 NN and IL7 3N potentials, the final GFMC results reproduce the experimental ground- and excited-state energies for  $A \leq 12$  nuclei very well [67, 79, 82–84].

Nuclear e.m. charge ( $\rho$ ) and current ( $\mathbf{j}$ ) operators—that is the time and vector components of the four-vector current  $j^\mu = (\rho, \mathbf{j})$ —are also expressed as an expansion in many-body operators that act on nucleonic degrees of freedom

$$\begin{aligned} \rho(\mathbf{q}) &= \sum_i \rho_i(\mathbf{q}) + \sum_{i<j} \rho_{ij}(\mathbf{q}) + \dots, \\ \mathbf{j}(\mathbf{q}) &= \sum_i \mathbf{j}_i(\mathbf{q}) + \sum_{i<j} \mathbf{j}_{ij}(\mathbf{q}) + \dots. \end{aligned} \quad (4)$$

Here,  $\mathbf{q}$  is the momentum associated with the external photon field. Calculations in IA performed using one-body operators only are based on the simplified picture in which nuclear properties can be expressed in terms of those associated with free nucleons, *i.e.*, the probing photon interacts with individual nucleons. This kind of contributions is schematically represented by disconnected diagrams such as the one illustrated in panel (a) of Figure 3 (appearing in the next subsection).

One-body e.m. current operators are obtained from the non-relativistic expansion of the covariant single-nucleon current operator [23]. At leading order in this  $Q/m$  expansion (where  $Q$  denotes a generic nucleon momentum), the charge operator, here given in momentum-

† Note that some authors use the convention  $F_\pi/2$  to define the pion decay amplitude.

space, reads

$$\rho_i^{\text{NR}}(\mathbf{k}_i) = e e_{N,i}, \quad (5)$$

where  $\mathbf{k}_i = \mathbf{p}'_i - \mathbf{p}_i$  is momentum transferred to nucleon  $i$  ( $\mathbf{p}_i$  and  $\mathbf{p}'_i$  are the initial and final momenta of nucleon  $i$ ),  $e > 0$  is the electric charge, and  $e_{N,i} = (1 + \tau_{i,z})/2$  is the proton projection operator. To simplify the notation in the equation above and in the following ones we drop terms proportional to the  $\delta$ -function  $\delta(\mathbf{k}_i - \mathbf{q})$ , enforcing momentum conservation. Consequently, the  $\mathbf{k}_i$ -dependence on the left hand side of Eq. (5) becomes equivalent to the  $\mathbf{q}$ -dependence introduced in Eq. (4).

Implicit in the expression above is the assumption that nucleons are point-like objects, an approximation which holds in the (long-wave) limit of  $\mathbf{q} \rightarrow 0$ . However, nucleons' charge and magnetization internal distributions cannot be neglected as the spatial resolution of the probe increases. In order to account for these nucleonic structure effects, form factors that depend on the four-momentum transferred  $Q_\mu^2 = -q^\mu q_\mu = -\omega^2 + q^2$  are folded in the expressions of the e.m. currents for point-like nucleons. In particular, the charge operator of Eq. (5) becomes

$$\rho_i^{\text{NR}}(\mathbf{k}_i) = e e_{N,i}(Q_\mu^2), \quad (6)$$

where now

$$e_{N,i}(Q_\mu^2) = \frac{G_E^S(Q_\mu^2) + G_E^V(Q_\mu^2) \tau_{i,z}}{2}, \quad (7)$$

and  $G_E^{S/V}$  denote the isoscalar/isovector combinations of the proton and neutron electric form factors, normalized as  $G_E^S(0) = G_E^V(0) = 1$  [85].

The non-relativistic one-body e.m. current operator consists of two terms namely the convection current, generated by the motion of charged nucleons, and the spin-magnetization current associated with the nucleonic spins, and in momentum representation it reads

$$\mathbf{j}_i^{\text{NR}}(\mathbf{k}_i, \mathbf{K}_i) = \frac{e}{2m} [2e_{N,i}(Q_\mu^2) \mathbf{K}_i + i\mu_{N,i}(Q_\mu^2) \boldsymbol{\sigma}_i \times \mathbf{q}], \quad (8)$$

where  $\mathbf{K}_i = (\mathbf{p}'_i + \mathbf{p}_i)/2$ , and

$$\mu_{N,i}(Q_\mu^2) = \frac{G_M^S(Q_\mu^2) + G_M^V(Q_\mu^2) \tau_{i,z}}{2}, \quad (9)$$

with the isoscalar/isovector combinations of the proton and neutron magnetic form factors  $G_M^{S/V}$  [85] normalized as  $G_M^S(0) = 0.880 \mu_N$ , and  $G_M^V(0) = 4.706 \mu_N$  in units of the nuclear magneton  $\mu_N$ . Note that by Fourier transforming Eqs. (6) and (8) to obtain a representation in terms of the nucleon coordinates  $\mathbf{r}_i$ , the familiar form of the charge and current operators (as given, *e.g.*, in the Ref. [23]) is restored.

Relativistic effects are accounted for by retaining higher order terms in the  $Q/m$  expansion of the covariant single-nucleon e.m. currents [23]. Inclusion of the first non-vanishing relativistic correction (RC) leads to IA operators which are suppressed by a  $(Q/m)^2$  factor with respect to the corresponding non-relativistic ones, and their formal expressions can be found, *e.g.*, in Ref. [48].

The IA description of nuclei is improved by accounting for the effects of NN and 3N interactions onto the e.m. currents associated with nucleon pairs and triples, respectively. MEC follow naturally once meson-exchange mechanisms are invoked to describe the interactions among nucleons. For example, at large inter-particle distances, where the NN interaction is mediated by the exchange of one pion, two-body e.m. currents of one-pion range emerge. They result from photons hooking up with exchanged pions, as shown by the



seagull and pion-in-flight diagrams illustrated in panels (b) and (c), respectively, of Figure 3 (see next subsection). Direct evaluation of the transition amplitudes associated with these diagrams leads to the OPE current commonly used in the literature (see, *e.g.*, Ref. [86]), which in momentum representation reads

$$\mathbf{j}\pi = -ie \frac{g_A^2}{F_\pi^2} (\boldsymbol{\tau}_i \times \boldsymbol{\tau}_j)_z \left( \boldsymbol{\sigma}_i - \mathbf{k}_i \frac{\boldsymbol{\sigma}_i \cdot \mathbf{k}_i}{\omega_{k_i}^2} \right) \frac{\boldsymbol{\sigma}_j \cdot \mathbf{k}_j}{\omega_{k_j}^2} + i \rightleftharpoons j, \quad (10)$$

where  $\omega_{k_i}^2 = k_i^2 + m_\pi^2$ .

The explicit connection between many-body potentials and many-body current operators is provided by the continuity equation imposed by the gauge invariance of the theory:

$$\mathbf{q} \cdot \mathbf{j} = [H, \rho], \quad (11)$$

where  $H$  is the nuclear Hamiltonian, whose many-body operatorial decomposition is given in Eq. (2), and  $[\dots, \dots]$  denotes a commutator. Neglecting relativistic effects, the equation above can be re-casted in a set of equations of the form

$$\mathbf{q} \cdot \mathbf{j}_i = [t_i, \rho_i^{\text{NR}}] = \left[ \frac{\mathbf{p}_i^2}{2m}, \rho_i^{\text{NR}} \right], \quad (12)$$

$$\mathbf{q} \cdot \mathbf{j}_{ij} = [v_{ij}, \rho_i^{\text{NR}} + \rho_j^{\text{NR}}], \quad (13)$$

where  $\rho_i^{\text{NR}}$  is the non-relativistic IA charge operator defined in Eqs. (5)-(6). Similar equations hold in the presence of 3N forces and beyond. In particular, Eq. (12) is satisfied by the non-relativistic IA current operator  $\mathbf{j}_i^{\text{NR}}$  given in Eq. (8), while the pion-in-flight and seagull e.m. currents of Eq. (10) satisfy Eq. (13) with the OPE potential given in Eq. (3) (see, *e.g.*, Ref. [86]).

The conventional approach exploits the continuity equation and the meson-exchange theoretical insight to consistently construct e.m. two-body currents from the given  $v_{ij}$  potential utilized in the *ab-initio* calculations (see Refs. [21–23] and references therein). These currents are, in the literature, referred to as “model independent” in that they are completely constrained by the NN interaction via gauge invariance. The dominant terms are isovector in character, and they satisfy, by construction, the continuity equation with the static part of the NN potential. The latter is assumed to be due to the exchange of ‘effective’ pseudoscalar (PS or “ $\pi$ -like”) and vector (V or “ $\rho$ -like”) mesons. MEC currents are then due to the exchange of these ‘effective’ PS- and V-mesons, and are constructed utilizing PS- and V-meson propagators projected out of the static part of  $v_{ij}$ . This ensures that the short- and intermediate-range behavior of the MEC is consistent with that of the NN potential. Additional “model independent” currents of short-range follow by minimal substitution in the momentum-dependent part of the potential [21]. They have both isoscalar and isovector terms, and lead to contributions which are typically much smaller (in magnitude) than those generated by the PS and V currents. At large inter-nucleon separations, where the NN potential is driven by the OPE mechanism, the “model independent” current coincides with the standard seagull and pion-in-flight OPE currents given in Eq. (10) and diagrammatically illustrated in panels (b) and (c), respectively, of Figure 3 (appearing in the next subsection). Inclusion of two-body terms in the e.m. current operator, particularly the  $\pi$ -like exchange contribution, is crucial to improve the agreement with the experimental data.

Models of 3N currents that satisfy the continuity equation with conventional 3N potentials have been most recently developed in Ref. [21]. In general, 3N MEC currents, are found to provide small corrections to photo- and electronuclear process [21, 87–90].

The continuity equation does not constrain components of the e.m. currents which are orthogonal to the momentum  $\mathbf{q}$  carried by the photon field. Currents of this nature,

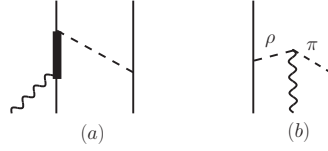


**Figure 1.** Diagrams illustrating conventional “model dependent” two-body currents. See text for explanation. Nucleons,  $\Delta$ 's, mesons, and photons are denoted by solid, thick, dashed, and wavy lines, respectively.

that are purely transverse currents, are, in the literature, referred to as “model dependent” to distinguish them from the “model independent” ones which are completely determined by the nuclear potentials. Possible photon interactions with nucleon pairs involve, for example, its coupling to mesons being exchanged among the nucleons, or virtual nucleon excitations, *e.g.*,  $\Delta$  resonances. The dominant two-body “model dependent” term is found to be associated with excitations of intermediate  $\Delta$  isobars [22, 23, 91, 92]. A contribution belonging to this class is schematically represented by the diagram shown in panel (a) of Figure 1. Additional (and numerically small) “model dependent” currents arise from the isoscalar  $\rho\pi\gamma$ —schematically illustrated in panel (b) of Figure 1—and isovector  $\omega\pi\gamma$  transition mechanisms [22, 23]. Conventional e.m. currents do not involve free-parameters in the sense that they are determined by the many-body potentials entering the nuclear Hamiltonian. However, they are not uniquely determined because the continuity equation does not constrain their transverse component. Their range of applicability extends, in some cases, beyond the pion-production threshold, where isobar currents become more important [23, 93].

Conventional two-body e.m. charge operators are entirely “model dependent” in that they cannot be derived from the NN interaction [23]. Two-body contributions commonly utilized in *ab-initio* studies include  $\pi$ -,  $\omega$ -,  $\rho$ -meson exchange charge operators, as well as  $\rho\pi\gamma$  and  $\omega\pi\gamma$  transition charge operators [23]. In order to reduce the model dependence due to a poor knowledge of meson-NN coupling constants, the  $\pi$ - and  $\rho$ -meson propagators entering the associated meson-exchange amplitudes can be replaced by the ‘effective’ PS- and V-meson propagators projected out of the static NN potential, much in the same fashion implemented to construct the “model dependent” two-body current operators. The dominant contribution to the two-body charge operator is provided by the pion-exchange operator, which is seen to be one order of magnitude larger than that of the remaining two-body contributions [23]. Studies on charge form factors of light nuclei [23] show that two-body effects in the charge operators become important above values of the momentum transfer  $q \simeq 3 \text{ fm}^{-1}$ , while below those the IA picture is sufficient to reach agreement with the experimental data.

## 2.2. The chiral effective field theory approach

We now turn our attention to the  $\chi$ EFT formulation of nuclear forces and e.m. currents. Chiral Lagrangians are arranged in classes characterized by the power  $\nu$  of a small parameter  $Q$  associated with the pion momentum, and so are the nuclear operators obtained from them. The scheme by which nuclear operators are organized according to their scaling in  $Q$  is called power counting. Here, we present the hierarchic arrangement of nuclear many-body operators emerging from the application of the counting scheme introduced by Weinberg in Refs. [25–27].

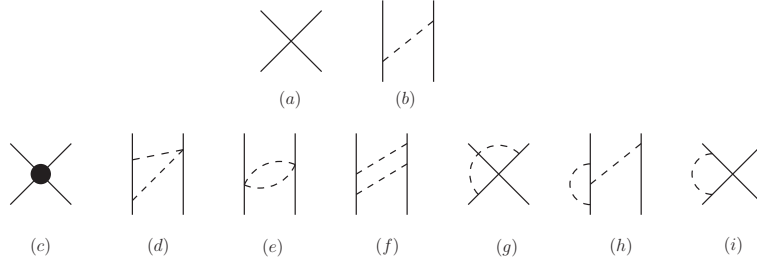


**Figure 2.** Diagrams illustrating contributions to the chiral NN potential entering at LO ( $\nu = 0$ ), panels (a) and (b), and NLO ( $\nu = 2$ ), panels (c)-(i). The solid circle in panel (c) indicate contact interactions of order  $Q^2$  that involve two nucleons' momenta (see text for explanation). Notation is as in Figure 1, but for dashed lines that here represent pions.

*Chiral many-body potentials*

Nuclear  $\chi$ EFT potentials are expressed in terms of multiple-pion exchange contributions, which describe the long- and intermediate-range components of the interaction, along with many-nucleons contact terms (CT) that encode short-range dynamics [31–33]. The chiral nuclear force involves a number of unknown LECs which need to be determined. LECs entering the NN chiral potential are fitted to the available NN scattering data, as it is done for conventional potentials. The chiral NN potential at LO ( $Q^{\nu=0}$ ) consists of the static OPE potential given in Eq. (3) plus two four-nucleon contact interaction terms involving two unknown LECs,  $C_S$  and  $C_T$ . The contact contribution of order  $\nu = 0$  is represented by the diagram illustrated in panel (a) of Figure 2, and the complete chiral potential at LO ( $\nu = 0$ ) reads

$$v^{\nu=0} = v_\pi + v_{CT} = -\frac{g_A^2}{F_\pi^2} \tau_i \cdot \tau_j \frac{\sigma_i \cdot \mathbf{k} \sigma_j \cdot \mathbf{k}}{\omega_k^2} + C_S + C_T \sigma_i \cdot \sigma_j. \quad (14)$$

The NLO<sup>†</sup> contribution scales as  $Q^{\nu=2}$  (there are no  $\nu = 1$  contributions to the NN interaction) and, referring to Figure 2, it includes the one-loop diagrams illustrated in panels (d)–(i), plus seven additional contact terms, illustrated in panel (c). The latter involve two nucleon momenta and are written in terms of seven unknown LECs. At this order, there are also 3N contributions of one-pion range which, however, are seen to vanish (see, *e.g.*, Ref. [28]). At NLO ( $\nu = 2$ ), all the spin-isospin operator structures necessary to describe the NN interaction have been generated, however one needs to incorporate higher order contributions in order to accurately fit NN data. The N2LO ( $\nu = 3$ ) nuclear force consists of additional one-loop terms contributing to the NN sector of the interaction, along with the first non-vanishing contribution to the 3N interaction [31–33]. We note that the leading 3N forces ( $\nu = 3$ ) are suppressed by two orders with respect to the leading NN potential ( $\nu = 0$ ). Currently, phase-shift equivalent chiral NN potentials include up to N3LO ( $\nu = 4$ ) corrections consisting of two-loop contributions and 15 additional contact terms associated with 15 unknown LECs to be fitted to NN scattering data. Chiral NN potentials up to N3LO ( $\nu = 4$ ) have been developed by Epelbaum and collaborators in Refs. [94–96], and by Entem and Machleidt in Refs. [97, 98].

So far, we discussed NN potentials that are constructed in the center-of-mass frame of the two nucleons. However, in Ref. [99] it has been shown that, by requiring Poincaré covariance

<sup>†</sup> Note that in Ref. [37] the NN potential of order  $Q^{\nu=2}$  is counted as being an N2LO instead of an NLO correction. To avoid confusion induced by the use of different conventions, we always specify the power  $\nu$  of  $Q$  when we use the ‘N $n$ LO’ notation.

of the theory, one is forced to introduce additional terms with fixed LECs, in order to describe the two-nucleon potential in reference frames other than the center-of-mass frame. These terms depend on the total momentum of a nucleon pair which can be set to be equal to zero in the center-of-mass frame of a two-nucleon system, but it is in general different from zero in systems with mass number  $A > 2$ , and the effects of these corrections have not yet been quantitatively studied within  $\chi$ EFT formulations [99].

The 3N forces [31–33] enter at N2LO ( $\nu = 3$ ) and involve two unknown LECs. Strong observables that can be used to pin them down are, for example, the binding energies of  $A = 3$  and 4 nuclei. An alternative strategy, implemented by Gazit and collaborators in Ref. [100], is based on the observation that one of the strong LECs enters also the chiral contact two-nucleon weak current at N2LO ( $\nu = 2$ ) [44]. Therefore, experimental data of electroweak processes induced by this weak operator can also be used to fix the LEC. In Ref. [100], the 3N force at N2LO ( $\nu = 3$ ) is constrained so as to reproduce the binding energies of the  $A = 3$  nuclei and the empirical value of the Gamow-Teller matrix element in triton  $\beta$ -decay. Of course, the values of the LECs entering the 3N potential are obtained in combination with the chiral NN interaction utilized in the calculations. 3N forces at N3LO ( $\nu = 4$ ) are presently being investigated by the theoretical community [101]. Chiral 3N forces, if included, are taken at N2LO in the results presented in this review.

Once the chiral potentials are constructed, standard *ab-initio* techniques may be used to solve the many-body Schrödinger equation. Calculations of the energy spectrum of light nuclei that use NN interactions at N3LO and 3N forces at N2LO compare very well with the experimental data (see, *e.g.*, Refs. [70, 102]). More recently, computational techniques developed in the field of lattice QCD have been implemented to solve the many-body problem of nuclear physics in combination with chiral potentials. The method is known as lattice EFT and currently it has been applied to structure studies of nuclei with mass number up to  $A = 28$  [103–105], while selected e.m. transitions have been investigated in  $^{12}\text{C}$  [106] and  $^{16}\text{O}$  [107].

Few comments are now in order. Nuclear potentials and current operators present ultraviolet divergences which need to be removed by a proper regularization procedure. There are two kinds of regularizations which are implemented. The first one concerns the regularization of the loop integrals entering loop contributions (for example, those illustrated in diagrams (d)–(i) of Figure 2). This is accomplished via one of the usual schemes commonly adopted in quantum field theory, *e.g.*, dimensional regularization, and it is followed by a renormalization procedure in which divergences, isolated by the regularization scheme, are reabsorbed by the LECs of the theory. The second kind of regularization follows from the fact that nuclear operators, obtained by evaluating transition amplitudes, are then used in the Schrödinger equation to construct nuclear wave functions and to evaluate matrix elements. Chiral operators have a power law behavior at large momenta that needs to be cut off to avoid infinities. This is accomplished by multiplying nuclear operators with a short-range momentum cutoff. The latter is usually taken to be of the form  $\exp[-(Q/\Lambda)^{2n}]$ , where the choice of  $n$  is contingent to the accuracy one aims to reach. That is, for small values of  $Q$ , where the cutoff behaves as  $\sim 1 - (Q/\Lambda)^{2n} + \dots$ , spurious contributions  $\propto (Q/\Lambda)^{2n}$  generated by the insertion of the cutoff need to be much smaller than the order at which the calculation is performed. In a theory that explicitly includes up to three-pion-exchange contributions, as it is done in the case of the chiral NN potential at N3LO ( $\nu = 4$ ), it is reasonable to set  $\Lambda \sim 500 \text{ MeV} \sim 3m_\pi$ . This way, the cutoff eliminates short-range contributions of four-pion range and beyond, that are not explicitly included in the theory, but are rather subsumed in the LECs. We remark that the discussion on what is the proper renormalization scheme (and power counting) to be adopted is still open [31–33, 108–112]. We will not address this

issue further, and simply keep in mind that calculations with chiral operators depend on an additional parameter, *i.e.*, the momentum cutoff  $\Lambda$  defined above. For comprehensive reviews on  $\chi$ EFT nuclear forces we refer to the review articles by Epelbaum *et al.* and by Machleidt and Entem given in Refs. [31, 32], and Ref. [33], respectively.

### Chiral many-body electromagnetic current operator

One of the great advantages of the  $\chi$ EFT formulation is that e.m. currents are naturally constructed with nuclear forces in a consistent way. Gauge invariance is one among the fundamental symmetries the theory is required to satisfy. Hence, e.m. fields are coupled to nuclear currents which satisfy the continuity equation, order by order, with chiral potentials. Chiral two-body currents  $\mathbf{j}$  were first investigated within  $\chi$ EFT by Park, Min, and Rho in Ref. [45] and constructed up to include one-loop corrections by using covariant perturbation theory. In recent years, the two-body operators for both  $\rho$  and  $\mathbf{j}$  have been derived within two different implementation of time-ordered perturbation theory up to include TPE corrections. The JLab-Pisa group [37, 46–48] used standard time-ordered perturbation theory, while the Bochum-Bonn group [49, 50] used the method of the unitary transformation, which was also utilized to construct the N3LO ( $\nu = 4$ ) two-body potential developed in Refs. [94–96]. Differences between these e.m. operators have been discussed at length in Refs. [37, 46–48, 50]. Here, we will qualitatively describe the hierarchy of the e.m. currents and charge operators that emerges from the chiral expansion, and refer to the aforementioned references for details and formal expressions of the operators. We point out that a proper renormalization of the e.m. OPE operators has been carried out only within the unitary transformation formalism (see Ref. [50]).

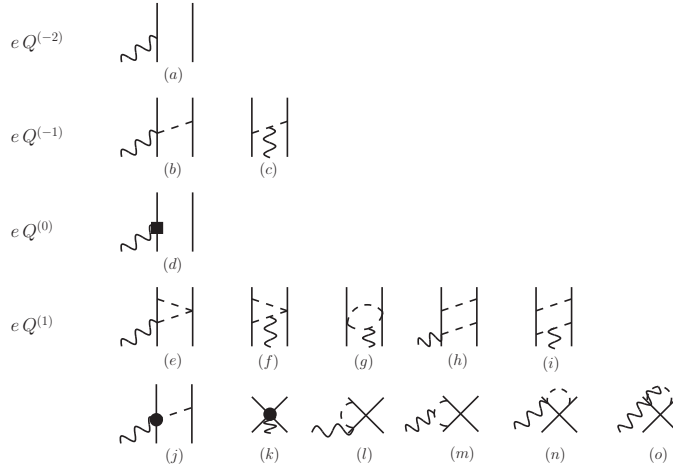


**Figure 3.** Diagrams illustrating one- and two-body chiral e.m. current operators entering at LO ( $\nu = -2$ ) [panel (a)], NLO ( $\nu = -1$ ) [panels (b) and (c)], N2LO ( $\nu = 0$ ) [panel (d)], and N3LO ( $\nu = 1$ ) [panels (e)–(o)]. The LO operator corresponds to the non-relativistic IA operator of Eq. (8). The NLO seagull and pion-in-flight contributions lead to the current operator of Eq. (10). The square in panel (d) represents the  $(Q/m_N)^2$ , or  $(v/c)^2$ , relativistic correction to the LO one-body current operator [or IA(RC)], whereas the solid circle in the tree-level diagram illustrated in panel (j) is associated with a  $\gamma\pi N$  coupling of order  $eQ^2$  (see text for explanation). The solid circle in panel (k) represent a vertex of order  $eQ$ . Notation is as in Figure 2.

We start off with the e.m. current operator  $\mathbf{j}$ , whose contributions are diagrammatically

listed in Figure 3. In Table 1, we also report the scaling in  $eQ^{\nu}$  (where  $e$  is the electric charge brought in by the e.m. coupling) and the range of the operators at each order. Note that the LO term here scales as  $eQ^{\nu=-2}$ , which follows from direct application of the power counting [45] to the disconnected diagram illustrated in panel (a) of Figure 3. In particular, the  $\gamma$ NN vertex scales as the single nucleon e.m. current given in Eq. (8), that is  $eQ$ . In addition, disconnected contributions, such as those illustrated in panels (a) and (d) of this figure, involve an extra  $\delta$ -function in the initial and final momenta of the spectator nucleon—that is  $\delta(\mathbf{p}'_j - \mathbf{p}_j)$ , and they are thus enhanced by a factor  $Q^{-3}$  with respect to connected diagrams. Then, the power counting of diagram (a) is  $eQ \times Q^{-3} = eQ^{-2}$ . Other conventions for the LO's scaling have also been utilized in the literature. Ultimately, what matters is the suppression factor of a given operator  $\propto eQ^{\nu}$  with respect to the LO term  $\propto eQ^{\nu_{\text{LO}}}$ , that is  $eQ^{(\nu-\nu_{\text{LO}})}$ , which is independent of the choice made for the LO term scaling. Translation from one notation to the other is easily achieved keeping that in mind<sup>†</sup>.

Referring to Figure 3, the LO ( $\nu = -2$ ) operator is represented by the diagram illustrated in panel (a) and corresponds to the standard non-relativistic IA current given in Eq. (8). A strict chiral expansion of the nuclear current operators does not guarantee the convergence of the calculated observables to the experimental data. One has to account for nucleonic structure effects via suited form factors. The latter can also be derived within  $\chi$ EFT, however, as it has been observed in Refs. [113–115] in the case of the deuteron charge form factor, the description of nuclear observables is limited by the difficulty of  $\chi$ EFT in describing nucleonic form factors for values of momentum transfer larger than  $q \sim 1.5 \text{ fm}^{-1}$ . Therefore, it is customary also within  $\chi$ EFT formulations to account for nucleonic structure effects via form factors taken from fits to elastic electron scattering data on deuteron and proton. As discussed above, relativistic corrections to the LO one-body current generate a one-body operator which is suppressed by a  $(Q/m)^2$  factor with respect to the LO one. This single-nucleon term, also denoted with IA(RC), is represented by the disconnected diagram illustrated in panel (d) and scales as  $eQ^{\nu=0}$  (N2LO). Nuclear two-body effects appear at NLO ( $\nu = -1$ ) with the OPE currents represented by the diagrams illustrated in panels (b) and (c). These are the well known seagull and pion-in-flight currents of Eq. (10). At N3LO ( $\nu = 1$ ), there are currents of one- and two-pion range as well as contact currents. In particular, pure TPE one-loop contributions are illustrated in panels (e)–(i), while one-loop short-range currents are represented in panels (l)–(o). One-loop corrections at N3LO ( $\nu = 1$ )—that is those illustrated in panels (e)–(i) and (l)–(o)—and OPE currents at NLO ( $\nu = -1$ ) lead to purely isovector operators.

We note that, so far, the e.m. operators involve known LECs, namely the axial coupling constant  $g_A$  and the pion decay amplitude  $F_{\pi}$ . Unknown LECs enter the N3LO ( $\nu = 1$ ) tree-level and contact currents illustrated in panels (j) and (k), respectively. We distinguish between ‘minimal’ and ‘non-minimal’ contact currents. The former are linked to the contact potential at NLO ( $\nu = 2$ )—schematically illustrated in panel (c) of Figure 2—via the continuity equation. That is, the diagram of panel (j) in Figure 3 is determined from the nucleon vertex in panel (c) of Figure 2 via minimal substitution in the nucleon momentum,  $\mathbf{p} \rightarrow \mathbf{p} - ie\mathbf{A}$ , where  $\mathbf{A}$  is the vector photon field. Therefore ‘minimal’ currents involve the same LECs that enter the contact NN potential at NLO ( $\nu = 2$ ), and these can be constrained by fitting  $np$  and  $pp$  elastic scattering data and the deuteron binding energy. Additional contact currents at N3LO ( $\nu = 1$ ) are of ‘non-minimal’ nature and follow from the coupling of

<sup>†</sup> We point out that there are also slightly different power counting schemes adopted in the literature. These differences will be highlighted where needed.

Operator	LO	NLO	N2LO	N3LO	N4LO
$\mathbf{j}$	$\nu = -2$ IA(NR)	$\nu = -1$ OPE	$\nu = 0$ IA(RC)	$\nu = 1$ OPE(LECs) TPE CT(LECs)	
$\rho$	$\nu = -3$ IA(NR)	$\nu = -2$ —	$\nu = -1$ IA(RC)	$\nu = 0$ OPE	$\nu = 1$ TPE

**Table 1.** Scaling in  $eQ^\nu$  up to  $\nu = 1$  and ranges of the chiral e.m. current and charge operators. The  $\mathbf{j}$  operator at N4LO ( $\nu = 2$ ) are have not been derived yet. The acronyms stand for OPE = one-pion-exchange, TPE = two-pion-exchange, CT = contact term, IA = impulse approximation, NR = non-relativistic, and RC = relativistic correction.

the e.m. field tensor  $F_{\mu\nu} = (\partial_\mu A_\nu - \partial_\nu A_\mu)$ . In particular, there are two ‘non-minimal’ contact currents, one is isoscalar and the other one isovector. These contact currents involve unknown LECs, which need to be fixed so as to reproduce e.m. observables.

The tree-level current at N3LO ( $\nu = 1$ ), represented by the diagram illustrated in panel (*j*), results from a  $\gamma\pi N$  coupling of order  $eQ^2$  (indicated by a solid circle) and involves three unknown LECs. Two of them multiply isovector operators and the remaining one multiplies an isoscalar operator. In the present  $\chi$ EFT formulation, with pions and nucleons as relevant degrees of freedom, LECs subsume interactions involving heavy-mesons or nucleon resonances integrated out from the theory. In fact, the isovector part of the tree-level current at N3LO ( $\nu = 1$ ) has the same structure as the current involving the  $N\Delta$ -excitation that is illustrated in panel (*a*) of Figure 1. The latter is known to provide the major contribution to the ‘model dependent’ conventional currents [23]. Similarly, the isoscalar component of the tree-level current at N3LO ( $\nu = 1$ ) simulates the  $\rho\pi\gamma$  transition current [23], illustrated in panel (*b*) of Figure 1. A strategy often implemented to reduce the number of unknown LECs is to ‘saturate’ them with the couplings entering the  $\Delta$ -resonance and/or the  $\rho\pi\gamma$  transition currents illustrated in panels (*a*) and (*b*) of Figure 1, respectively (see Ref. [45]). Once the five LECs listed so far, two associated with contact currents and three belonging to the tree-level current at N3LO ( $\nu = 1$ ), are determined (via saturation and/or via fits to e.m. observables) the current operator can then be used predictively.

As an example, we briefly discuss calculations [48] of the  $n + p \rightarrow d + \gamma$  cross section at thermal neutron energy  $\sigma_{np}^\gamma$  (left panel of Figure 4) and the isovector combination of the  $A = 3$  nuclei’s magnetic moments  $\mu^V(^3\text{H}/^3\text{He})$  (right panel of Figure 4). These observables are induced by the magnetic dipole operator associated with the e.m. nuclear currents. In these calculations, ‘minimal’ LECs associated with the contact currents at N3LO—see panel (*k*) of Figure 3—have been fixed to NN scattering data [33, 98]. The saturation of the  $\Delta$ -resonance has been exploited to fix the two LECs entering the isovector component of the tree-level current at N3LO ( $\nu = 1$ )—see panel (*j*) of Figure 3, while the two isoscalar LECs, entering the tree-level and contact currents at N3LO ( $\nu = 1$ )—see panels (*j*) and (*k*) of Figure 3, respectively—are determined so as to reproduce the deuteron as well as the isoscalar combination of the trinucleon magnetic moments. Then, only one unknown isovector LEC is left. For the calculation in the left (right) panel this LEC is obtained by reproducing the experimental value of the isovector combination of the trinucleon magnetic moments ( $n + p \rightarrow d + \gamma$  cross section at thermal neutron energy) for each value of the momentum cutoff  $\Lambda = 500, 600$  MeV. The results are obtained including cumulatively contributions at LO ( $\nu = -2$ ), NLO ( $\nu = -1$ ), N2LO ( $\nu = 0$ ), and at N3LO ( $\nu = 1$ ). The cumulative contribution at N3LO ( $\nu = 1$ ) is separated into the results labeled ‘N3LO(no-LECs)’ and those labeled

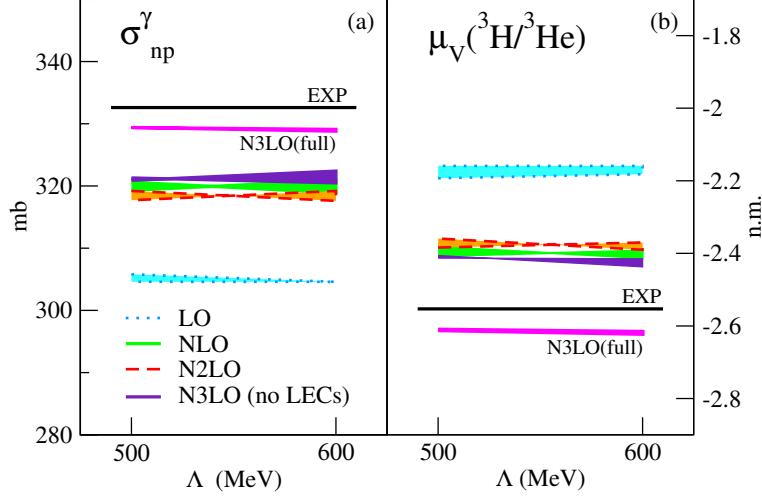


**Figure 4.** (Color online) Cumulative contributions to the  $n + p \rightarrow d + \gamma$  cross section at thermal neutron energies  $\sigma_{np}^\gamma$  (left panel) and trinucleon isovector magnetic  $\mu^V(^3\text{H}/^3\text{He})$  (right panel). The bands represent the sensitivity of the results to the two nuclear Hamiltonians utilized, namely the NN(N3LO)+3N(N2LO) and AV18+UIX. The experimental values for  $\sigma_{np}^\gamma$  and  $\mu^V(^3\text{H}/^3\text{He})$  are  $332.6 \pm 0.7$  and  $2.553 \mu_N$ , respectively. Calculations are from Ref. [48].

‘N3LO(full)’. The former include only contributions of minimal nature. That is the loop-corrections illustrated in panels (e)–(i) and (l)–(o) of Figure 3, and the ‘minimal’ contact currents represented in panel (k) of the same figure. The magenta band labeled ‘N3LO(full)’ is obtained using the full e.m. current operator up to N3LO ( $\nu = 1$ ). The thickness of the bands represents variations due to the use of different nuclear Hamiltonians to generate the nuclear wave functions, namely the AV18+UIX or the NN(N3LO)+3N(N2LO), where the two- and three-body chiral interactions are from Refs. [98] and [100], respectively. The predictions indicated by the magenta bands are within 1% for  $\sigma_{np}^\gamma$  and 3% for  $\mu^V(^3\text{H}/^3\text{He})$  of the experimental values [48], which are represented by the black bands in the figure. We note that the leading two-body correction at NLO ( $\nu = -1$ ) given by the long-ranged OPE seagull and pion-in-flight currents enhances the LO ( $\nu = 0$ ) prediction (or IA prediction) for  $\sigma_{np}^\gamma$  [ $\mu^V(^3\text{H}/^3\text{He})$ ] by  $\sim 4\%$  ( $\sim 9\%$ ). We also note that the N3LO ( $\nu = 1$ ) contributions due to the tree-level and ‘non-minimal’ contact currents are ‘large’ and crucial to bring the theory in agreement with the experimental data. This is an indication that explicit inclusion of the  $\Delta$ -resonance as a fundamental degree of freedom of the theory should improve the convergence of the chiral expansion.

An important check on the chiral e.m. currents is to verify that they satisfy the continuity equation with the chiral potential order by order in the chiral expansion. Of course, up to NLO ( $\nu = -1$ ) the current is conserved since it just involves the non-relativistic IA and OPE seagull and pion-in-flight operators of Eqs. (8) and (10), respectively, which are known to satisfy the continuity equation with kinetic term and OPE potential entering the many-body nuclear Hamiltonian. A simple counting of the powers of momentum entering the l.h.s. and r.h.s. of Eq. (13)<sup>†</sup>, indicates that ‘minimal’ N3LO ( $\nu = 1$ ) e.m. currents, illustrated in Figure 3,

<sup>†</sup> Note that the commutator on the r.h.s. of Eq. (13) brings in an extra factor of  $Q^3$  due to the implicit momentum integrations. Then, for example, for two-body currents at N3LO ( $\nu = 1$ ) the l.h.s. of Eq. (13) scales as  $eQ^2$ . The non-relativist IA charge operator entering the r.h.s. scales as  $eQ^{-3}$ . Therefore, in order to equate the l.h.s. with the r.h.s. the two-body potential  $v_{ij}$  has to scale as  $Q^2$ .



must satisfy the continuity equation with the NN potential of order  $Q^2$ , illustrated in Figure 2. This statement has been explicitly verified in Refs. [37, 49].

A natural question to ask is whether at the order we are considering, that is N3LO ( $\nu = 1$ ), there are three-body currents. Above, we mentioned that 3N forces appear for the first time at NLO ( $\nu = 2$ ), however they are seen to vanish. Therefore, in order to satisfy the continuity equation, three-body currents at N3LO ( $\nu = 1$ ) must either vanish, or be transverse to the photon field. They are, in fact, found to vanish [116], thus the current operator up to N3LO ( $\nu = 1$ ) includes only one- and two-body terms. Leading three-body e.m. currents appear at N4LO ( $\nu = 2$ ) [45], and they have not been derived yet.

### *Chiral many-body electromagnetic charge operator*

The e.m. charge operator has been first investigated from a  $\chi$ EFT perspective by Walzl *et al.* in Ref. [113] and Phillips in Refs. [114, 115]. Phillips derived it up to N3LO (that is, up to  $\nu = 0$  in our counting <sup>†</sup>), while the first derivation of one-loop corrections, entering at N4LO ( $\nu = 1$ ), has been carried out in Ref. [49] by Kölling *et al.* using the unitary transformation method. A time-ordered perturbation theory calculation has subsequently appeared in Ref. [47]. Within this framework, the construction of the charge operator up to one-loop necessarily requires the study of non-static contributions to the chiral OPE and TPE potentials. These corrections that go beyond the static limit are not uniquely determined off-the-energy-shell, therefore the specific form of the N3LO ( $\nu = 0$ ) and N4LO ( $\nu = 1$ ) corrections of one- and two-pion range are found to depend on the off-the-energy-shell prescriptions adopted for non-static terms in the OPE and TPE potentials, respectively [47]. The ambiguity in the non-static potential and charge operators is of no consequence, since different forms are related to each other by a unitary transformation [47], a finding that was first unraveled by Friar [117] for non-static potentials and charge operators of one-pion range.

In what follows, we refer to Figure 5 and list the various contributions to the charge operator up to corrections of order  $eQ^{(\nu=1)}$ . The LO ( $\nu = -3$ ) contribution is represented by the diagram illustrated in panel (a) and corresponds to the non-relativistic IA operator given in Eq. (6). In principle, at NLO ( $\nu = -2$ ) there are contributions of one-pion range which, however, are seen to vanish in the static limit. At N2LO ( $\nu = -1$ ) there is the one-body operator illustrated in panel (b) corresponding to the relativistic correction to the leading IA operator [or IA(RC)]. Two-body contributions appear at N3LO ( $\nu = 0$ ) and are illustrated in panels (c), (d) and (e). In particular, the contribution of panel (c) involves a  $\gamma\pi$ NN vertex—denoted by a solid circle—obtained from a chiral Lagrangian of order  $eQ$  [114, 115], while operators associated with the diagrams of panels (d) and (e) result from accounting for non-static corrections, and are found to be suppressed with respect to the contribution of panel (c) [48]. An operator that has the same structure as the operator resulting from the evaluation of the transition amplitude associated with the diagram of panel (c), has been reported in the late eighties in the review article by Riska [20], however its derivation within a  $\chi$ EFT context has been carried out in recent years by Phillips [114]. Finally, one-loop corrections enter at N4LO ( $\nu = 1$ ) and are represented by the diagrams of panels (f)–(o). Of course, at N3LO ( $\nu = 0$ ) and N4LO ( $\nu = 1$ ) one should also include relativistic corrections to the OPE at NLO ( $\nu = -2$ ) and IA at N2LO ( $\nu = -1$ ), respectively. Note that, due to charge conservation, contributions beyond the IA or LO term vanish at  $|\mathbf{q}| = 0$ .

We emphasize that the structure of the charge operator is quite different from that of the current operator. To begin with, the e.m. current operator at LO ( $\nu = -2$ ) is suppressed by a

<sup>†</sup> Note that in the counting utilized by Phillips the IA charge operator at LO is taken to scale as  $eQ^0$  as opposed to  $eQ^{-3}$  as it is done here, therefore  $\text{N3LO}_{\text{Phillips}} = Q^3$ .

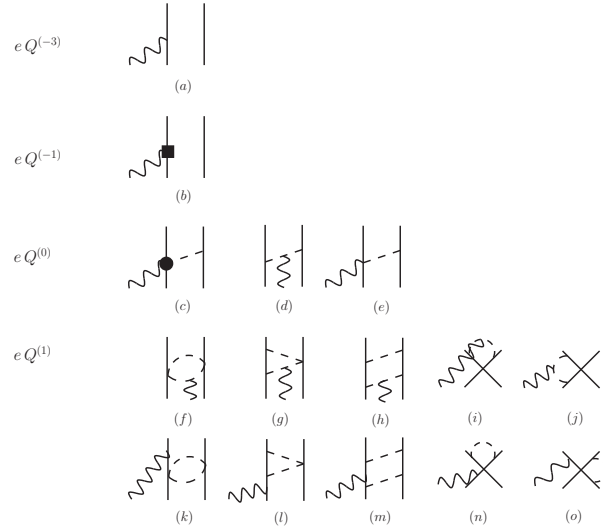


**Figure 5.** Diagrams illustrating one- and two-body charge operators entering at LO ( $eQ^{-3}$ ), panel (a), N2LO ( $eQ^{-1}$ ), panels (b), N3LO ( $eQ^0$ ), panels (c)–(e), and N4LO ( $eQ^1$ ), panels (f)–(o). The square in panel (b) represents the  $(Q/m)^2$ , or  $(v/c)^2$ , relativistic correction to the LO one-body charge operator [or IA(RC)], whereas the solid circle in panel (c) is associated with a  $\gamma\pi N$  charge coupling of order  $eQ$  (see text for explanation). Notation is as in Figure 2.

factor of  $Q$  with respect to the LO ( $\nu = -3$ ) charge operator. Secondly, two-body effects of one-pion range enter the charge operator at N3LO ( $\nu = 0$ ). They instead constitute the NLO ( $\nu = -1$ ) and therefore the major correction to the IA picture in the case of the e.m. current operator. In addition, OPE corrections to the charge operator are  $1/m$  terms that vanish in the static limit of  $m \rightarrow \infty$ . Finally, the charge operator does not involve unknown LECs.

### 2.3. Conventions and notations

Here, we introduce and define some nomenclature. We will use the word ‘conventional’ to describe calculations carried out within the conventional approach described in Sec. 2.1. With ‘ $\chi$ EFT calculations’ we generically denote calculations that use potentials and currents derived within  $\chi$ EFT formulations, briefly outlined in Sec. 2.2. We stress that such  $\chi$ EFT calculations are not always strictly consistent, in that, for example, (i) they may use different regulators for the chiral NN and 3N potentials and currents, (ii) they may use two- and three-body forces which are not evaluated at the same order in the chiral expansion, (iii) they may use chiral e.m. currents which satisfy the continuity equation with only part of the chiral potential. We denote with ‘hybrid calculations’ calculations in which nuclear wave functions are obtained from conventional nuclear Hamiltonians while e.m. current operators are derived from  $\chi$ EFT formulations.

Throughout the course of this review, we try, where possible, to consistently implement the following color scheme: we indicate with black symbols experimental data; cold colors (e.g., cyan, blue) indicate calculations in IA; warm colors (e.g., magenta, red) indicate calculations with two-body currents. The combination (cyan, magenta) is mostly used for  $\chi$ EFT calculations, while the (blue, red) one refers to conventional or hybrid calculations. Similarly, for calculations in which the effect of 3N forces is investigated, warm colors are assigned to final results inclusive of 3N forces’ effects, while cold colors are associated with

results that use only NN potentials.

In the figures, nuclear models are indicated using the convention  $v_{ij} + V_{ijk}$ . For example, calculations that use the conventional AV18 two-nucleon and IL7 three-nucleon interactions are indicated with AV18+IL7. For calculations that use chiral potentials we use the notation NN( $Nn$ LO)+3N( $Nn'$ LO), where  $n$  and  $n'$  specify the chiral orders of the two-nucleon and three-nucleon potentials, respectively. Conventional electromagnetic charge and current operators are denoted using the convention  $\rho^{1\text{-body}+2\text{-body}}$  and  $\mathbf{j}^{1\text{-body}+2\text{-body}}$ . We use ‘IA’ to denote the non-relativistic operators given in Eqs. (5), (6), (8), while relativistic corrections of order  $Q^2/m^2$  to the (non-relativistic) IA operator are denoted with ‘IA(RC)’. Conventional two-body e.m. currents are indicated with ‘MEC’. For example, a calculation that uses conventional one- and two-body vector currents are indicated with  $\mathbf{j}^{\text{IA}+\text{MEC}}$ , or with  $\mathbf{j}^{\text{IA}+\text{IA(RC)}+\text{MEC}}$ , if relativistic correction to the IA operator are included. For chiral e.m. charge (current) operators we use the notation  $\rho^{\text{N}n\text{LO}}$  ( $\mathbf{j}^{\text{N}n\text{LO}}$ ), where  $n$  specifies the cumulative contributions up to  $Nn$ LO corrections included. Of course, chiral e.m. charge and current operators at LO are equivalent to conventional non-relativistic operators in IA, *i.e.*,  $\rho^{\text{LO}} \equiv \rho^{\text{IA}}$  and  $\mathbf{j}^{\text{LO}} \equiv \mathbf{j}^{\text{IA}}$ . When we want to indicate both the current operator and the nuclear potential, we use the following notation: e.m. operator/ $v_{ij} + V_{ijk}$ .

### 3. Electron scattering reactions

In Born approximation, the electron scattering off a nucleus [1–3, 118–121] occurs via the exchange of one virtual photon between the probing electron and the nuclear target, as it is schematically shown in Figure 6. Elastic electron scattering is an ideal probe to study nuclear properties. In fact, due to the weakness of the e.m. interaction with respect to the strong one, responsible of defining the main nuclear structure features, electrons are noninvasive probes, in that they barely perturb the targets. In the light nuclei of interest here, the proton number  $Z$  is small, thus incoming and scattered electrons are accurately described by plane-waves, *i.e.*, they are assumed to be free particles unaffected by the Coulomb field of the nucleus. This approximation is referred to as plane wave Born approximation, and corrections beyond it are accounted for through the evaluation of successive higher-order terms in the  $Z\alpha$  expansion [118].

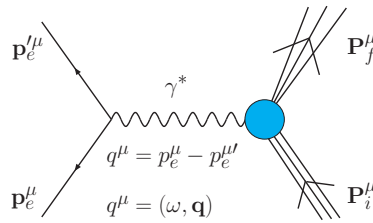


**Figure 6.** (Color online) Diagram illustrating the electron scattering off a nucleus in the one-photon-exchange approximation. A virtual photon  $\gamma^*$  (wavy line) is exchanged between an electron (single solid lines) of initial and final four-momenta  $p_e^\mu$  and  $p_e'^\mu$ , respectively, and a nucleus (triple solid lines) with initial and final momenta  $P_i^\mu$  and  $P_f^\mu$ , respectively.

In Figure 6, an electron with momentum  $p_e^\mu = (\epsilon, \mathbf{p}_e)$  is scattered to a state with momentum  $p_e'^\mu = (\epsilon', \mathbf{p}_e')$ . The virtual photon transfers a momentum  $q^\mu = (\omega, \mathbf{q})$  to the nucleus, which transitions from an initial state  $|\Psi_i\rangle$  with momentum  $P_i^\mu = (E_i, \mathbf{P}_i)$  to a

final state  $|\Psi_f\rangle$  with momentum  $\mathbf{P}_f^\mu = (E_f, \mathbf{P}_f)$ , and momentum conservation implies  $q^\mu = p_e^\mu - p_e'^\mu = \mathbf{P}_f^\mu - \mathbf{P}_i^\mu$ . Furthermore, the interaction proceeds through the exchange of a space-like virtual photon, for which  $q_\mu^2 = \omega^2 - \mathbf{q}^2 < 0^\dagger$ . In electron-induced reactions  $\omega$  and  $\mathbf{q}$  can vary independently (provided that  $|\mathbf{q}| > \omega$ ), as opposed to reactions induced by real photons where  $|\mathbf{q}| = \omega$ . In elastic reactions  $\omega = 0$  (neglecting the recoil of the nucleus), which implies  $|\Psi_i\rangle = |\Psi_f\rangle$ . Reactions in which  $\omega \neq 0$  are instead called inelastic. To different values of  $\omega = E_f - E_i$ , correspond different excitation energies of the nucleus. As  $\omega$  increases to a few MeV, low-lying (discrete) nuclear excited states can be accessed. For energies transferred of the order of  $\sim 10 - 30$  MeV, giant resonance modes in the continuum spectrum of the nucleus are excited, while for values of  $\omega_{q.e.} \sim q^2/(2m)$  quasi-elastic effects dominate, in which the reaction is in first approximation well described as if electrons were scattered off single nucleons. Beyond the quasi-elastic energy region, meson production can be observed. A schematic representation of the double differential cross section for electron scattering at a fixed value of momentum transfer  $q$  is provided in Figure 7.

Because in inelastic electron scattering  $\omega$  and  $\mathbf{q}$  can vary independently, for each value of excitation energy  $\omega$ , one can study the matrix elements' behavior as a function of the momentum transfer. In particular, by varying  $\mathbf{q}$  one changes the spatial resolution of the electron probe, which is  $\propto 1/|\mathbf{q}|$ . At low values of momentum transfer, electron scattering reactions probe long ranged dynamics, while at higher values of momentum transfer shorter distance phenomena are tested, where dynamics from heavier mesons and baryons become relevant.

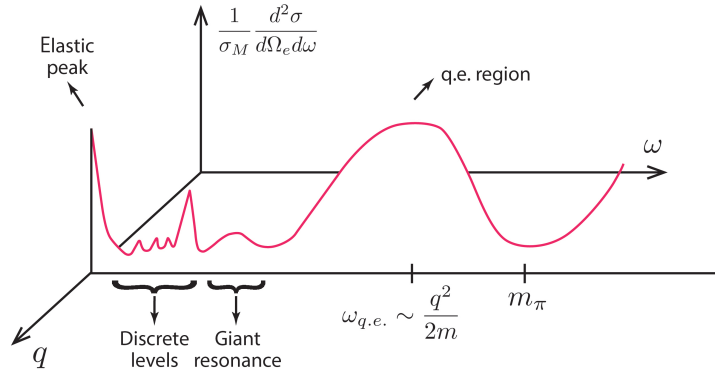


**Figure 7.** (Color online) Schematic representation of the double differential cross section at fixed value of momentum transfer.

Cross sections for elastic scattering and scattering to discrete excited states, for which the transferred energy  $\omega$  is fixed, are expressed in terms of longitudinal (or charge) and transverse (or magnetic) form factors, which are functions of the momentum transferred  $q = |\mathbf{q}|$ , and provide information on the e.m. charge and current spatial distributions inside the nucleus. The double differential cross section for inclusive processes, in which only the scattered electron is detected, is expressed in terms of the longitudinal and transverse

$\dagger$  The four-vector squared  $q_\mu q^\mu$  is here denoted with  $q_\mu^2$ .

response functions. These represent deviations from the Mott cross section,  $\sigma_M$ , associated with electron scattering off point-like nuclei, therefore they contain the nuclear structure information. In particular, longitudinal responses are obtained from a multipole expansion of the nuclear e.m. charge operator  $\rho$ , while the transverse ones are obtained from matrix elements of the nuclear e.m. current operator  $\mathbf{j}$ . Thus, electron scattering processes are particularly suited to test models for both nuclear Hamiltonians, which are used to generate the nuclear wave functions, and e.m. current operators.

In the next subsections we present an overview of recent progress in calculations of electron scattering observables for light nuclei, with emphasis on latest applications of  $\chi$ EFT nuclear and e.m. operators.

### 3.1. Formalism

In plane wave Born approximation, the formal expression of the electron scattering cross section for a process in which a nucleus transitions from an initial state  $|\Psi_i\rangle$  to a final bound state  $|\Psi_f\rangle$  reads [1–3, 23], in the laboratory frame<sup>†</sup>,

$$\frac{d\sigma}{d\Omega_e} = 4\pi\sigma_M f_{rec}^{-1} \left[ \frac{Q_\mu^4}{q^4} F_L^2(q) + \left( \frac{Q_\mu^2}{2q^2} + \tan^2 \frac{\theta_e}{2} \right) F_T^2(q) \right] \quad (15)$$

where  $Q_\mu^2 = -q_\mu^2$  and  $q = |\mathbf{q}|$ . The Mott cross section  $\sigma_M$  is given by

$$\sigma_M = \left\{ \frac{\alpha \cos \theta_e/2}{2\varepsilon \sin^2 \theta_e/2} \right\}^2, \quad (16)$$

and the recoil term is

$$f_{rec}^{-1} = 1 + \frac{2\varepsilon}{M_A} \sin^2(\theta_e/2), \quad (17)$$

where  $M_A$  is the rest mass of the target nucleus with mass number  $A$ ,  $\theta_e$  and  $\varepsilon$  are the electron scattering angle and initial energy.

The experimental longitudinal and transverse form factors for elastic and inelastic transitions,  $F_L(q)$  and  $F_T(q)$ , respectively, are extracted from the measured cross section via Rosenbluth separation, a procedure that allows, by varying  $\theta_e$  at fixed values of  $\omega$  and  $q$ , to separate the longitudinal from the transverse form factor. The multipole expansion of the charge and current operators allows to write form factors in terms of reduced matrix elements of Coulomb ( $T_J^C$ ), magnetic ( $T_J^M$ ), and electric ( $T_J^E$ ) multipole operators [1–3, 23]:

$$F_L^2(q) = \frac{1}{2J_i + 1} \sum_{J=0}^{\infty} |\langle J_f, E_f || T_J^C(q) || J_i, E_i \rangle|^2, \quad (18)$$

$$F_T^2(q) = \frac{1}{2J_i + 1} \sum_{J=0}^{\infty} |\langle J_f, E_f || T_J^M(q) || J_i, E_i \rangle|^2 + |\langle J_f, E_f || T_J^E(q) || J_i, E_i \rangle|^2, \quad (19)$$

where  $J_i$  ( $J_f$ ) is the initial (final) total angular momentum of the nucleus. The Coulomb multipoles ( $CJ$ ) contributing to the longitudinal form factor are obtained from matrix elements of the charge operator  $\rho$ , while the electric ( $EJ$ ) and magnetic ( $MJ$ ) multipoles contributing to the transverse form factor are obtained from matrix elements of the current operator  $\mathbf{j}$  using standard formulae [1–3, 23]. Parity and time-reversal conservation laws impose selection rules. In particular, in elastic scattering (where  $\omega = 0$ , and  $J_i = J_f$ ) only Coulomb multipoles with even  $J$  contribute starting from  $J = 0$ , while electric multipole cannot contribute due to

<sup>†</sup> Note that the convention used for the electric charge is  $\frac{e^2}{4\pi\hbar c}$ .

time-reversal invariance. Thus, only magnetic multipole operators enter the transverse form factor and they carry an odd value of  $J$ , starting from  $J = 1$  since a transverse photon carries unit helicity. In addition, conservation of angular momentum requires that  $J \leq 2J_i$ .

In the limit of  $q \rightarrow 0$ , where the wavelength of the radiation is large compared to the nuclear radius, the elastic Coulomb and magnetic reduced matrix elements are proportional to static charge and magnetic moments [1–3, 23, 119]. In particular, the Coulomb monopole ( $C0$ ) contribution is proportional to the proton number  $Z$ , while for scattering off ground states (thus  $J_i = J_f = J_0$ ), the Coulomb quadrupole ( $C2$ ) and magnetic dipole ( $M1$ ) reduced matrix elements are proportional to the ground-state quadrupole and magnetic dipole moments, respectively. They are obtained from the evaluations of the following ground-state expectation values [1–3, 119]

$$Q = \langle J_0 M_0 = J_0 | \hat{Q} | J_0 M_0 = J_0 \rangle , \quad (20)$$

$$\mu = 2m \langle J_0 M_0 = J_0 | \hat{\mu}_z | J_0 M_0 = J_0 \rangle , \quad (21)$$

where the quadrupole and magnetic dipole operators are defined as

$$\hat{Q} = \int d\mathbf{x} \rho(\mathbf{x})(3z^2 - \mathbf{x}^2) , \quad (22)$$

$$\hat{\mu} = \frac{1}{2} \int d\mathbf{x} [\mathbf{x} \times \mathbf{j}(\mathbf{x})] . \quad (23)$$

and  $\rho(\mathbf{x})$  and  $\mathbf{j}(\mathbf{x})$  are the charge and current density operators [86]. Therefore, probing electrons are sensitive to static e.m. properties of nuclei as  $q \rightarrow 0$ .

In inelastic transitions, all kinds of multiple operators with  $|J_i - J_f| \leq J \leq J_i + J_f$  contribute to the form factors, which are in this case referred to as transition form factors. In addition, parity conservation requires that  $\pi_i \pi_f = (-1)^J$  [ $\pi_i \pi_f = (-1)^{J+1}$ ] for Coulomb and electric (magnetic) transitions, where  $\pi_{i,f}$  are the parities of the initial and final nuclear states. In the long-wave limit, the transverse electric multiple operator  $EJ$  can be written in terms of the Coulomb operator  $CJ$ . In this limit, one replaces the longitudinal current entering the  $EJ$  transition operator with the charge operator  $\rho$  using the continuity equation (this is, in fact, the Siegert theorem [122]). Therefore, in the long-wave limit, the transverse electric multipole operator  $EJ$  is obtained from matrix elements of the charge operator  $\rho$ , *i.e.*, from Coulomb  $CJ$  multipoles. This is a powerful approximation that allows to implicitly include in  $EJ$  multipoles the effect of MEC corrections (of the three-vector e.m. currents) without explicitly including them in the calculations.

Reduced matrix elements entering the form factors for elastic and inelastic scattering to discrete excited nuclear states also enter the transition rate for photo-emission reactions (which will be discussed in Sec. 4.3). Because in this kind of reactions the emitted photon is real, the process is induced by transverse multipoles. For natural parity states, the dominant transverse contributions are the  $M1$  and  $E2$  transitions operators. With the use of standard formulas [119] the reduced transition probabilities  $B(E2)$  and  $B(M1)$  are obtained from them as follows

$$B(E2) = \frac{1}{2J_i + 1} |\langle J_f || \hat{Q} || J_i \rangle|^2 , \quad (24)$$

$$B(M1) = \frac{1}{2J_i + 1} |\langle J_f || \hat{\mu}_z || J_i \rangle|^2 , \quad (25)$$

where  $\hat{Q}$  and  $\hat{\mu}_z$  are the operators defined in Eqs. (22) and (23), respectively<sup>†</sup>.

Below, we focus on ground-state properties which are inferred from elastic electron scattering. In particular, Section 3.2 is devoted to discuss static e.m. nuclear moments,

<sup>†</sup> Note that Eq. (24) is obtained in the long-wave limit with the use of the Siegert theorem.

while in Section 3.3 we present a number of calculations of elastic form factors. Strictly speaking, ground-state static electric and magnetic moments are accessed via many different experimental procedures including, in some cases, elastic electron scattering. Despite the fact that this section is devoted solely to electron scattering processes, we discuss the theoretical calculations of light nuclei e.m. moments here. We find this arrangement to be convenient because the discussion on nuclear static e.m. properties is complementary to the discussion on nuclear elastic form factor that follows. A presentation of the main features of the double differential cross section for inelastic scattering and associated observables is deferred to Section 3.4.

### 3.2. Ground-state properties: electromagnetic moments

Static e.m. properties of light nuclei play an important role in testing the validity of nuclear models. For example, the experimental evidence of a non-zero deuteron quadrupole moment pointed to the necessity of introducing tensor components in the NN interaction. Similarly, static magnetic moments of nuclear ground states have been determinant to establish the role of MEC. Indeed, the seminal studies on MEC effects were focused on evaluating their contributions to nuclear magnetic moments [11, 12]. Since then, modern and highly sophisticated conventional MEC have been successfully utilized in a number of calculations of nuclear e.m. properties [23]. In recent calculations, based on wave functions obtained with the HH method, trinucleon magnetic moments are found to be within less than 1% of the experimental values [90], when the AV18+UIX nuclear Hamiltonian and consistent MEC currents are used. MEC provide a  $\sim 16\%$  correction to the total calculated values [90].

**Table 2.** GFMC results from Ref. [123] for  $A \leq 9$  nuclear states' energies, dipole magnetic [ $\mu$ (IA)] and quadrupole ( $Q$ ) moments, compared to experimental values [124–128]. Numbers in parentheses are statistical errors for the GFMC calculations or experimental errors; errors of less than one in the last decimal place are not shown.

${}^AZ(J^\pi, T)$	$E$ [MeV]		$\mu$ (IA) [n.m.]		$Q$ [ $\text{fm}^2$ ]	
	GFMC	Expt.	GFMC	Expt.	GFMC	Expt.
${}^2\text{H}(1^+, 0)$	-2.225	-2.2246	0.847	0.8574	0.270	0.286
${}^3\text{H}(\frac{1}{2}^+, \frac{1}{2})$	-8.50(1)	-8.482	2.556	2.979		
${}^3\text{He}(\frac{1}{2}^+, \frac{1}{2})$	-7.73(1)	-7.718	-1.743	-2.127		
${}^6\text{Li}(1^+, 0)$	-31.82(3)	-31.99	0.817	0.822	-0.20(6)	-0.082(2)
${}^7\text{Li}(\frac{3}{2}^-, \frac{1}{2})$	-39.0(1)	-39.24	2.87	3.256	-4.0(1)	-4.06(8)
${}^8\text{Li}(2^+, 1)$	-41.5(2)	-41.28	1.16(2)	1.654	3.3(1)	3.14(2)
${}^8\text{B}(2^+, 1)$	-37.5(2)	-37.74	1.45(1)	1.036	5.9(4)	6.83(21)
${}^9\text{Be}(\frac{3}{2}^-, \frac{1}{2})$	-58.1(2)	-58.16	-1.18(1)	-1.178	5.1(1)	5.29(4)
${}^9\text{Li}(\frac{3}{2}^-, \frac{3}{2})$	-45.2(3)	-45.34	2.66(3)	3.439	-2.3(1)	-3.06(2)
${}^9\text{C}(\frac{3}{2}^-, \frac{3}{2})$	-39.7(3)	-39.04	-0.75(3)	-1.391	-4.1(4)	

Hybrid studies on  $M1$  static properties of  $A \leq 3$  nuclei, based on the N3LO ( $\nu = 1$ )  $\chi$ EFT e.m. currents of Ref. [44], have been first carried out by Song and collaborators in Refs. [129, 130]. The model dependence of the hybrid predictions has been studied by utilizing different realistic nuclear Hamiltonians, including Hamiltonians derived within  $\chi$ EFTs. Using resonance saturation arguments [129, 130], the authors have reduced the number of LECs entering the e.m. currents to two. These LECs multiply contact operators at

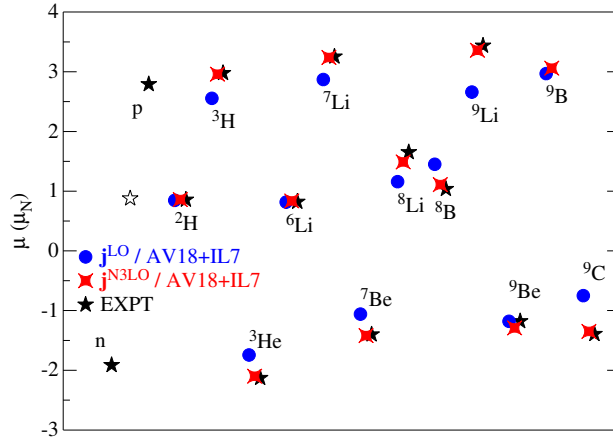


**Figure 8.** (Color online) Magnetic moments in nuclear magnetons for  $A \leq 9$  nuclei from Ref. [123]. Black stars indicate the experimental values from Refs. [125, 126, 132], while blue dots (red diamonds) represent GFMC calculations which include the LO or IA (N3LO) e.m. currents from  $\chi$ EFT. Predictions are for nuclei with  $A > 3$ .

N3LO—see panel (k) of Figure 3—and they have been fixed to the experimental trinucleon magnetic moments ( $np \rightarrow d\gamma$  cross section at thermal neutron energies and the deuteron magnetic moment) when used to predict the  $np \rightarrow d\gamma$  cross section at thermal neutron energies and the deuteron magnetic moment (trinucleon magnetic moments). In Ref. [129], it has been found that the isoscalar and isovector combinations of trinucleon magnetic moments agree with the experimental value at the  $\sim 2 - 3\%$  level (a finding that was confirmed in the studies of Ref. [48] summarized in Figure 4), and it has been conjectured that additional corrections from three-body e.m. currents entering at N4LO, along with the use of improved nuclear wave functions, could reduce the present gap between theoretical and experimental values.

Moving towards larger nuclei, we find a number of *ab-initio* calculations of magnetic moments carried out in IA. A recent summary on the current status for nuclei up to  $A \sim 15$  can be found, *e.g.*, in Ref. [131]. Here, we limit ourselves to report in Table 2 a set of GFMC calculations of energies and static e.m. moments in IA of nuclei with  $A \leq 9$ . In fact, we want to emphasize calculations which account for two-body effects in the e.m. currents, as most recently reported in Ref. [123]. Magnetic moments for  $A \leq 7$  nuclei, comprehensive of two-body corrections, have been first evaluated in Ref. [22] using GFMC computational techniques and conventional MEC operators [21, 22], in combination with the AV18+IL2 nuclear Hamiltonian. In that work, it has been found that MEC corrections increase the  $A = 3, 7$  isovector magnetic moments by up to 16%, bringing them into very good agreement with experimental data. That study has been recently extended in Ref. [123] to include larger nuclei and improved nuclear wave functions obtained from the AV18 and an updated version of the 3N interaction, *i.e.*, the IL7. In addition,  $\chi$ EFT e.m. current operators of Refs. [37, 46, 48] have been tested in hybrid calculations which use the same nuclear wave functions obtained from the AV18+IL7 interaction.

GFMC results for nuclear magnetic moments are summarized in Figure 8, where black stars represent the experimental data [125, 126, 132]—there are no data for the  ${}^9\text{B}$  magnetic moment. For completeness, experimental values for the proton (p) and neutron (n) magnetic moments, as well as their sum (empty star), which corresponds to the magnetic moment of an



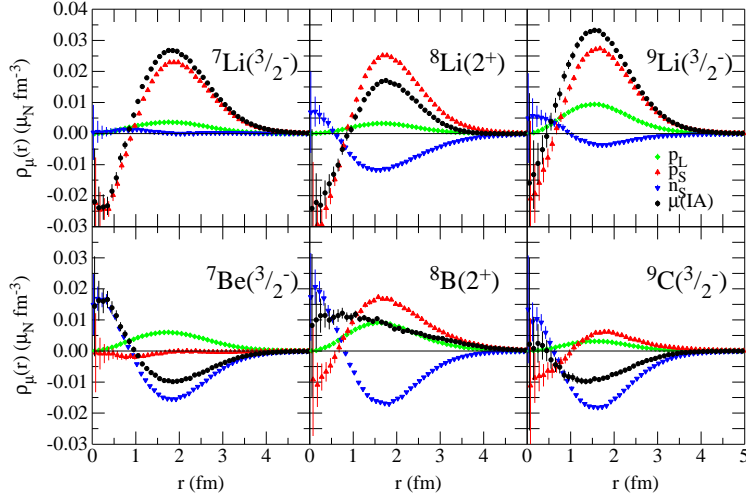


**Figure 9.** (Color online) One-body magnetic density in nuclear magnetons per  $\text{fm}^3$  for selected nuclei (see text for explanation).

S-wave deuteron, are shown. The static nuclear magnetic dipole operator induced by the IA current of Eq. (8) coincides with the LO in  $\chi\text{EFT}$  and reads

$$M1 = \mu(\text{IA}) = \sum_i (e_{N,i} \mathbf{L}_i + \mu_{N,i} \boldsymbol{\sigma}_i) , \quad (26)$$

where  $\mathbf{L}_i$  is the orbital angular momentum of nucleon  $i$  (only protons contribute to the convection e.m. current), and the  $e_{N,i}$  and  $\mu_{N,i}$  expressions are given in Eqs. (7) and (9), respectively, and should be taken in the limit of  $Q_\mu^2 \rightarrow 0$ . Results obtained with the operator given above are represented by blue dots of Figure 8, and they reproduce the bulk properties of the considered nuclear magnetic moments. The magnetic moment associated with the protons' convection current is found to be small if compared with proton and neutron spin magnetization terms [123]. Nuclear magnetic moments in IA are driven by those associated with valence nucleons. In particular, the magnetic moment of an odd-even nucleus is driven by that of the unpaired proton, and lines up in the upper part of Figure 8, similarly, the magnetic moment of an even-odd nucleus is driven by that of the unpaired neutron, and sits in the bottom part of the figure. Magnetic moments for odd-odd nuclei are instead driven either by a proton-neutron or by a triton-neutron ( ${}^3\text{He}$ -proton) cluster.

These general features can be best appreciated by looking at the IA magnetic densities represented in Figure 9. Here, the red upward-pointing triangles are the contribution from the proton magnetic moment weighted by the difference between the spatial distributions for proton with spin up and down,  $\mu_p[\rho_{p\uparrow}(r) - \rho_{p\downarrow}(r)]$ , while the blue downward-pointing triangles are the analogous contribution but from the neutron magnetic moments. The green diamonds are the proton orbital (convection current) contribution, and the black circles are the sum. The integrals of the black curves over  $d^3r$  give the total magnetic moments of the nuclei in IA. For example, for the odd-even  ${}^7\text{Li}$  and  ${}^9\text{Li}$  nuclei, the neutrons are paired up, and give

only a small contribution, so the total IA magnetic moment is close to the sum of the proton spin and orbital parts. However,  ${}^8\text{Li}$  has one unpaired neutron which acts against the proton and significantly reduces the overall IA values. Similar considerations apply to the bottom panels of Figure 9.

GFMC results of nuclear magnetic moments, which account for two-body effects and relativistic corrections in the e.m. current operator, are represented in Figure 8 by red stars. The main features of the  $\chi\text{EFT}$  e.m. currents [37, 46, 48] utilized in the calculations have been discussed in Section 2.2. As mentioned there, LECs of minimal nature, associated with N3LO contact currents of the type illustrated in panel (k) of Figure 3, can be fixed to NN scattering data. In this work, they have been assigned the values obtained from the phase-shifts analysis carried out in Refs. [33, 97, 98]. Instead, referring to Figure 3, LECs entering the N3LO operator illustrated in panel (j) and those of non-minimal nature associated with the contact currents of panel (k), have been determined so as to reproduce the magnetic moments of  $A = 2$  and 3 nuclei [48]. Thus, only the results for  $A > 3$  nuclei with this  $\chi\text{EFT}$  e.m. current are predictions. Referring to Figure 8, corrections beyond the leading IA operator always increase the IA results in the direction of the experimental data, except for  ${}^6\text{Li}$  and  ${}^9\text{Be}$ , where the contributions from two-body e.m. currents, while being small, make the predictions slightly worse. The effect of two-body components in the e.m. current operator is particularly pronounced in the  ${}^9\text{C}$  and  ${}^9\text{Li}$  nuclei, where they provide up to  $\sim 40\%$  and  $\sim 20\%$ , respectively, of the total predicted magnetic moments' values. Two-body effects, while being significant for the  ${}^9\text{C}$  and  ${}^9\text{Li}$  magnetic moments, have been found to be negligible for those of  ${}^9\text{Be}$  and  ${}^9\text{B}$ . This behavior can be explained considering the dominant spatial symmetries of the nuclear wave functions for these  $A = 9$  systems. For example, the dominant spatial symmetry of  ${}^9\text{Be}$  ( ${}^9\text{B}$ ) corresponds to an  $[\alpha, \alpha, n(p)]$  structure [133]. Therefore, the unpaired nucleon outside the  $\alpha$  clusters feels no OPE potential—see panel (a) Figure 2. As a consequence, two-body currents of one-pion range entering at NLO—see panels (b) and (c) of Figure 3—produce a negligible correction. On the other hand, the dominant spatial symmetry of  ${}^9\text{C}$  ( ${}^9\text{Li}$ ) corresponds to an  $[\alpha, {}^3\text{He} ({}^3\text{H}), pp (nn)]$  structure, and NLO OPE e.m. currents contribute in both the trinucleon clusters and in between the trinucleon clusters and the valence  $pp (nn)$  pair.

In Ref. [123], also conventional MEC of Refs. [21, 22] have been used to calculate nuclear magnetic moments. It has been found that GFMC results obtained with  $\chi\text{EFT}$  and conventional currents are qualitatively in agreement, particularly for isovector combinations of magnetic moments. Quantitative differences between the two models have been found to be more pronounced in isoscalar combinations of magnetic moments<sup>†</sup>. In general,  $\chi\text{EFT}$  e.m. currents are found to provide results which are in a better agreement with the experimental data for the considered nuclear magnetic moments.

### 3.3. Ground-state properties: elastic form factors

Elastic form factors of light nuclei are key observables to test nuclear Hamiltonians and current operators. Their longitudinal (L) and transverse (T) components are given in Eqs. (18) and (19), respectively, to be taken with  $J_f = J_i = J_0$ . Elastic longitudinal and transverse form factors reflect the charge and magnetic spatial distributions, respectively. In this section we provide an overview of the present status of elastic form factors in *ab-initio* calculations, with emphasis on studies that include two-body currents and/or 3N forces. We organized the

<sup>†</sup> We note that the isoscalar,  $\mu(\text{IS})$ , and isovector,  $\mu(\text{IV})$ , combinations of nuclear magnetic moments are defined as  $\mu(T, T_z) = \mu(\text{IS}) + \mu(\text{IV})T_z$ , where  $\mu(T, T_z)$  is the magnetic moment of a nucleus with total isospin,  $T$ , and total isospin  $z$ -projection,  $T_z$ .

results in subsections devoted to different nuclei with increasing mass number, ranging from the deuteron to  $^{12}\text{C}$ . When possible, we compare theoretical results obtained by different groups for the same observables and check them against experimental data.

*3.3.1. The deuteron* — Electron-deuteron elastic scattering reactions have been intensively investigated both from an experimental and a theoretical point of view. There exists a vast literature on this topic, for which we refer to the review articles of Refs. [8, 121, 134]. Conventional calculations based on realistic NN interactions and consistent e.m. two-body MEC provide a satisfactory description of the available experimental data [23, 76, 135, 136]. Currently, there are also quite a few calculations of deuteron e.m. properties that are based on  $\chi\text{EFT}$  formulations [48, 113–115, 137–140]. Within the  $\chi\text{EFT}$  framework, a general good agreement between the calculated and experimental deuteron form factors is observed, provided that the e.m. structure of the nucleons is accounted for via suited nucleonic form factors.

Traditionally, the charge and magnetic spatial distributions of the deuteron are studied in terms of the charge ( $G_C$ ), quadrupole ( $G_Q$ ), and magnetic ( $G_M$ ) form factors, and they are related to the Coulomb,  $T_0^C$ , and magnetic transverse,  $T_1^M$ , multipole operators discussed in Sec. 3.1 via [23]

$$\sqrt{\frac{4\pi}{3}}T_0^C(q) = (1 + \eta)G_C(q) , \quad (27)$$

$$\sqrt{\frac{4\pi}{3}}T_2^C(q) = \frac{2\sqrt{2}}{3}\eta(1 + \eta)G_Q(q) , \quad (28)$$

$$-i\sqrt{\frac{4\pi}{3}}T_1^M(Q) = \frac{2}{\sqrt{3}}\sqrt{\eta(1 + \eta)}G_C(q) , \quad (29)$$

where  $\eta = (q/2M_d)^2$  and  $M_d$  is the deuteron mass. These form factors are normalized as

$$G_C(0) = 1 , G_M(0) = (M_d/m_N)\mu_d , G_Q(0) = M_d^2 Q_d , \quad (30)$$

where  $\mu_d$  and  $Q_d$  are the deuteron magnetic moment (in units of  $\mu_N$ ) and quadrupole moment, respectively. The deuteron form factors are extracted from the measured structure functions  $A$  and  $B$ , and tensor polarization  $T_{20}$ . The expressions relating these measured quantities with the form factors can be found in Ref. [23].

In Figure 10, the calculated deuteron charge and quadrupole form factors from Ref. [48] are compared with the experimental data in panels (a) and (b), respectively. In these figures, results from both a  $\chi\text{EFT}$  and a hybrid calculation based on the  $\chi\text{EFT}$  charge operator at LO ( $\nu = -3$ ) and N3LO ( $\nu = 0$ ) are shown. The cyan dotted band (blue dashed line) and magenta hatched (red solid) band are obtained using deuteron wave functions from the N3LO ( $\nu = 4$ ) chiral NN potential by Entem and Machleidt [98] (AV18 potential), in combination with the charge operator at LO ( $\nu = -3$ ) and N3LO ( $\nu = 0$ ), respectively. The thickness of the bands indicates the sensitivity of the results with respect to two values of the regularization cutoff corresponding to  $\Lambda = 500$  and  $600$  MeV (used consistently in the chiral NN potential and e.m. currents, for the  $\chi\text{EFT}$  calculation). The IA and IA(RC) operators at LO and N2LO—see panels (a) and (b) of Figure 5—are cutoff independent, therefore hybrid results at LO are represented by a line, while the thickness of the cyan dotted band associated with the  $\chi\text{EFT}$  results at LO is due to variations in the cutoff utilized to regularize the chiral NN potential.

The charge and quadrupole form factors are determined by the isoscalar component of the charge operator. Therefore, the N4LO ( $\nu = 1$ ) loop-corrections, illustrated in panels (f)–(o) of Figure 5, do not contribute to these observables, as they lead to isovector operator structures.

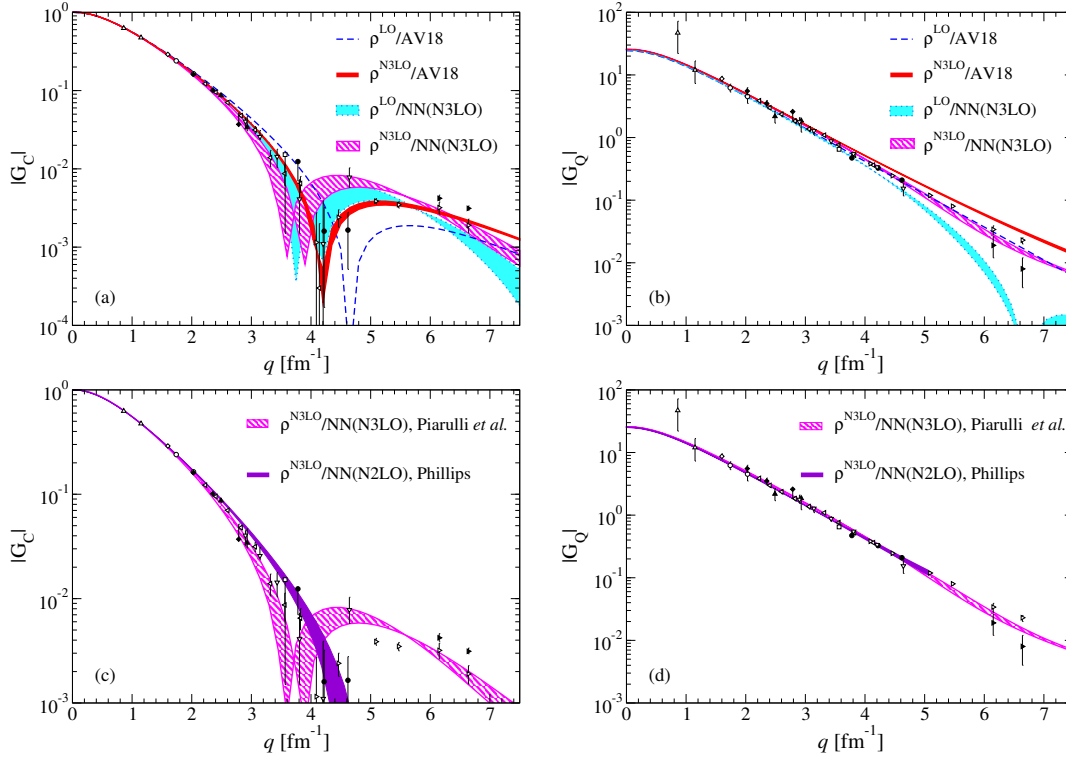


**Figure 10.** (Color online) Deuteron charge, panel (a), and quadrupole, panel (b), form factors from Ref. [48] compared with experimental data from Refs. [141–162]. Cutoffs  $\Lambda$  in the range 500–600 MeV are displayed by the bands. In panels (c) and (d), results from Ref. [48] (magenta hatched bands) are compared with those obtained in Ref. [115] (purple solid bands). See text for more details.

We emphasize that the results discussed here include e.m. nucleonic form factors—that is the  $G_{E/M}^{S/V}$  introduced in Eqs. (7) and (9). As noted in Ref. [113], a simple chiral expansion of the charge operator provides poor agreement with the experimental data for  $q \gtrsim 1.5 \text{ fm}^{-1}$ . The inclusion of e.m. nucleonic form factors taken from experimental data ensures a reasonable fall-off of the calculated deuteron form factors at increasing values of  $q$ . In doing so, a very good agreement between the full theory and experiment is observed up to values of  $q \sim 3 \text{ fm}^{-1}$  in the case of the charge form factor, and of  $q \sim 6 \text{ fm}^{-1}$  in the case of the quadrupole form factor. Hybrid and  $\chi$ EFT results are in very good agreement for low values of momentum transfered ( $q \lesssim 3 \text{ fm}^{-1}$ ), however, as  $q$  increases these observables become sensitive to the wave functions utilized in the computations, which display some differences (see, *e.g.*, Figure 16 of Ref. [33]). This can be appreciated by comparing the calculations based on the N3LO ( $\nu = 0$ ) e.m. charge operators, with the chiral N3LO ( $\nu = 4$ ) [98] (magenta hatched band) and the AV18 [76] (solid red band) NN potentials. The diffraction region of  $G_C$  is better reproduced by the AV18 calculation, while the  $\chi$ EFT results for  $G_Q$  are in better agreement with the experimental data for  $q \gtrsim 3 \text{ fm}^{-1}$ .

In the bottom panels of Figure 10, we compare the full  $\chi$ EFT results by Piarulli *et al.* [48] (magenta hatched band) with those obtained by Phillips in Refs. [114, 115] (purple solid band). The latter employ the chiral N2LO ( $\nu = 3$ ) NN interaction from Ref. [96] and the

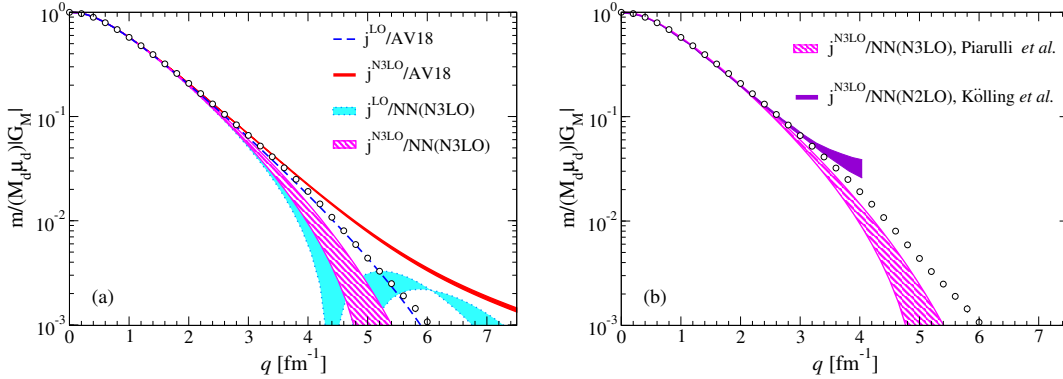


**Figure 11.** (Color online) Panel (a): The deuteron magnetic form factor  $G_M(q)$  from Ref. [48] compared with the experimental data from Refs. [121, 141, 147, 148, 163, 164]. Color code as in Figure. 10. Panel (b): Calculated deuteron magnetic form factor from Ref. [48] (magenta hatched band) compared with that obtained in Ref. [140] (purple solid band), based on the N2LO NN interaction from Ref. [96] and current operators at N3LO.

charge operator at N3LO ( $\nu = 0$ )<sup>†</sup>. These calculations are in good agreement at low values of momentum transfer and exhibit a similar cutoff dependence. However, as  $q$  increases the predicted form factors exhibit a more noticeable sensitivity to the particular NN potential utilized to solve the Schrödinger equation (a finding that confirms the conclusions of previous studies by Phillips [114, 115]).

We also report that the  $\chi$ EFT (AV18) calculated deuteron quadrupole moment,  $Q_d$ , inclusive of MEC, is found to be within 1% (2%) of the experimental value, and to show a  $\sim 1\%$  (negligible) variation in going from  $\Lambda = 500$  to 600 MeV [48].

We now turn our attention to the deuteron magnetic form factor. Because the deuteron is isoscalar, only isoscalar components in the chiral e.m. current contribute to its magnetic form factor. Therefore, OPE and TPE currents at NLO ( $\nu = -1$ )—see panels (b) and (c) of Figure 3—and N3LO ( $\nu = 1$ )—see panels (e)–(i) and (l)–(o) of the same figure—do not contribute to this observable. The isoscalar e.m. current operator involves only two e.m. LECs both entering at N3LO ( $\nu = 1$ ); one accompanies a short-ranged contact interaction—see panel (k) of Figure 3—and the other one multiplies the isoscalar part of the tree-level current illustrated in panel (j) of Figure 3. We note that isoscalar contributions of one-pion range are suppressed by three powers of  $Q$  with respect to the LO ( $\nu = -2$ ) or IA term.

In panel (a) of Figure 11, we show the calculated deuteron magnetic form factor from Ref. [48], with the same color code as in Figure 10. Here, the e.m. LECs entering the isoscalar current at N3LO ( $\nu = 1$ ) have been constrained so as to reproduce the deuteron magnetic moment,  $\mu_d$ , as well as the isoscalar combination of the trinucleon magnetic moments,  $\mu^S$ , defined in Eq. (31). Therefore, there is no prediction for the deuteron static magnetic moment with this chiral e.m. current. LECs of minimal nature that multiply contact operators at N3LO ( $\nu = 1$ ) have been taken from the phase-shift analysis carried out in Refs. [33, 98]. We observe a rather good agreement with the experimental data for values of  $q \simeq 2 \text{ fm}^{-1}$ . However, at larger values of momentum transferred the hybrid and  $\chi$ EFT results are quite different. In particular, calculations based on the AV18 interaction and e.m. operators at LO ( $\nu = -2$ ) do

<sup>†</sup> Note that the power counting used in Ref. [115] is slightly different from the one we use. In particular, in the counting of Ref. [115], relativistic corrections to the LO charge operator lead to a one-body operator that is of order N4LO, which is, therefore, neglected.

not show the diffraction pattern observed in the  $\chi$ EFT results at LO ( $\nu = -2$ ). This is due to the different deuteron wave functions generated by the two corresponding NN potentials. We remark that the N3LO ( $\nu = 1$ ) e.m. current is conserved with the NN potential at NLO ( $\nu = 2$ ), therefore, the  $\chi$ EFT calculation based on the NN potential at N3LO ( $\nu = 4$ ) would require an e.m. current of order  $\nu = 3$  in order to strictly fulfill the continuity equation.

In panel (b) of Figure 11, we compare the results by Piarulli *et al.* [48] (hatched magenta band) with the fully consistent  $\chi$ EFT calculations by Kölling *et al.* [140] (solid purple band) based on the chiral NN potential at N2LO ( $\nu = 3$ ) [96] and chiral e.m. currents at N3LO ( $\nu = 1$ ) [49, 50], both derived within the unitary transformation method. In that work, the short-ranged e.m. LEC—see panel (k) of Figure 3—is fixed to the deuteron magnetic moment, while the isoscalar OPE e.m. LEC—see panel (j) of Figure 3—is fitted to the measured B structure function [140]. The theoretical results for the deuteron magnetic form factor are in very good agreement with each other and with the experimental data for values of momentum transferred  $q \simeq 3 \text{ fm}^{-1}$ , and present a comparable cutoff dependence.

Finally, we report on a very recent evaluation of deuteron  $G_C$ ,  $G_Q$ , and  $G_M$  form factors carried out in a fully consistent and cutoff independent  $\chi$ EFT formulation [165]. The calculation, based on the renormalizable approach of Ref. [166], uses e.m. charge, e.m. currents, and NN operators at LO, and predicts deuteron form factors which are in good agreement with the experimental data, provided that the nucleonic e.m. structure is folded in the evaluation via appropriate nucleonic form factors.

*3.3.2. The three-body nuclei* — Currently, the only complete study on elastic form factors of nuclei with mass number  $A = 3$  that uses  $\chi$ EFT potentials at N3LO ( $\nu = 4$ ), N3LO ( $\nu = 1$ ) e.m. currents and N4LO ( $\nu = 1$ ) charge operators has been carried out by Piarulli *et al.* in Ref. [48]. In that work, the calculations of the relevant matrix elements have been performed using wave functions obtained with the HH expansion method carried out in momentum space. The e.m. current and charge operators of Refs. [37, 46–48] have been sandwiched in between wave functions obtained from the NN(N3LO)+3N(N2LO) nuclear Hamiltonian, where the two-body interaction is from Ref. [98], while the 3N force has been taken at N2LO ( $\nu = 3$ ) with corresponding LECs constrained as in Ref. [100].

In Figure 12, the charge form factors ( $F_C$ ) of  ${}^3\text{He}$  and  ${}^3\text{H}$  are represented in the upper panels, while the bottom panels show the isoscalar ( $F_C^S$ ) and isovector ( $F_C^V$ ) combinations defined as

$$F_C^{S,V}(q) = \frac{1}{2}[2F_C(q, {}^3\text{He}) \pm F_C(q, {}^3\text{H})], \quad (31)$$

and normalized, respectively, to  $3/2$  and  $1/2$  at  $q = 0$ . The  $\chi$ EFT charge operator, schematically illustrated in Figure 5, does not involve unknown LECs up to N4LO. Results obtained with the charge operator at LO (N4LO) are represented by the cyan dotted (magenta hatched) band, and their thickness represent the spread in the calculations corresponding to a variation of the regularization cutoff ( $\Lambda = 500\text{--}600 \text{ MeV}$ ). The latter has been varied consistently in both the potentials and the currents. Hybrid results, obtained with wave functions from the AV18+UIX nuclear Hamiltonian, are also given in Figure 12. In particular, those based on the charge operator at LO (N4LO) are illustrated by the blue dashed line (red solid band). Note that one-body operators at LO are cutoff independent, which is why hybrid results at LO are given by a line. The calculated charge form factors are in excellent agreement with the experimental data for values of  $q < 3 \text{ fm}^{-1}$ . However, the positions of the zeros, as well as those of the maxima at  $q \sim 4 \text{ fm}^{-1}$ , are not well reproduced by the theory. The

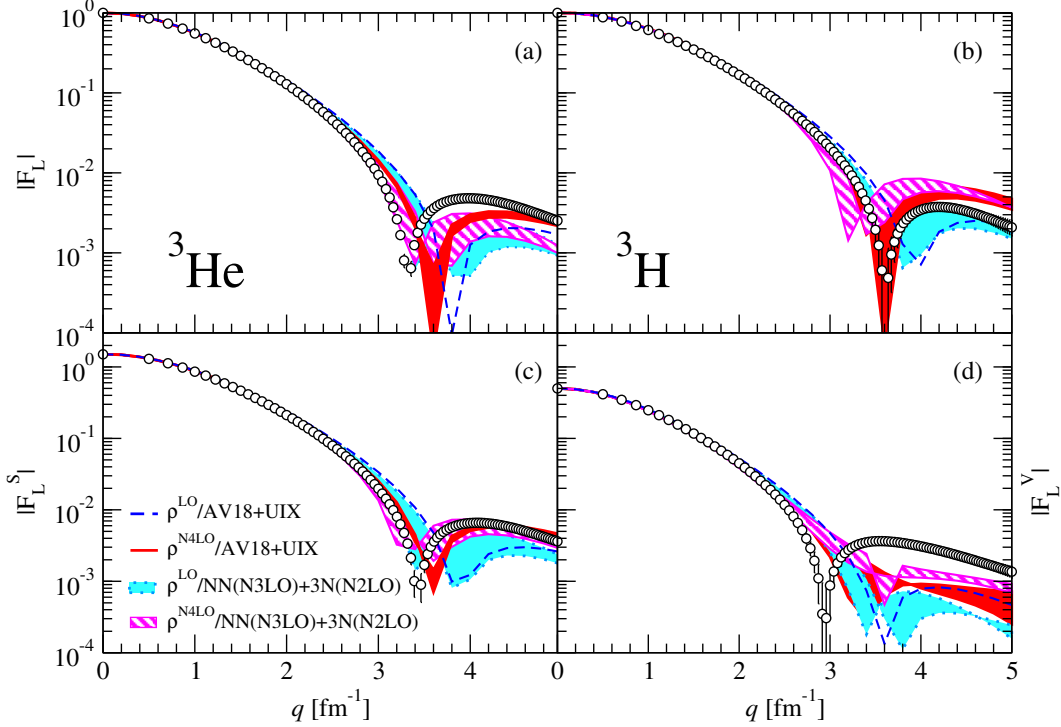


**Figure 12.** (Color online) The  ${}^3\text{He}$  (a) and  ${}^3\text{H}$  (b) charge form factors, and their isoscalar (c) and isovector (d) combinations from Ref. [48], compared with experimental data by Amroun *et al.* [167] (empty circles). Same color code as in Figure 10. Predictions corresponding to cutoffs  $\Lambda$  in the range (500–600) MeV are displayed by the bands.

results displayed in the bottom panels of Figure 12 suggest that larger (in magnitude) two-body isovector contributions to the e.m. charge operator are needed to reproduce the first zero in the isovector form factor,  $F_C^V$ .

The trinucleon magnetic form factors are given in Figure 13. Minimal LECs entering the N3LO contact currents—see panel (k) of Figure 3—have been taken from fits to NN scattering data [33, 98]. The LECs entering the isovector component of the  $\chi\text{EFT}$  e.m. current at N3LO, illustrated in panel (j) of Figure 3, have been saturated by the  $\Delta$ -isobar. The LEC associated with the isoscalar component of the same current, along with the LEC associated with the isoscalar N3LO contact current of non-minimal nature (see diagram in panel (k) of Figure 3) have been determined by reproducing the deuteron magnetic moment as well as the isoscalar combination of the trinucleon magnetic moments,  $\mu_S = [\mu({}^3\text{He}) + \mu({}^3\text{H})]/2$ . The remaining LEC, which multiplies an isovector non-minimal contact current at N3LO (see panel (k) of Figure 3) is fixed so as to reproduce the isovector combination of the trinucleon magnetic moments,  $\mu_V = [\mu({}^3\text{He}) - \mu({}^3\text{H})]/2$ . As before, in Figure 13, the top panels show the  ${}^3\text{He}$  and  ${}^3\text{H}$  magnetic form factors, while the bottom ones show the isoscalar ( $F_M^S$ ) and isovector ( $F_M^V$ ) combinations given by

$$F_M^{S,V}(q) = \frac{1}{2}[\mu({}^3\text{He})F_M(q, {}^3\text{He}) \pm \mu({}^3\text{H})F_M(q, {}^3\text{H})], \quad (32)$$

and normalized, respectively, to  $\mu_S$  and  $\mu_V$  at  $q = 0$ . In Figure 13, the color code is as in Figure 12, the only difference being that the vector e.m. currents include up to

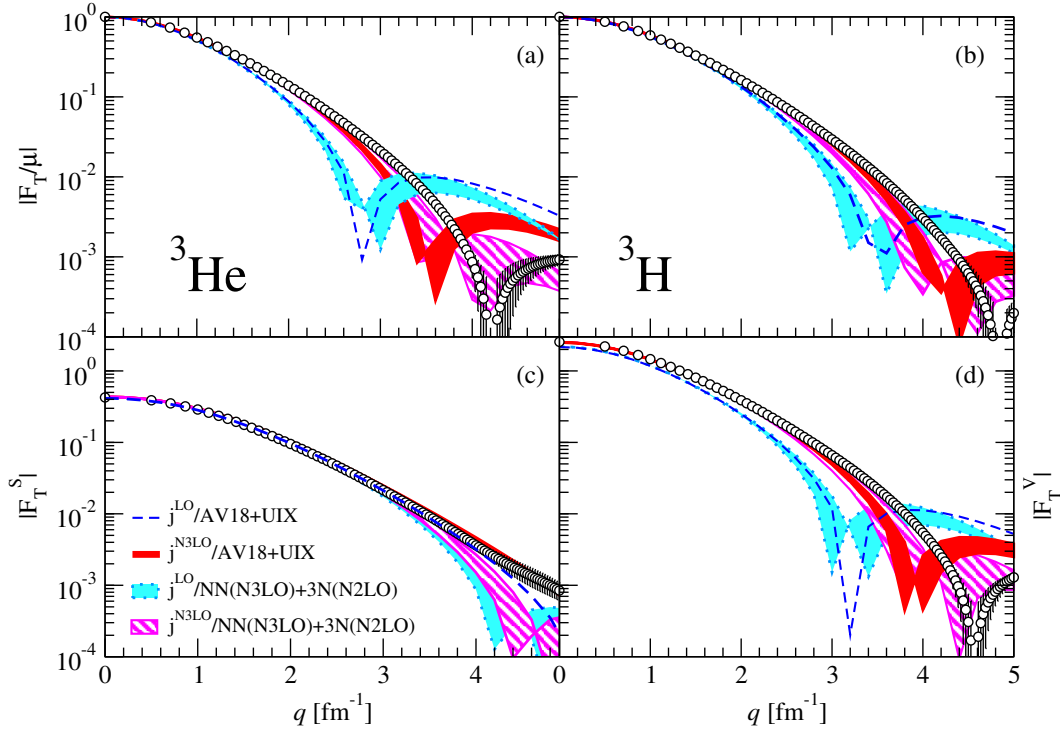


**Figure 13.** (Color online) The  ${}^3\text{He}$  (a) and  ${}^3\text{H}$  (b) magnetic form factors, and their isoscalar (c) and isovector (d) combinations from Ref. [48], obtained with the LO current operator, and with the inclusion of  $\chi\text{EFT}$  current operators up to N3LO, are compared with experimental data by Amroun *et al.* [167]. Same color code as in Figure 10. Predictions relative to cutoffs  $\Lambda$  in the range (500–600) MeV are displayed by the bands.

N3LO ( $\nu = 1$ ) corrections. As it is well known from studies based on the conventional approach (see Ref. [23]), two-body e.m. currents are crucial to improve the agreement between the observed positions of the zeros and the predicted ones at LO (or IA). Despite the excellent agreement between theory and experiment for  $q \leq 2 \text{ fm}^{-1}$ , the theory underpredicts the data at higher momentum transfers, while the zeros are found at lower values of  $q$  than observed. The theoretical description of the first diffraction region is still incomplete. This is a finding that confirms the conclusions of previous studies based on the conventional approach [21, 23, 90, 168]. It is interesting to point out that, in Ref. [48], different LEC parameterizations have been investigated. In particular, it has been found that if one fixes the isovector LEC to the  $np$  radiative capture cross section at thermal neutron energies, as opposed to  $\mu_V$ , the  $\chi\text{EFT}$  calculations of the magnetic form factors would lead to significantly better agreement with data over the whole range of momentum transfers, while overestimating the observed  $\mu_V$  by  $\simeq 3\%$  (see Figure 4 and associated discussion).

**3.3.3. The  ${}^4\text{He}$  nucleus** – *Ab-initio* calculations of the  ${}^4\text{He}$  elastic charge form factor have been performed by Schiavilla and collaborators [169] and reported in the review article of Ref. [23]. Since then, improved nuclear wave functions from conventional nuclear interactions, as well as calculations from chiral potentials, have appeared in the literature.

Results from Viviani *et al.* [170] are presented in Figure 14 along with the experimental



data by Frosch *et al.* [171]. Wave functions have been obtained using the HH method with the AV18+UIX nuclear Hamiltonian and consistent conventional MEC. The calculation in IA (blue dashed line) deviates from the experimental data for values of momenta larger than  $q \sim 2 \text{ fm}^{-1}$ , while the agreement with the experiment is restored once MEC are included (red solid line). The effect of two-body currents becomes more pronounced as  $q$  increases to larger values. In particular, two-body corrections lead to a very different diffraction minimum than that observed in the IA results, and in agreement with experiment.

In Ref. [172], an IA calculation with the AV18+UIX Hamiltonian has been performed using the EIH method, a different formulation of hyperspherical harmonics. A perfect agreement between results from these calculations (not shown in Figure 14, but displayed in Ref. [172]) and the IA results by Viviani *et al.* [170] has been obtained, indicating that a high level of accuracy has been reached in benchmarking few-body nuclei calculations, especially those of ground-state properties.

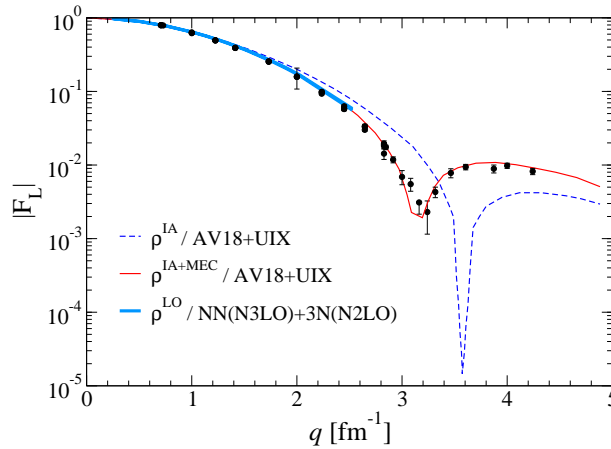


**Figure 14.** (Color online) Calculated  ${}^4\text{He}$  elastic charge form factor in IA (blue dashed line) and with MEC (red solid line) and nuclear wave functions from the AV18+UIX Hamiltonian from Ref. [170], compared with the IA (or LO) calculation (cyan band) with the chiral NN(N3LO)/3N(N2LO) potential from Ref. [172]. Experimental data are from Frosch *et al.* [171].

Also shown in Figure 14 is an IA (or LO) calculation (cyan band) from Ref. [172] obtained from  $\chi\text{EFT}$  potentials within the EIH method. The chiral Hamiltonians have been taken to consist of an NN force at N3LO ( $\nu = 4$ ) [98] and a 3N force at N2LO ( $\nu = 3$ ), with LECs parameterized as in Ref. [173] (choosing one LEC of natural value and fitting the other so as to reproduce the binding energy in  $A = 3$  nuclei) and as in Ref. [100] (fitting on the triton binding energy and empirical Gamow-Teller matrix element) at fixed cutoff  $\Lambda = 500 \text{ MeV}$ . The curves corresponding to the two above mentioned chiral Hamiltonians overlap in the figure and give rise to the thin band. At very low momentum, the conventional and  $\chi\text{EFT}$  approaches agree with each other. This is not very surprising, because they both use the same charge operator. Furthermore, conventional and chiral Hamiltonians give very similar results for the  ${}^4\text{He}$  radius, which determines the shape of the elastic form factor at low- $q$ . In fact, the point-proton radius is  $1.432(2) \text{ fm}$  [174] ( $1.464(2) \text{ fm}$  [172]) when the AV18+UIX

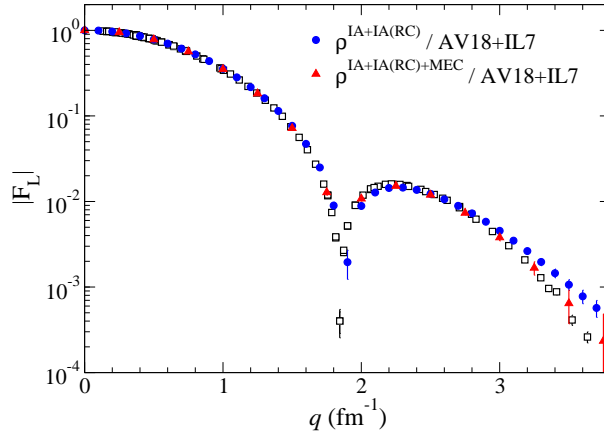


**Figure 15.** (Color online) GFMC calculations from Ref. [24] of the  $^{12}\text{C}$  elastic charge form factor obtained with the AV18+IL7 Hamiltonian in IA, comprehensive of relativistic corrections, (blue dots) and with MEC (red dots), compared with experimental data by de Vries *et al.* [178] (empty squares). Monte Carlo statistical errors are also shown.

(NN(N3LO)+3N(N2LO)) nuclear Hamiltonian is used. These calculated values are both close to the charged radius measured from elastic electron scattering, once the finite proton and neutron size are subtracted, yielding to 1.463(6) fm (see also Ref. [175] for more details).

Finally, we remind that new JLab data have been recently published in Ref. [176], where both experiment and conventional theory have been extended up to higher values of momentum transfer.

**3.3.4. Nuclei with  $A > 4$**  — There are few *ab-initio* calculations of elastic form factors for  $A > 4$  nuclear systems. Elastic charge and magnetic form factors of  $^6\text{Li}$  have been calculated in Ref. [177] from VMC nuclear wave functions obtained using the AV18+UIX nuclear Hamiltonian, and conventional MEC. In particular, the charge form factor has been found to be in excellent agreement with the experimental data, with conventional two-body corrections from the  $\pi$ -like charge operator improving on the IA results. The calculated transverse form factor, instead, has been found to deviate from the experimental data beyond values of momentum transfer  $q \sim 1 \text{ fm}^{-1}$ . Appreciable MEC effects for this isoscalar observable have been found for values of momentum transferred larger than  $3 \text{ fm}^{-1}$ , that is beyond the range of the available experimental data [23, 177]. The discrepancy with the experimental data has been attributed to a possible insufficient accuracy of the VMC nuclear wave functions, which could be resolved using improved GFMC evolutions [23, 177].

A comprehensive and computational demanding GFMC calculation of the  $^{12}\text{C}$  elastic charge form factor has recently appeared in the literature [24]. In that work, Lovato *et al.* have used the AV18+IL7 nuclear Hamiltonian and conventional MEC. The calculated  $^{12}\text{C}$  values of the ground-state energy and rms charge radius obtained with this Hamiltonian are -93.3(4) MeV and 2.46(2) fm, respectively, to be compared with the experimental values of -92.16 MeV and 2.471(5) fm. In Figure 15, the calculated  $^{12}\text{C}$  charge form factor [24] is shown along with the experimental data from Ref. [178]. Here, the one-body charge operator includes

relativistic corrections (RC) and the calculated form factor obtained from it is indicated by the blue circles, which are in very good agreement with the experimental data for values of momentum transferred  $q \lesssim 3 \text{ fm}^{-1}$ . Two-body charge operators used in the calculations include  $\pi$ -like and  $\rho$ -like exchange terms, as well as a  $\rho\pi\gamma$  transition current (see Sec. 2.1 for more details on conventional MEC operators). The full calculation with MEC (red triangles) provides an improved description of the data in the  $q \geq 3 \text{ fm}^{-1}$  region.

Since the review by Carlson and Schiavilla [23], thanks to the tremendous advancement of many-body computational techniques, accurate nuclear wave functions are now available for up to  $A \sim 20$  nuclear systems. This opens up the possibility of studying the charge and magnetic spatial distributions of more complex nuclear systems. In addition, chiral potentials and e.m. currents are now available and in the future studies, such as those of Refs. [24, 177], can be performed with  $\chi$ EFT and extended to other nuclei. Effects of two-body e.m. currents have been proved to be significant and crucial for an accurate theoretical description of the available experimental data. It would also be interesting to study their contributions in neutron-rich nuclei that display halo features, such as, *e.g.*, the  ${}^6\text{He}$  nucleus. Electron scattering experiments on unstable nuclei have not been carried out yet. However, plans to measure charge distributions of neutron-rich nuclei have been presented at both European (FAIR) and Japanese (RIKEN) facilities. Such electron scattering reactions on unstable nuclei, to be performed in storage rings, can potentially reveal new interesting nuclear structure properties, for which the community can provide theoretical guidance due to the high level of reliability that is being reached by *ab-initio* calculations.

### 3.4. Inelastic scattering

The electron scattering off a nucleus is inelastic when both momentum  $\mathbf{q}$  and energy  $\omega$  are transferred to the target. In this case, the final state of the nucleus is different from the initial state (typically the ground state), *i.e.*,  $|\Psi_f\rangle \neq |\Psi_i\rangle$ . In the case that only the scattered electron is measured and no specific final hadronic state is selected, one obtains an inclusive unpolarized double differential cross section. In the usual one-photon-exchange approximation and for ultrarelativistic electrons, such cross section in the laboratory is<sup>†</sup>

$$\frac{d^2\sigma}{d\Omega_e d\omega} = \sigma_M \left[ \frac{Q_\mu^4}{q^4} R_L(\omega, \mathbf{q}) + \left( \frac{Q_\mu^2}{2q^2} + \tan^2 \frac{\theta_e}{2} \right) R_T(\omega, \mathbf{q}) \right], \quad (33)$$

where the Mott cross section,  $\sigma_M$ , has been defined in Eq. (16). The dynamical quantities of interest are the longitudinal ( $L$ ) and transverse ( $T$ ) response functions, defined as

$$\begin{aligned} R_L(\omega, \mathbf{q}) &= \sum_f |\langle \Psi_f | \rho(\mathbf{q}) | \Psi_0 \rangle|^2 \delta \left( E_f - E_0 - \omega + \frac{\mathbf{q}^2}{2M_A} \right) \\ R_T(\omega, \mathbf{q}) &= \sum_f \sum_{\lambda=\pm 1} |\langle \Psi_f | J_\lambda(\mathbf{q}) | \Psi_0 \rangle|^2 \delta \left( E_f - E_0 - \omega + \frac{\mathbf{q}^2}{2M_A} \right), \end{aligned} \quad (34)$$

where the recoil energy in the  $\delta$ -function includes the mass of the target  $M_A$ . Here the symbol  $\sum_f$  indicates a sum over the final states of the nucleus, including both the finite (sum) and continuum (integral) ones. The longitudinal and transverse response functions are obtained from the charge and transverse current operator, respectively. The longitudinal part can be disentangled from the transverse one by using the Rosenbluth separation method [179]. Because this procedure is based on the one-photon-exchange assumption, it is valid only for

<sup>†</sup> Note that, with respect to Eq. (15), here a different convention for the charge is used, namely  $\frac{e^2}{\hbar c}$ .

light nuclei. Indeed, data from different laboratories (mostly Bates and Saclay), extracted via the Rosenbluth separation, agree fairly well with each other for light mass targets. From the definitions of Eq. (34), it is clear that a comprehensive study of the nuclear response functions requires not only the description of the initial state wave function and of the four-body current  $j^\mu$ , but also of the final state wave functions, which could be in the continuum.

Since  $\omega$  and  $\mathbf{q}$  can vary independently, one can study the responses as a function of the energy  $\omega$  while keeping the momentum  $q = |\mathbf{q}|$  fixed or, vice versa, one can vary the momentum  $q$  and keep  $\omega = E_f - E_i$  unchanged. In the last case, the response functions are called inelastic or transition form factors, since the nucleus undergoes a transition from the initial state  $|\Psi_i\rangle$  to the specified final state  $|\Psi_f\rangle$ , and correspond to the quantities introduced in Eqs. (18) and (19).

Below, we present the recent progress in *ab-initio* calculations of inelastic response functions and form factors and compare to the available experimental data. We divide the discussion into different subsections devoted to nuclei with increasing mass number, ranging from the deuteron to  $^{12}\text{C}$ .

*3.4.1. The deuteron and the  $A = 3$  nuclei* – In the case of  $A = 2$  and 3 nuclei, the final states  $|\Psi_f\rangle$  can be exactly evaluated with computational few-body techniques also in the continuum, thus the longitudinal and transverse response functions,  $R_L$  and  $R_T$  of Eqs. (34), are obtained by summing over all the final states. Alternatively, when specific break-up channels are selected, exclusive processes can be studied.

Results for the deuteron obtained within the conventional approach have been already discussed in earlier review articles (see, *e.g.*, Refs. [23, 180]). Recently, Yang and Phillips performed a  $\chi\text{EFT}$  calculation of the deuteron longitudinal response function in Ref. [181]. They have employed N2LO ( $\nu = 3$ ) wave functions from  $\chi\text{EFT}$  power counting and their subtractive renormalization method [182]. By using the  $\text{LO}^\dagger$  charge operator they obtained results which, at low energy and low momenta, are in agreement with conventional calculations by Arenhövel *et al.* carried out in Ref. [183] using the Bonn potential [184].

The inelastic responses of  $^3\text{H}$  and  $^3\text{He}$  with conventional potentials and currents in IA have been discussed in the review by Carlson and Schiavilla [23]. Conventional two-body currents have been recently included in the studies of Refs. [185, 186], and reviewed by Golak *et al.* in Ref. [168], while  $\Delta$ -isobar excitations below pion threshold have been studied in Refs. [187, 188]. For the inelastic electron scattering of the three-body nuclei not much has been done using the  $\chi\text{EFT}$  approach.

From the available calculations of  $A = 2$  and 3 nuclei, it is generally observed that the effect of two-body operators is much larger on the transverse response,  $R_T$ , than in the longitudinal one,  $R_L$ . This can be easily understood in the  $\chi\text{EFT}$  language. In fact, two-body corrections appear at NLO and at N3LO for the current and charge operator, respectively (see Table 1).

Because the longitudinal response  $R_L$  is not very sensitive to two-body operators, for  $A \geq 3$  nuclei one can focus on studying the sensitivity of this observable to 3N forces, while keeping the charge operator in IA. The three-body nuclei have been studied for example in Ref. [191] employing the LIT method. Conventional 3N forces were found, *e.g.*, to reduce  $R_L$  in the quasi-elastic peak by 5-10% in the momentum transfer regime between 174 MeV

<sup>†</sup> Note that the authors use a slightly different power counting, in particular they count  $Q/m$  as  $Q^2/\Lambda_\chi^2$  as opposed to  $Q/\Lambda_\chi$ . This demotes the relativistic one-body operator of panel (b) and the two-body operator of panel (c) illustrated in Figure 5 to N4LO.

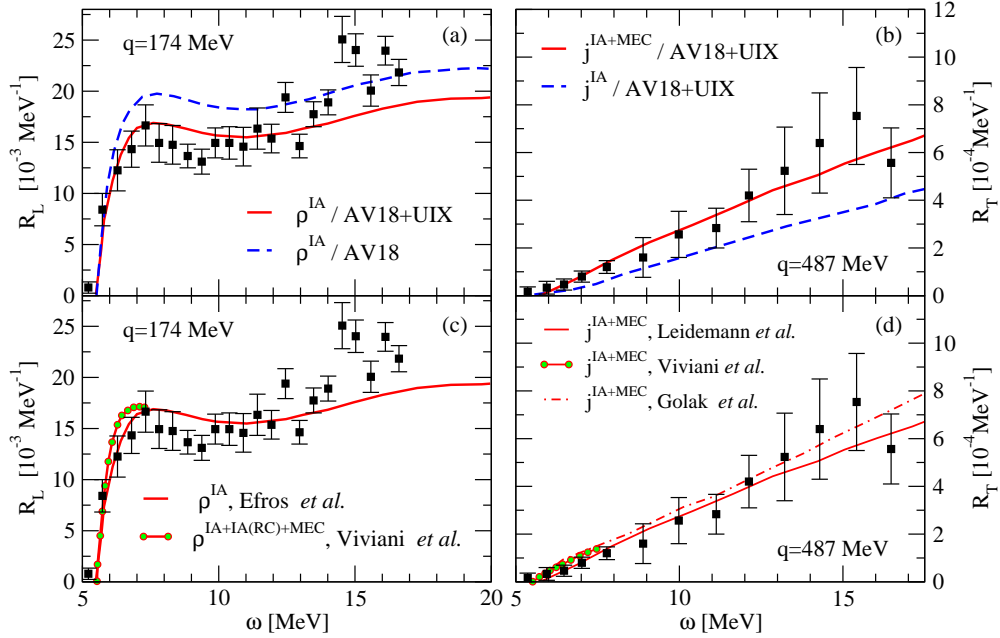


**Figure 16.** (Color online) Calculations for the  ${}^3\text{He}$  longitudinal (left panels) and transverse (right panels) response functions at  $q = 174$  and  $487$  MeV, respectively, in comparison to data by Retzlaff *et al.* from Ref. [189] and from Ref. [190], respectively. Panel (a): calculations from Ref. [191] with (red solid curve) and without (blue dashed curve) 3N forces. Panel (c):  $R_L$  calculations by Efros *et al.* from Ref. [191] compared to those by Viviani *et al.* [186] both obtained with the AV18+UIX Hamiltonians, but different charge operators (see text). Panel (b):  $R_T$  calculations from Ref. [192] with (red solid curve) and without (blue dashed curve) MEC, obtained from the AV18+UIX Hamiltonian. Panel (d):  $R_T$  calculations by Leidemann *et al.* from Ref. [192] in comparison to those by Viviani *et al.* [186] and by Golak *et al.* [168], where the same Hamiltonian (AV18+UIX) has been used, but slightly different current operators, including MEC, have been implemented (see also text).

and about 400 MeV. However, 3N forces can also have much larger effects. In Figure 16(a), the threshold behavior of  $R_L$  is shown in the case of  ${}^3\text{He}$  at  $q = 174$  MeV: 3N forces (red solid curve with the AV18+UIX potential) lead to a quenching of the response function with respect to the calculation without 3N forces (blue dashed curve with the AV18 potential) and they were proven to be necessary to obtain a satisfactory description of the experiment. In Figure 16(c), a comparison with another calculation by Viviani *et al.* [186] is shown, where the same potentials were used and charge operators included MEC (green dots connected by red line). In Ref. [186], it was found that MEC have a negligible effect in this kinematical region, thus, the difference between the two calculations with the AV18+UIX force is likely coming from the different numerical methods used. It is worth noticing that such theoretical difference is much smaller than the experimental error. Furthermore, an even better agreement between the LIT calculations by Efros *et al.* [191] and the variational calculations by Viviani

*et al.* [186] is found for larger momentum transfers, as shown in Ref. [191].

In case of the transverse response function,  $R_T$ , it is generally observed that two-body currents have a substantial contribution on the total strength. For the three-body nuclei,  $R_T$  was calculated, for example, in Refs. [168, 186, 192] with the AV18+UIX force and MEC and in Ref. [193] with the Bonn potential [184], and the Tucson-Melbourne [194] 3N force and corresponding MEC. In the latter calculations, it has been shown that, for momentum transfer values of 174 MeV and 400 MeV, the two-body currents enhance the quasi-elastic peak by about 10% and 6%, respectively. The largest MEC effects have been found away from the quasi-elastic peak and particularly close to threshold, where two-body currents can enhance the strength by up to 200%. Generally, exchange currents contributions relative to the IA are enhanced when the difference  $|\omega - \omega_{q.e.}|$  is larger. This is not unexpected as the quasi-elastic peaks correspond to the maximum contributions of the one-body current.

In Figure 16(b) and (d), we show the case of the  ${}^3\text{He}$  transverse response at  $q = 487$  MeV and discuss the threshold results obtained in calculations that utilized the AV18+UIX Hamiltonian. In panel (b), calculations by Leidemann *et al.* from Ref. [192] obtained with the LIT method point to the importance of MEC. The curve including MEC (red solid) leads to a considerably improved agreement with experimental data with respect to the IA calculation (blue dashed curve). In Figure 16(d), results by Leidemann *et al.* from Ref. [192] are compared to those by Viviani *et al.* from Ref. [186] (green dots connected by red line) and by Golak *et al.* from Ref. [168] (dash-dotted curve). Besides using the same Hamiltonian, those calculations adopt slightly different implementations of the current operator. Calculations by Leidemann *et al.* include relativistic corrections to the one-body operator and use the method devised by Arenhövel and Schwamb [195] in coordinate space to derive the MEC. Calculations by Golak *et al.* do not include Coulomb interactions in the final state, do not include relativistic corrections to the current operator and implement MEC obtained according to the momentum-space method of Riska [196] (both methods for the MEC derivation lead to the same MEC contributions). Calculations by Viviani *et al.* instead employ more sophisticated MEC, which also include contribution from the  $\Delta$ -excitation. One can observe that all the three calculations nicely agree with data and with each other, proving that the dynamic of the few-body system is well under control.

At momentum transfer values of the order of 500 MeV and higher, relativity starts to play a role. Relativistic effects in  $A = 3$  due to the frame dependence were studied, *e.g.*, in Refs. [197, 198].

While inclusive processes can help planning for future exclusive experiments, exclusive reactions are much richer in the information they provide about the nuclear dynamics. In the case of three-body nuclei, the exclusive  $p-d$  break-up has been studied within the Faddeev approach and using conventional forces and currents [185]. It has been observed that the final state interaction plays an important role, however not many experimental data are available to compare.

**3.4.2. The  ${}^4\text{He}$  nucleus** — For four-body systems the explicit calculation of all final states in the continuum becomes more cumbersome, thus often approximations of various kinds are introduced. The simplest model for the response function is obtained under the assumption that the photon is absorbed by one nucleon only (via a one-body operator) and that the hadronic final state is just a free propagation (plane wave) of the knocked out nucleon that does not interact with the remaining spectator (A-1)-nucleus. Such an approximation is named plane wave impulse approximation (PWIA). Under this assumption and neglecting excitations

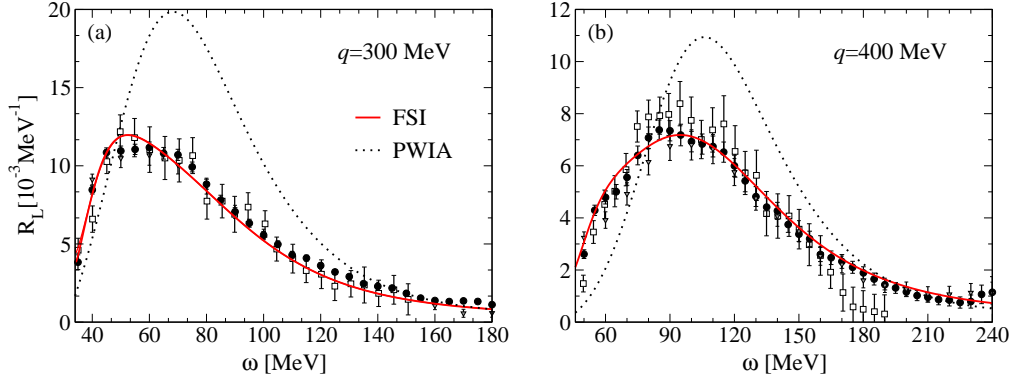


**Figure 17.** (Color online) Longitudinal response function  $R_L$  for  ${}^4\text{He}$  from Ref. [200] : PWIA (black dotted line) versus calculation with the FSI (red solid line) with the AV18+UIX potential. The charge operator is used in IA. Experimental data are from Bates [201] (squares), Saclay [202] (circles).

of the residual nucleus $\dagger$ , the longitudinal response function can be obtained from the ground-state nucleon momentum distribution  $N(\mathbf{p})$  as [23]

$$R_L^{\text{PWIA}}(\omega, q) = \int d\mathbf{p} N(\mathbf{p}) \delta \left( \omega - \frac{(\mathbf{p} + \mathbf{q})^2}{2m} - \frac{\mathbf{p}^2}{2(A-1)m} - E_s \right), \quad (35)$$

with  $m$  being the mass of the struck nucleon (dominantly the proton) and  $E_s$  the proton separation energy. The PWIA does not consider the antisymmetrization of the final state and ignores the effect of the final state interaction (FSI). It is thus expected to be better at high-momentum transfer, where the FSI is small. It also neglects the effect of two-body currents. In the quasi-elastic regime, corresponding to momentum transfers of a few hundreds MeV and energies around  $\omega_{q.e.} \approx q^2/2m$ , one can envision that the electron has scattered elastically with a single nucleon. Thus, the PWIA can be considered the base line in a comparison with more sophisticated calculations.

For mass number  $A = 2$  and 3 nuclei, the PWIA fails to reproduce experimental data for  $R_L$  below momentum transfer  $q \sim 500$  MeV, see, *e.g.*, Ref. [23]. In particular, it typically yields to too much strength near the quasi-elastic peak and too little strength at energies below and above this peak. When the FSI is included, the agreement with experiment is restored. The same conclusions were drawn for the  ${}^4\text{He}$  nucleus, in the first calculation of  $R_L$  with the Laplace transform approach [203, 204] (already reported in the review [23]) and in a LIT calculation with a central NN potential model [205] and then also confirmed in a more recent realistic calculation [200].

In Figure 17, we show the longitudinal response function of  ${}^4\text{He}$  from Ref. [200] calculated with the AV18+UIX potential for two values of momentum transfer  $q = 300$  and 400 MeV. In these calculations the charge density operator is used in IA. The latter is expanded in multipoles and then each multipole response function is separately calculated using the LIT method in conjunction with an EIH expansion. For these values of momentum transfer a numerical precision of 1% is reached when multipoles up to  $J = 6$  are summed up. What is

$\dagger$  Note that, in principle, one may use the spectral function approach (see, *e.g.*, Ref. [199]) to account for excitations of the residual nucleus.

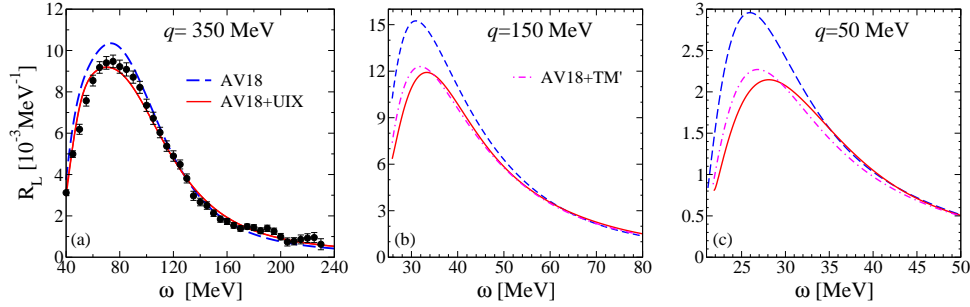


**Figure 18.** (Color online) Effect of 3N forces on the longitudinal response function  $R_L$  of  ${}^4\text{He}$  at different momentum transfers. Calculations from Refs. [200, 207] obtained with the AV18 (blue dashed curve), AV18+UIX (red solid curve) and AV18+TM' (magenta dash-dotted curve) potentials. The current operator has been used in IA. Data are from Saclay [202].

evident from Figure 17 is that the PWIA (black dotted curve) is rather poor. When the FSI is included using the LIT method (red solid curve) the agreement with the experimental data is restored. The advantage of the LIT method over the Laplace transform used in Ref. [204] is that the first method allows for a stable inversion of the transform [206], so a direct comparison of the theoretical response function to the experimental data is possible. This is preferable with respect to applying the integral transform to the experimental data, as the latter usually requires an extrapolation of the data in the high energy tail. Ultimately, the advantage of a direct comparison of the theoretical and experimental  $R_L$  is that one obtains the  $\omega$ -dependence of the FSI effects as an additional information, as shown in Figure 17. For the chosen kinematical values, the FSI is important also in the region of the quasi-elastic peak.

It is interesting to study the sensitivity of the longitudinal response functions to different Hamiltonians, with emphasis on 3N force effects. In Figure 18, results for  ${}^4\text{He}$  obtained with the LIT method in Ref. [200, 207] are shown. In those calculations, conventional potentials have been used and the charge operator has been kept in IA. One observes a rather strong effect of 3N forces: the difference between calculations with the AV18 only (blue dashed curve) and those comprehensive of the UIX three-body force (red solid curve) is increasing at low  $q$ . At  $q = 350$  MeV, as shown in panel (a), the UIX leads to about a 10% reduction of the strength and improves the description of the data. At  $q = 150$  and 50 MeV, presented in panel (b) and (c), where no experimental data exist, the UIX quenches the response function by up to 50%. This fact is confirmed when using a different three-body force like the TM' potential [194] (magenta dash-dotted curve). With different three-body Hamiltonians a 10% variation in  $R_L$  is observed. Calculations with the  $\chi\text{EFT}$  approach are in progress [208] and it is worth recalling that the TM' force is basically the long range part of the  $\chi\text{EFT}$  three-body force at N<sup>2</sup>LO ( $\nu = 3$ ). Because of the sensitivity of  $R_L$  to 3N forces and because of such 10% variation with different 3N forces, precise future experiments can help to better constrain realistic three-body Hamiltonians. Thus, the longitudinal response function of  ${}^4\text{He}$  is an e.m. observable, complementary to the hadronic ones, that can potentially allow to study and constrain 3N forces.

In case of the transverse response function,  $R_T$ , where two-body currents contribute already at NLO ( $\nu = -1$ ) as suggested by the  $\chi\text{EFT}$  power counting, one can speculate that their strength enhancing effect will in part cancel the quenching due to the 3N forces that was observed in  $R_L$ . However, no calculation studying both the effect of switching on and off 3N



forces and MEC exists. The first calculation of the transverse response function of  ${}^4\text{He}$  was performed by Carlson and Schiavilla using the Laplace transform [204]. Conventional three-body Hamiltonians, always comprehensive of 3N forces, and MEC have been implemented. A large effect of two-body currents has been pointed out at momentum transfer  $q = 300$  and  $400$  MeV, leading to an enhancement of the strength by 20%, with respect to the IA. The major contribution was shown to come from OPE and proven necessary to describe the data. A comparison to the experiment could, though, only be done by Laplace transforming the data, so it was not possible to resolve the  $\omega$  dependence of the MEC. A direct comparison to data was done instead in Ref. [209] using the LIT method. There, however, a semirealistic NN potential was utilized and approximations were introduced in the two-body currents. With this simplified model, two-body currents were not found to be very important, probably due to the missing one-pion exchange character both in the NN force and corresponding MEC.

As already mentioned, from inelastic electron scattering experiments other observables can be extracted. For example, the inelastic charge form factor,  $F_L^{tr}(q)$ , pertaining to the transition from the ground state to the resonant first  $0^+$  excited state of  ${}^4\text{He}$  was recently studied with realistic Hamiltonians in Ref. [172]. The transition form factor corresponds to the inelastic longitudinal response function  $R_L(\omega, q)$  integrated around the energy of the  $0^+$  resonance. Because in this case  $J_f = J_0 = 0$ , effectively only the monopole part of the charge operator contributes to this transition. Several experimental data sets are available [210–212], where the background of other multipoles and of the monopole high energy tail has been subtracted. The first *ab-initio* calculation was performed by Hiyama *et al.* in Ref. [213] with the AV8' two-body potential [65], a reduction of the AV18 force, in combination with a simple central 3N force. The two free parameters of the latter have been calibrated to reproduce the  ${}^3\text{H}$  and  ${}^4\text{He}$  binding energies. As shown in Figure 19, a rather good description of the data for  $F_L^{tr}(q)$  has been achieved (black dash-dotted curve). More recent calculations of  $F_L^{tr}(q)$  have been performed with the LIT method, using realistic Hamiltonians both from conventional theory as well as from  $\chi\text{EFT}$ . As shown in Figure 19, the following Hamiltonians have been used: the AV18+UIX (red solid curve) and the NN(N3LO)+3N(N2LO) (magenta band) chiral forces. For the latter, the NN potential was used at N3LO ( $\nu = 4$ ) [98] and the 3N force at N2LO ( $\nu = 3$ ). The band width is obtained by using two different parameterization of the LECs in the 3N force, following Ref. [100] and Ref. [173], respectively. A dramatic dependence of the results on the starting three-body Hamiltonian is observed. Three different Hamiltonians which describe the  ${}^4\text{He}$  ground-state energy within 1% from experiment show large differences in their predictions for  $F_L^{tr}(q)$ . This is quite surprising and highlights the richness of the dynamical information provided by inelastic observables. The failure of the realistic forces to reproduce the available experimental data for  $F_L^{tr}(q)$  is not believed to be cured by two-body charge operators, as they appear only at N3LO ( $\nu = 0$ ) in  $\chi\text{EFT}$  and thus are not expected to play a major role. This example of disagreement between state-of-the-art theoretical calculations and experiment will hopefully stimulate further theoretical and experimental activity. From the theoretical point of view, the first excited state of  ${}^4\text{He}$  can be tackled with alternative few-body approaches. Interesting other features, such as its relation to collective modes, can also be explored, see, *e.g.*, Ref. [214]. From the experimental point of view, the failure of the realistic forces to reproduce the available experimental data for  $F_L^{tr}(q)$  has motivated new proposals to measure the monopole form factor via higher accuracy electron scattering at the S-DALINAC [215] and via the  ${}^4\text{He}({}^4\text{He}, {}^4\text{He}){}^4\text{He}^*$  reaction at LNS in Catania with the spectrometer MAGNEX [216].

Regarding exclusive electron scattering reactions, the  ${}^4\text{He}(e, e'p){}^3\text{H}$  process was studied, *e.g.*, by Quaglioni *et al.* in Ref. [217]. Because often  $(e, e'p)$  experiments are performed to

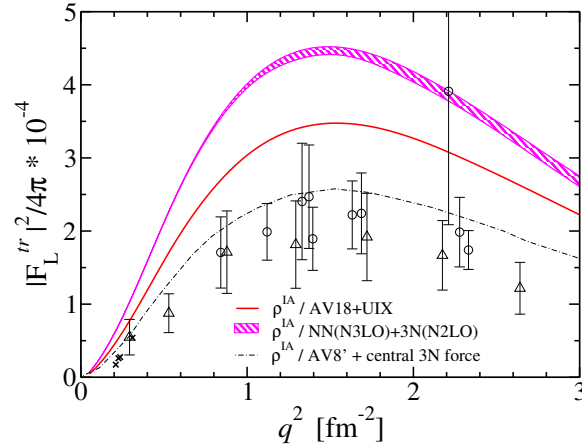


**Figure 19.** (Color online) Transition charge form factor from the ground state to the first  $0^+$  excited state of  ${}^4\text{He}$  with different Hamiltonians and in IA for the charge operator. Theoretical calculations are taken from Ref. [172] for the AV18+UIX (red solid curve) and the NN(N3LO)+3N(N2LO) chiral forces (magenta band), while the result with the AV8' + central 3N force (black dash-dotted curve) is taken from Ref. [213]. Experimental data are from Köbschall *et al.* [212] (circles), Frosch *et al.* [210] (triangles) and Walcher [211] (crosses).

study the structure of target nucleus [218] and spectroscopic factors are extracted under the assumption of direct knock-out of the proton neglecting the FSI, a check on such assumptions for  $A = 4$  is very instructive. In Ref. [219], by using the LIT method and a simple semirealistic potential, it was shown that FSI effects are rather large, especially at low  $q$ , amounting up to 40%. It was concluded that the extraction of spectroscopic factors is more viable in the kinematic regions with high momentum transfer and small missing momentum. Very recently, a study on exclusive processes including the  ${}^3\text{He}(e, e'p){}^2\text{H}$  and  ${}^4\text{He}(e, e'p){}^3\text{H}$  reactions has been carried out in Ref. [220], extending the applications of MEC to high energies. It is found that FSI are of utmost importance and necessary for a satisfactory description of data.

The  $(e, e'NN)$  reaction, in which two nucleons are knocked out and detected, is also considered an important tool to investigate NN correlations in nuclei. The  ${}^4\text{He}(e, e'd)d$  process was studied theoretically in Ref. [221] using a semirealistic interaction and an exact and consistent treatment of the FSI. The latter was found to be substantial, pointing out the importance of having all relevant effects under control if one wants to study NN correlations. Although several model studies are available in the literature, Unfortunately, fully *ab-initio* exclusive calculations, where the Schrödinger equation is solved exactly, are not yet available in more complex nuclei, mostly because of the major stumbling block of dealing with the final states in the continuum.

**3.4.3. Transition form factors and sum rules in  $A > 4$  nuclei** — There exist few calculations of transition form factors in  $A > 4$  nuclei. Inelastic transition form factors of  ${}^6\text{Li}$  have been studied in Ref. [177] using VMC wave functions for the ground and excited states obtained from the AV18+UIX potential. In that work, conventional and consistent MEC have been used and they have been found to significantly improve the agreement between theory and experiment for the calculated longitudinal and transverse transition form factors to a number of low-lying excited states of  ${}^6\text{Li}$ .

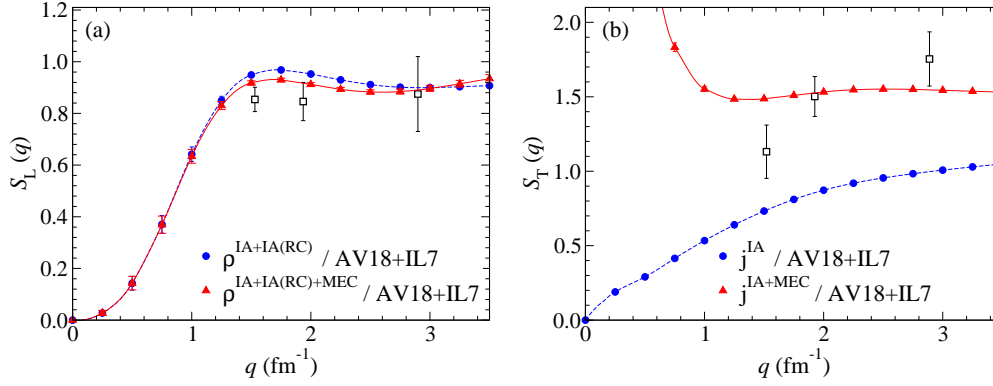


**Figure 20.** (Color online) Calculated GFMC longitudinal, panel (a), and transverse, panel (b), sum rules for  $^{12}\text{C}$  from Ref. [24] obtained with the AV18+IL7 Hamiltonian and consistent MEC. IA and IA+IA(RC) results (blue dots) and with MEC (red triangles) are compared with the experimental values (empty squares), inclusive of tail corrections (see text and Ref. [24] for more details).

Very recently, GFMC calculations of the charge form factors and sum rules of e.m. response functions in  $^{12}\text{C}$  have been carried out by Lovato *et al.* in Ref. [24]. The study of e.m. inelastic responses in  $^{12}\text{C}$  is particularly interesting in view of the recent anomaly observed in the neutrino quasi-elastic charge-changing scattering data on  $^{12}\text{C}$  measured at MiniBooNE [4]. In particular, the measured cross section has been found to be larger than predicted by previous theoretical calculations. The latter, however, were not carried out within strictly *ab-initio* frameworks.

The *ab-initio* study of Ref. [24] has aimed at quantitatively evaluating, *albeit* in processes induced by e.m. probes, the effect of MEC on calculated  $^{12}\text{C}$  response functions. In particular, Lovato *et al.* calculated the  $^{12}\text{C}$  e.m. sum rules [222]

$$S_{L/T} = C_{L/T} \int_{\omega_h}^{\infty} d\omega \frac{R_{L/T}(q, \omega)}{G_E^p(Q^2)}, \quad (36)$$

where  $R_{L/T}$  are the longitudinal and transverse response functions of Eq. (34), and the  $C_{L/T}$  factors are defined as

$$C_L = \frac{1}{Z}, \quad C_T = \frac{2}{Z\mu_p^2 + N\mu_n^2} \frac{m^2}{q^2}. \quad (37)$$

The non-energy weighted sum rules given in Eq. (36) can be expressed as ground-state expectation values by using closure relations, *i.e.*,

$$S_{L/T} = C_{L/T} \left[ \langle \Psi_0 | O_{L/T}^\dagger(\mathbf{q}) O_{L/T}(\mathbf{q}) | \Psi_0 \rangle - |\langle \Psi_0; \mathbf{q} | O_{L/T}(\mathbf{q}) | \Psi_0 \rangle|^2 \right], \quad (38)$$

where  $O_L$  and  $O_T$  are the charge and current operators, respectively, and  $|\Psi_0; \mathbf{q}\rangle$  denotes the ground state of the nucleus recoiling with total momentum  $\mathbf{q}$ .

The GFMC results for  $^{12}\text{C}$ , based on the AV18+IL7 nuclear Hamiltonian and consistent conventional MEC, are shown in Figure 20. In the figure, blue dots are obtained in IA (and IA+IA(RC) for the one-body charge operator), while red triangles include MEC corrections due to  $\pi$ -like and  $\rho$ -like exchanges, to the  $\rho\pi\gamma$  transition current, and to OPE currents involving the excitations of  $\Delta$  intermediate states. The comparison to the experimental data is

not straightforward. In fact, in electron scattering, space-like virtual photons are exchanged for which  $|\mathbf{q}| > \omega$ . Therefore, in order to compare the theoretical results with the data one has to estimate the strengths in the energy region that is not accessed experimentally. In Figure 20, the experimental points (open squares in the figures) have been obtained by integrating the available data from Ref. [223] over the accessible energy interval. The tail contribution, necessary to perform the integral appearing in Eq. (36) up to infinity, has been estimated by assuming that at these energies the  $^{12}\text{C}$  response is proportional to that of the deuteron, which can be calculated exactly (see [24] for details). MEC contributions are found to be small in  $S_L$ , and rather large in  $S_T$  where they can increase the IA results by up to a 50%. The study of Ref. [24], and that of Ref. [224] reporting on GFMC calculations of  $^{12}\text{C}$  sum rules of responses induced by neutral weak currents, have found that calculated MEC effects are large and should not be ignored in a careful interpretation of available experimental data. These findings may have implications for the above mentioned anomaly observed at MiniBooNE, and other quasi-elastic scattering data on nuclei.

#### 4. Photonuclear reactions

In this section, we discuss processes in which real photons interact with the nucleus, by either being absorbed by it, causing its excitation or break-up, or emitted, for example, in  $\gamma$ -decay reactions or as a byproduct of fusion reactions. To the last class belong radiative capture processes, which, at very low-energies, are particularly relevant for astrophysical studies. Photo-absorption processes are schematically represented in Figure 21, where a real photon  $\gamma$  transfers an energy  $\omega = |\mathbf{q}|$  to the nucleus, which undergoes a transition from an initial to a final state, denoted by  $|\Psi_i\rangle$  and  $|\Psi_f\rangle$ , respectively. Depending on the photon energy, the final state can consist of a nuclear bound excited state, or an excited state in the continuum, where the nucleus breaks up in a number of clusters. At even higher energies, photoproduction of other particles, such as pions, can be observed, but we will consider only processes below such energies.

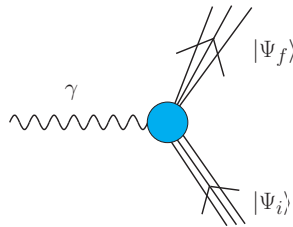


**Figure 21.** (Color online) Feynman diagram of the interaction of a single real photon with the nucleus.

Below, we devote Section 4.1 to photoabsorption reactions, Section 4.2 to radiative capture reactions, and Section 4.3 to e.m. transitions in low-lying nuclear states.

##### 4.1. Photoabsorption reactions

Photoabsorption reactions have been extensively studied in the '70s in a number of experiments on stable nuclei. The main feature of the measured cross sections is a very pronounced peak, referred to as the giant resonance peak, that is located at energies  $\omega$  of

about 10–30 MeV. It took quite a long time until such observations could be interpreted in terms of microscopic *ab-initio* theories, and this is due to the difficulty of accounting for correlations in both the ground and final states. At the above mentioned photon energies, the excited nucleus can, in fact, break into either different clusters made of lighter nuclei or even into all its constituents (in the case of very light nuclei). Accounting for all these complicated final states is one of the main difficulties from the theoretical point of view.

The general form of the nuclear matrix element entering the photodisintegration cross section is given by

$$N_\lambda = \langle \Psi_f | j_\lambda(\mathbf{q}) | \Psi_i \rangle, \quad (39)$$

where typically the initial state is the ground state, *i.e.*,  $\Psi_i = \Psi_0$ . Photodisintegration observables provide a good tool to study two-body e.m. currents because they are not dominated by the charge operator  $\rho(\mathbf{q})$ , but rather by the transverse current operator  $j_\lambda(\mathbf{q}) = \mathbf{e}_\lambda \cdot \mathbf{j}(\mathbf{q})$ , with  $\lambda = \pm 1$ , where  $\mathbf{e}_\lambda$  is a spherical component of the photon polarization vector. The latter is orthogonal to the direction of propagation  $\mathbf{q}$  of the real photon. In the case of unpolarized photons, we have to sum over  $\lambda = \pm 1$ . In inclusive processes, *i.e.*,  $\gamma + A \rightarrow X$ , no specific hadronic final state  $X$  of the  $A$ -body nucleus is measured, thus a sum over all possible final states has to be performed. The expression for the total cross section then becomes

$$\sigma_\gamma(\omega) = \frac{4\pi^2\alpha}{\omega} R_T(\omega), \quad (40)$$

where

$$R_T(\omega) = \frac{1}{2J_0 + 1} \sum_{\lambda=\pm 1} \sum_f |\langle \Psi_f | j_\lambda | \Psi_0 \rangle|^2 \delta\left(E_f - E_0 - \omega + \frac{\omega^2}{2M_A}\right) \quad (41)$$

is the transverse response function, already introduced in Eq. (34), but here for  $q = \omega$ . The total ground-state angular momentum and energy are denoted by  $J_0$  and  $E_0$ , respectively. The quantity  $\frac{\omega^2}{2M_A}$  in the energy-conserving delta function is the recoil energy of the nucleus with mass  $M_A$ , which can be neglected below pion production.

By calculating the initial and final state wave functions with a given Hamiltonian  $H$ , and then sandwiching a one-body or a two-body transverse current operator between them, one can study the effect of two-nucleon currents on the calculated cross sections. Alternatively, one can explore the low-energy Siegert theorem [122], which consists of replacing the total current operator  $j_\lambda(\mathbf{q})$  by its limit at  $\mathbf{q} \rightarrow 0$ . By using the continuity equation, one can then connect transverse electric multipoles  $EJ$  to the longitudinal Coulomb multipoles  $CJ$ , that are derived from the charge operator  $\rho(\mathbf{q})$ . In this way, the dominant part of the e.m. two-body currents is implicitly included. In the long-wavelength limit, where the first multipole  $J = 1$  prevails and neglecting the  $M1$  transition, Eq. (40) can be rewritten as

$$\sigma_\gamma(\omega) = 4\pi^2\alpha \omega R^{E1}(\omega), \quad (42)$$

with  $R^{E1}(\omega)$  being the dipole response function

$$R^{E1}(\omega) = \frac{1}{2J_0 + 1} \sum_f |\langle \Psi_f | D_z | \Psi_0 \rangle|^2 \delta(E_f - E_0 - \omega). \quad (43)$$

Here,

$$D_z = \sum_i^A (z_i - Z_{cm}) \left( \frac{1 + \tau_i^3}{2} \right) \quad (44)$$

is the dipole operator,  $z_i$  is the  $z$ -coordinate of the  $i$ -th nucleon, while  $Z_{cm}$  denotes the  $z$ -component of the center of mass of the nucleus. The expression in Eq. (42) is known

as cross section in the unretarded dipole approximation and is obtained by using the Siegert theorem. Retardation effects are included when the full Bessel function, entering the general expression of the current multipoles, is considered instead of its expression in the long-wavelength limit of  $qR \ll 1$ , with  $R$  being the average size of the nucleus (see, *e.g.* [23, 225]). It is well known that the unretarded dipole cross section is a very good approximation of the full expression given in Eq. (40) for energies well below the pion production threshold.

In the following, we present the most recent *ab-initio* calculations of photodisintegration cross sections and compare them with the available experimental data. For simplicity, we concentrate on unpolarized cross sections and discuss, in dedicated subsections, a variety of light nuclei ranging from mass number  $A = 2$  and  $A = 16$ . Obviously, polarization observables are extremely important to understand nuclear dynamics. They have already been investigated for some nuclei and we refer to some of these results in our discussion, without, however, going into much details.

**4.1.1. The deuteron** — The photodissociation of the deuteron has been extensively studied for a long time both theoretically and experimentally (see, *e.g.*, Refs. [8, 225]). The deuteron is the simplest nuclear system available in which one can explore the role of two-body physics coming from two-body current operators. A  $\chi$ EFT study along these lines has been presented in Ref. [226], where OPE currents (diagrams (b) and (c) in Figure 3) and TPE currents (diagrams (e–h) in Figure 3) have been included. This calculation is not complete in that contact two-body currents also entering at N3LO (see diagrams (j–o) in Figure 3) have not been included. Nevertheless, it is interesting to discuss the main findings in comparison to experimental data and to calculations based on the conventional approach.

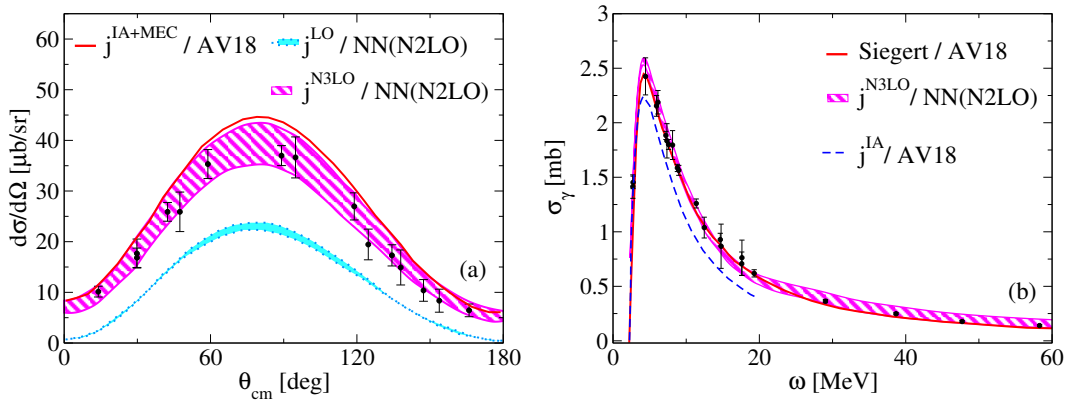


**Figure 22.** (Color online) Panel (a): Deuteron differential unpolarized cross section at photon laboratory energy of  $\omega = 30$  MeV displayed as a function of the proton emission angle.  $\chi$ EFT calculations are from Ref. [226] (with one-body current only in dotted cyan and with one- and two-body currents in the magenta hatched band) in comparison to conventional calculations (red solid curve) and to experimental data by Ying *et al.* from [227]. Panel (b): Deuteron total photoabsorption cross section as a function of the photon energy. Calculations based on Siegert theorem (red solid curve) are from Ref. [228], IA calculations (blue dashed curve) are from Ref. [21], and  $\chi$ EFT calculations with two-body currents (magenta hatched band) are from Ref. [226]. Experimental data as given in Ref. [225] are represented by the black dots.

In panel (a) of Figure 22, the calculated differential cross sections from Ref. [226] are shown. Calculations have been performed by introducing the explicit form of the current operator

in the relevant matrix elements entering Eqs. (40) and (41). It is apparent that predictions with the one-body current only (cyan dotted band) strongly underestimate the data, while, when two-body currents are included (magenta hatched band), an agreement with the data is established. As expected, most of the effect of two-body currents comes from the OPE term. The band is obtained by using five different parameterizations for the chiral potential at N2LO [96, 229], and its thickness can be interpreted as an estimate of the theoretical uncertainty. Such a band is expected to decrease with the addition of the contact two-body currents and when the chiral order of both potential and currents is increased. The  $\chi$ EFT approach also agrees fairly well with the conventional approach (red solid curve), where the AV18 potential was used and MEC were included (see Ref. [226] for details).

In panel (b) of Figure 22, the total photoabsorption cross section is displayed as a function of the photon energy. The  $\chi$ EFT calculation from Ref. [226] explicitly includes the effect of two-body currents from the one- and two-pion exchanges and clearly leads to a nice agreement with data. The conventional calculation with the AV18 potential (red solid curve) from Ref. [228] is instead based on the use of the Siegert theorem, and is related to an  $E1$  response as in Eq. (42) and (43). Thus, the main part of the MEC is included. It is well known from the conventional approach that the IA strongly underestimates the total cross section. To highlight this fact, in Figure 22(b) we report on the conventional calculation by Marcucci *et al.* from Ref. [21], where the IA (blue dashed curve) is used for energies below 20 MeV. In Ref. [21], it was also shown that a perfect agreement between conventional calculations that explicitly include MEC and those obtained with the Siegert theorem is obtained below 20 MeV photon energies. Previous studies, reported in Ref. [225], have shown that retardation effects and higher order multipoles contribute to an enhancement of the cross section of about 10% at  $\omega = 80$  MeV, while further contributions due to exchange currents and relativistic effects cancel each other in the energy range from 5 to 100 MeV.

It is interesting to note that the  $\chi$ EFT and the conventional Siegert calculations are consistent with each other. The main difference in percentage is found in the high energy tail, where, in fact, corrections to the unretarded dipole approximation may start to be relevant. Nevertheless, the Siegert/AV18 curve falls into the error band of the  $\chi$ EFT calculation.

Finally, we would like to mention that polarization observables have been studied in the two-body case, both in the conventional approach (see, *e.g.*, [21, 230]) and in the  $\chi$ EFT approach (see, *e.g.*, [226]), where important effects of exchange currents have been found.

*4.1.2. The three-body nuclei* — In moving from two- to three-body nuclei, the dynamics becomes richer due to the appearance of 3N forces. Because of the present incomplete theoretical underpinning of 3N forces, a possible way to search for effects of 3N forces is to use high precision NN potentials in three-body calculations of hadronic observables and look for differences between theoretical predictions and experimental data. This kind of studies has been performed for bound-state energies of  ${}^3\text{H}$ ,  ${}^3\text{He}$  (and  ${}^4\text{He}$ ) [231, 232], as well as for nucleon-deuteron collisions, see, *e.g.*, Refs. [233, 234]. Complementary information can be accessed by studying photodisintegration processes, involving the interaction between photons and many-body nuclear currents. Thus, e.m. reactions with  $A = 3$  nuclei can be crucial observables to test, refine and possibly even discriminate among different theoretical approaches for Hamiltonians and currents.

The photodisintegration of three-body nuclei has been investigated by a number of groups using different techniques. Calculations using conventional potentials and currents have been performed with the HH method in Refs. [21, 186], with the Faddeev approach in Refs. [235–237] and with the LIT method in Refs. [236, 238, 239]. Details on the different few-body methods can be found in the recent review of Ref. [51]. Regarding the effect

of conventional two-body currents, Faddeev and HH calculations have shown that for the two-body channel at low photon energy MEC enhance the differential photodisintegration cross section by 50% in the peak region. The first study of three-body photodisintegration processes carried out within  $\chi$ EFT is found in Ref. [226], where the two- and three-body photodisintegration of  ${}^3\text{He}$  have been studied with Faddeev-type calculations. In that study, 3N forces were omitted and Coulomb effects were neglected in the scattering states. When looking for effects of one- and two-pion exchange currents in the differential cross section, the situation resembled very much that one of the deuteron presented in Figure 22. Two features are worth stressing: (i) the addition of two-body currents strongly enhances the strength in the differential cross section, and (ii) the  $\chi$ EFT approach agrees rather well with the conventional calculations with the AV18 potential and corresponding MEC

We now turn our attention to study the sensitivity of the calculated cross sections to different Hamiltonians used to generate the nuclear wave functions. Specifically, we are interested to see what happens when 3N forces are switched on and off. In Ref. [237], it has been shown that cross sections calculated with explicit two-body currents or with the Siegert theorem nicely agree with each other at low-energies. Thus, in a Siegert calculation of the photodisintegration cross section the only input that can be changed is the nuclear Hamiltonian. In Figure 23, we show results from Ref. [236] obtained with the LIT method using the AV18 (blue dashed curve) and AV18+UIX (red solid curve) potentials for  ${}^3\text{H}$  (a) and  ${}^3\text{He}$  (b), in comparison with available experimental data. Similar results were obtained with slightly different three-body Hamiltonians in Ref. [238]. We emphasize that, due to the Siegert theorem, these results also include 3N currents effects in the electric dipole response, that otherwise should have been included explicitly as it has been done in Ref. [21]. In Figure 23(a), we also show the calculation for  ${}^3\text{H}$  performed within the Faddeev approach [236] (red dots) using the same interaction, *i.e.*, the AV18+UIX, and dipole transition operator. One can appreciate that the agreement between the two different methods is very good. The small difference between the two approaches can be interpreted as the numerical error of a theoretical calculation with this interaction. The latter is smaller than the theoretical deviation obtained when using a Hamiltonian without 3N forces and smaller than the experimental error bar indicated by the gray band.

In Refs. [236, 238], it has been found that the addition of the 3N forces reduces the strength of the calculated cross sections by roughly 10% at the peak region, leading to a better agreement with experimental data, as can be especially appreciated in the  ${}^3\text{H}$  case illustrated in Figure 23(a). This behavior observed in presence of the 3N forces is related to the additional binding they provide in the three-body system, which, in a naïve picture, reduces the probability to disintegrate the nucleus. In fact, for the triton, the binding energy is  $B.E. = 7.60(8.47)$  MeV with the AV18(AV18+UIX) potential. In Ref. [238], the isospin  $T = 3/2$  channel (which is exclusively a three-body break-up channel) was found to be more sensitive to 3N forces than the  $T = 1/2$ , their main effect being an enhancement of the tail of the cross section, amounting to 15% at 70 MeV.

Other non-local two-body Hamiltonians have been used to calculate the total cross section in the unretarded dipole approximation. Among these are the the potential obtained within the unitary correlation operator method (UCOM) [242] used in Ref. [239], and the  $J$ -matrix inverse scattering potential (JISP) [243] used in Ref. [244]. It is interesting to see how these potentials compare to other interactions and to experimental data, as they may induce strong exchange currents due to their non-locality. In case of the UCOM potential, the results lie between the AV18 and AV18+UIX curve, while for the JISP potential, the cross section has a higher tail with respect to the AV18+UIX curve, indicating that strong exchange currents



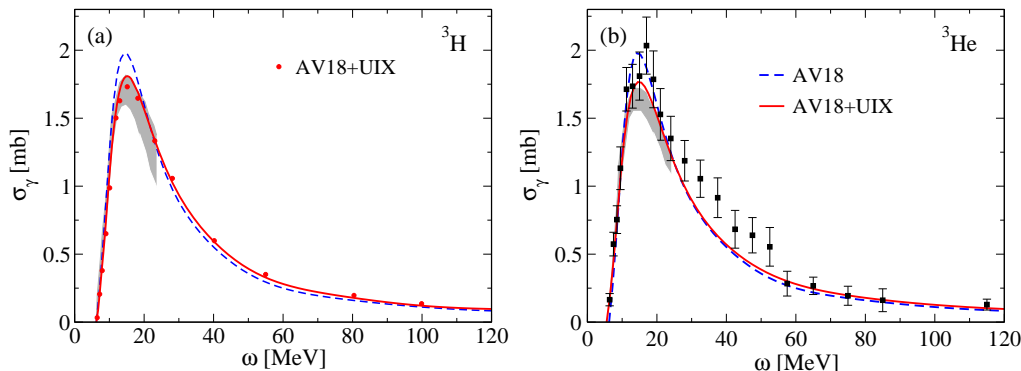


**Figure 23.** (Color online) Total photodisintegration cross sections from Ref. [236] for  ${}^3\text{H}$ , panel (a), and  ${}^3\text{He}$ , panel (b), as a function of the photon energy in comparison to the experimental data by Faul *et al.* from Ref. [240] (gray band), and by Fetisov *et al.* from Ref. [241] (squares). Calculations obtained with the LIT method (blue dashed curve with the AV18 and red solid curve with the AV18+UIX potential) compared to the results obtained in the Faddeev approach (red dots with the AV18+UIX potential).

are induced with this potential. Due to the large experimental error bar, it is not quite possible to discard such a potential model based solely on the three-body data.

The contribution of two- and three-body break-up channels to the total cross section has also been studied with the Faddeev approach. The three-body break-up cross section becomes larger than the two-body break-up one at 14 MeV and at higher energies it is the dominant channel. Similarly to the inclusive case, in the exclusive two-body channel, *e.g.*,  $\gamma+{}^3\text{H} \rightarrow d+n$ , the addition of 3N forces leads to a lower peak in the cross section and to a better agreement with experiment. However, the data are quite scattered, making it hard to draw final conclusions on different potentials. The photodisintegration of  ${}^3\text{He}$  into three-nucleons was extensively studied in Ref. [235] with conventional Hamiltonians and currents. Specifically, effects due to 3N forces have been sought for by comparing results with and without 3N forces in various kinematic regions. Very large effects of 3N forces amounting up to a 85% were found, a finding that could help planning for future experiments.

We recall that studies on polarization observables on  ${}^3\text{He}$  have been performed, *e.g.*, in Refs. [21, 186, 245], where a sensitivity to both 3N forces and to the detail of the many-body contributions to the nuclear current operator has been observed. In Ref. [226], polarization observables have been studied within the  $\chi\text{EFT}$  approach and very strong effects of exchange currents have been found in the photon analyzing power, leading even to a completely different shape of the angle-dependent curves when going from the simple IA picture to the one that includes two-body e.m. currents. Furthermore, recent studies on neutral pion production off three-body nuclei carried out in  $\chi\text{EFT}$  have also pointed out to large effects of two-body currents [246].

**4.1.3. The  ${}^4\text{He}$  nucleus** — Particular attention has been recently devoted to the study of the  ${}^4\text{He}$  photodisintegration reaction. This process is particularly interesting, from both a theoretical and an experimental point of view, due to a number of reasons. First, with a binding energy per nucleon of about 8 MeV/A,  ${}^4\text{He}$  can be considered the link between the very light nuclei,  ${}^2\text{H}$ ,  ${}^3\text{H}$ , and  ${}^3\text{He}$ , and heavier systems. Second, because NN and 3N forces

are typically calibrated on two- and three-body nuclei,  $^4\text{He}$  is the most natural testing ground for microscopic nuclear forces. Third, due to its larger density with respect to the lighter nuclei, intermediate and short range physics effects, such as those generated by 3N forces, are expected to be more important. In fact, conventional 3N forces contribute 17% of additional binding energy, leading to 24.27 (28.42) MeV with the AV18 (AV18+UIX) potential. This correction due to 3N forces is much larger than the 10% effect found in  $^3\text{H}$ . Finally, because of gauge invariance, nuclear forces also manifest themselves as exchange currents which are very important in photonuclear reactions, making the photodisintegration of  $^4\text{He}$  particularly interesting to study further effects of 3N forces.

The theoretical computation of such process is complicated by the difficulty of calculating the four-body continuum states. For the ground state of  $^4\text{He}$ , several few-body methods can be applied to precisely calculate its properties using realistic forces (as it has been shown in the famous benchmark study reported in Ref. [247]). The same is not true for break-up observables where many channels in the final state are open. However, one can avoid the complications of the explicit calculations of continuum final states by using a bound-state formulation of the continuum problem. This is what is achieved for, example, with the LIT method, and with the complex scaling method, see, *e.g.*, the review articles of Ref. [51] and [248].

From the experimental point of view, most of the efforts have been devoted to the measurements of exclusive channels, like  $^4\text{He}(\gamma, n)^3\text{He}$  and  $^4\text{He}(\gamma, p)^3\text{H}$ . For the  $^4\text{He}(\gamma, p)^3\text{H}$  reaction, the available data are scattered in the energy range between 20 and 35 MeV. The current experimental status is nicely summarized in Ref. [249], where data from both photon beams and as well as those deduced from the time reversed radiative-capture reaction using the principle of detailed balance are used. For the  $^4\text{He}(\gamma, n)^3\text{He}$  reaction, the experimental situation is unsettled (see Ref. [250] for a summary on this topic).

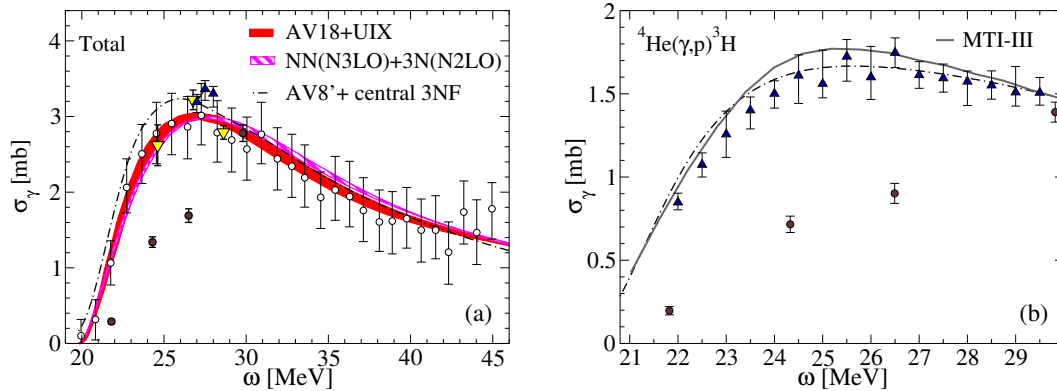


**Figure 24.** (Color online)  $^4\text{He}$  photoabsorption cross section based on the Siegert theorem for the total process, panel (a), and the exclusive channel  $^4\text{He}(\gamma, p)^3\text{H}$ , panel (b). Theory is compared to experimental data: empty circles by Nakayama *et al.* from Ref. [251], yellow triangles-down by Nilsson *et al.* from Ref. [252], blue triangles-up by Raut *et al.* from Ref. [249, 250] and brown circles by Shima *et al.* from Ref. [253] (see text for more details).

In Figure 24, we present *ab-initio* theoretical results in comparison with the most recent experimental data (from 2005 or later). On the left, we show the total cross section and on the right we present the  $^4\text{He}(\gamma, p)^3\text{H}$  exclusive reaction. For the total cross section, the first realistic calculations have been performed in Ref. [174] with the AV18+UIX potential

(red solid band), using the LIT method in conjunction with the EIHH expansion. The  $\chi$ EFT approach has been utilized, instead, in Ref. [254] (magenta hatched band), where the NN force was taken at N3LO ( $\nu = 4$ ) and the 3N force at N2LO ( $\nu = 3$ ) with a fit of the LECs from Ref. [173]. There, the LIT method has been used in combination with the NCSM [255]. For these realistic three-body Hamiltonians the results are shown with a band, corresponding to the theoretical uncertainty of the used computational method. An other recent calculation has been performed by Horiuchi *et al.* [256] (dash dotted curve) using the complex scaling method with the two-body AV8' potential [65] (a simplified version of the AV18 NN potential) supplemented by a simple central 3N force from Ref. [213]. These three theoretical calculations are shown in Figure 24(a). They are all based on the use of the Siegert theorem, *albeit* with different Hamiltonians, which all reproduce the experimental binding energy of  ${}^4\text{He}$  within one percent. Because they form a kind of theoretical band, with a variation of the order of 10% at the peak, we can be quite confident in saying that there is a solid understanding of nuclear dynamics in this regime. The large differences at threshold are due to the inaccuracy of the complex scaling method (see Ref. [256]) and should not to be considered as an effect of the potential.

When we compare against recent experimental data, the most striking disagreement between theory and experiments, amounting up to a factor of 2, is with the data from Shima *et al.* from Ref. [253]. They have been obtained with a quasi-monoenergetic photon beam and a time projection chamber, where a simultaneous measurement of both the  ${}^4\text{He}(\gamma, n){}^3\text{He}$  and  ${}^4\text{He}(\gamma, p){}^3\text{H}$  reactions has been performed. The data in the energy range below 30 MeV, where the large disagreement exist, have been remeasured by the same group, confirming their findings [257]. The latter are, however, in disagreement with previous data from Nilsson *et al.* on the neutron channel [252] (for the total cross section we show them below the three-body disintegration threshold, where  $\sigma_\gamma \simeq 2\sigma(\gamma, n)$ ) and with data from Nakayama *et al.* [251], measured via the  ${}^4\text{He}({}^7\text{Li}, {}^7\text{Be})$  reaction. To clarify the situation, an experiment has been carried out at the High Intensity Gamma-Ray source [249, 250]. Both the exclusive two-body channels have been measured (in Figure 24(a) we sum the two channels and show just the points in the energy range below the three-body break-up). This last experiment has confirmed that the peak of the cross section is at around 25-26 MeV, in nice agreement with the theory and with the data from Nilsson *et al.* and Nakayama *et al.*, and in strong disagreement with the data from Shima *et al.* Discarding this specific set of data, it can be said that there is nice agreement between theory and experiment.

For the exclusive  ${}^4\text{He}(\gamma, p){}^3\text{H}$ , in Figure 24(b) we show the calculations with the MTI-III potential from Ref. [219] (grey solid curve), performed with the LIT method, and those with the AV8' with a central 3N force from Ref. [256] (dash-dotted curve), performed with the microscopic R-matrix method. We compare them to the exclusive measurements from Tornow *et al.* [250] and from Shima *et al.* [253]. Also in this case, the theory supports a higher cross section in disagreement with the data from Shima *et al.* One can also see that the calculation with the more realistic AV8' potential and the central 3N force is actually in better agreement with the data from Tornow *et al.* Efforts are being directed towards a calculation of this cross section based on the AV18+UIX with the LIT method [258].

Finally, we would like to comment on the role of 3N forces. In Ref. [174], they were found to lead to a 6% decrease of the cross section peak, but also to a large enhancement, up to 35% , of the strength at energies above 50 MeV. Such 3N force dependence cannot be simply interpreted as a binding effect. The only inclusive experimental data that cover a wide range in energy are from Arkatov *et al.* [259]. When the UIX potential is added to the AV18 two-body force, the agreement with data is actually improved in the energy range from  $\omega = 50$  to 80 MeV. Beyond that, and up to pion threshold, the AV18 potential does provide

the best description of the data. Finally, we remind that other non-local two-body potentials, like the JISP, actually do lead to a cross section which is higher and not in agreement with the experimental data, as pointed out in Ref. [244]. This is presumably due to large exchange currents induced by the non-locality in the potential.

*4.1.4. The  $A = 6$  and 7 nuclei* — We now consider slightly heavier nuclei. Traditionally, nuclei with a number of nucleons between 4 and about 12 are considered as a bridge between the few- and the many-body systems. Furthermore, with increasing mass numbers, nuclear spectra become more complex and new interesting phenomena arise. For example, within the isobar nuclei with mass number  $A = 6$ , we have a two neutron-halo nucleus, *i.e.*,  ${}^6\text{He}$  [260]. This happens also to be the lightest halo nucleus in the nuclear chart, and, as such, has received quite a bit of attention both from the theoretical and experimental point of view (see, *e.g.*, Ref. [175]).  ${}^6\text{He}$  is a very short lived nucleus (half life of  $t_{1/2} = 807$  ms) that can be compared to the stable  ${}^6\text{Li}$  nucleus. An interesting question to ask is: does the interaction of a real photon with these two isobar analog nuclei lead to different structures in the photodisintegration cross section? Obviously, to answer this question one has to face two challenges, one theoretical and one experimental: (i) the exact calculation of six-body final state wave functions with various open channels is currently out of reach, and (ii) experiments with real photons cannot be done on unstable nuclei, so alternative techniques need to be looked for.

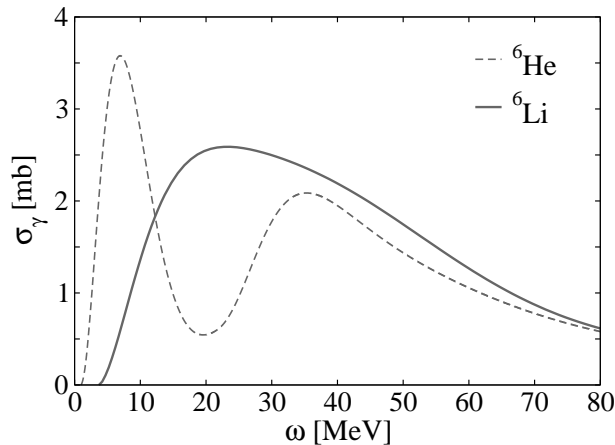


**Figure 25.** Theoretical photoabsorption cross section of  ${}^6\text{He}$  and  ${}^6\text{Li}$  from Ref. [261] calculated with the  $\text{AV4}'$  potential using the Siegert theorem.

The theoretical problem has been circumvented by using the LIT method. The application of this method in conjunction with the EIHH expansion has allowed to study the photodisintegration of the six-body nuclei in Refs. [261, 262]. Simple semi-realistic interactions have been used, that just fit the  $S$ -wave or (partially) the  $P$ -wave phase-shifts in the NN collisions. Even though they do miss some of the complexity of realistic potentials, such as the tensor and spin-orbit force, they decently reproduce (within 10%) the photodisintegration of lighter nuclei, as discussed earlier. The studies on the six-body nuclei have shown that the halo structure of the rare  ${}^6\text{He}$  isotope leads to considerable differences

from the stable  ${}^6\text{Li}$  nucleus in photodisintegration. As shown in Figure 25, for  ${}^6\text{He}$  the dipole cross section exhibits two well separated peaks, while a single resonant shape is observed for  ${}^6\text{Li}$ . The first peak corresponds to the break-up of the neutron halo, while the second peak corresponds to the break-up of the  $\alpha$ -particle. These results do not depend on the employed NN interaction: three different semi-realistic interactions have been used, and they have been found to lead to very similar structures. The curves in Figure 25 have been obtained with the AV4' potential [263], which is a truncated version of the AV18 potential, that leads to a reasonable description (10-15% from experiment) of the binding energy of these nuclei and includes some  $P$ -wave components, which are found to be important in  $p$ -shell nuclei [261].

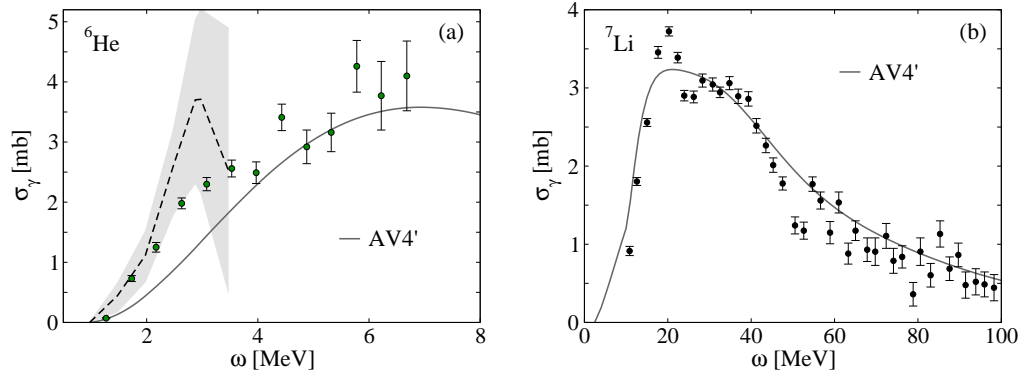


**Figure 26.** (Color online)  ${}^6\text{He}$  and  ${}^7\text{Li}$  total photoabsorption cross sections calculated with the AV4' potential from Refs. [261] in comparison to experimental data: for  ${}^6\text{He}$ , green circles denote data by Aumann *et al.* [264], while the gray band denotes data by Wang *et al.* [265]; for  ${}^7\text{Li}$ , dark circles represent data by Ahrens *et al.* [266].

Photonuclear experiments on unstable system cannot be done. However, the low-energy photodisintegration cross section, which is related to the dipole response function via the Siegert theorem as in Eq. (42), can be inferred from Coulomb excitation experiments, see, *e.g.*, the review [5]. In this case, a beam of rare isotopes is used as projectile in collisions with heavier targets. In specific circumstances, the Coulomb interaction between the projectile and the target either dominates or can be separated from the nuclear part. From the Coulomb interaction one can extract the  $E1$  strength and then reconstruct the photoabsorption cross section. For  ${}^6\text{He}$ , this kind of experiments has been done at GSI by Aumann *et al.* [264] with high projectile energy (240 MeV/nucleon) and at NCSL by Wang *et al.* [265] with lower projectile energy (25.2 MeV/nucleon). In Figure 26(a), we show these experimental results in comparison to the theoretical calculations from Ref. [261]. As one can see, the theory decently describes the data for  $\omega > 5$  MeV, but underpredicts the strength very close to threshold. The spin-orbit force, which is missing in the AV4' potential, could possibly enhance the strength in this energy region.

For  ${}^6\text{Li}$ , which is a stable isotope, several experiments on photonuclear reactions exist, however none of them corresponds to an inclusive measurement. Because summing all the different channels coming from different experiments is delicate and because the experimental situation for the exclusive processes is not settled, we prefer, instead, to show the comparison of theory with experiment for  ${}^7\text{Li}$ . Calculations on  $A = 7$  nuclei have been performed in Refs. [267] using the LIT with an EIHH expansion and the AV4' potential. Inclusive data

for  ${}^7\text{Li}$  have been measured by Ahrens *et al.* [266] and are shown in Figure 26(b). One can observe that, despite the simple potential used, the theoretical curve nicely describes the gross feature of the experimental data, *i.e.*, a steep rise, a broad maximum and a slow fall-off.  ${}^7\text{Li}$ , as  ${}^6\text{Li}$ , is a stable nucleus and show only one large bump, very differently from the two separated peaks found in  ${}^6\text{He}$  by theory. These theoretical calculations have stimulated new experimental efforts devoted to measure, *e.g.*, the photoabsorption of  ${}^{6,7}\text{Li}$  at the High Intensity Gamma-Ray Source [268] and at MAX-lab in Lund [269, 270]. The predicted presence of the second peak in the  ${}^6\text{He}$  photodisintegration cross section is still waiting for an experimental observation.

*4.1.5. Towards medium-mass nuclei* — First principle calculations of photonuclear reactions, where one starts from realistic NN forces that reproduce (some) NN phase-shifts, have been available only for the light systems, in the recent past. For the medium-mass nuclei, instead, several studies exist in the literature, where the photodisintegration is investigated using Skyrme-functionals (see, *e.g.*, Refs. [271, 272]), which are typically calibrated on finite nuclei. Alternative (macroscopic) approaches, like, *e.g.*, Halo EFT have also been recently investigated, see Ref. [273]. The reason for the lack of *ab-initio* calculations in the medium-mass regime is that one has to account for the very strong correlations induced by realistic interactions in both the ground state and in the final states in the continuum. The difficulty of theoretically describing the continuum states can be circumvented with the LIT method which reduces the problem to a bound-state-like equation. As shown above, the LIT method has been used together with HH expansions and with the NCSM. Both these methods do not lend themselves to a straightforward application to the medium-mass nuclei. In a recent paper [274], it has been shown that the LIT method can be used in conjunction to CC theory, a many-body approach well suited for the medium-mass and heavy nuclei [73]. The combination of the LIT with CC theory [275] has allowed to extend the previous mass limits of the theory and address the inclusive photodisintegration in  ${}^{16}\text{O}$ . The method has been first benchmarked with the exact EIHH on  ${}^4\text{He}$  using the same nuclear Hamiltonian. Despite the approximations introduced in the CC calculations, a very nice agreement has been found between the two-methods for  ${}^4\text{He}$ .

In Figure 27, we present the theoretical results for the dipole response function of  ${}^{16}\text{O}$  in comparison to the available data from Ahrens *et al.* [266]. The experimental cross section is transformed into a dipole response function using Eq. (42). For the starting Hamiltonian, the  $\chi\text{EFT}$  approach has been taken, where the NN interaction at N3LO ( $\nu = 4$ ) from Entem and Machleidt [98] (inclusive of Coulomb force) has been used, but 3N forces have been omitted. The band of the cyan curve is obtained by inverting the LIT with a slightly different regularization procedure, see, *e.g.*, Refs. [206, 274] for more details. It is apparent that the experimental location of the peak is correctly reproduced by the calculation. Also the total experimental dipole strength is reproduced, while the width of the theoretical resonance is broader than the experimental one. The investigation of the impact of the neglected 3N forces and higher order correlations on the photonuclear cross section of medium-mass nuclei is currently underway. This first case study paves the way for many future investigations of continuum responses in medium-mass nuclei for both stable and unstable isotopes, which will be accessible using the LIT method in conjunction with CC theory.

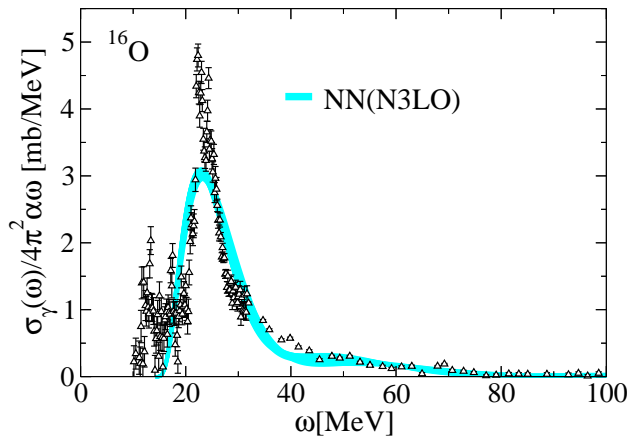


**Figure 27.** (Color online) Comparison of the  $^{16}\text{O}$  dipole response function calculated in coupled-cluster theory from Ref. [274] against experimental data by Ahrens *et al.* from Ref. [266].

#### 4.2. Radiative capture reactions

Radiative capture processes are the time inverse of nuclear photoabsorption reactions at few MeVs (or even keVs) above threshold, where only one channel is energetically open. The two processes are connected to each other via the detailed balance principle, see *e.g.*, Ref. [276]. Thus, conclusions similar to those obtained from studies on photodisintegration processes are drawn from studies on radiative capture reactions. Besides the important role played in nuclear structure studies, results from *ab-initio* calculations of low-energy radiative captures involving light nuclei significantly affect important areas of astrophysics (see, *e.g.*, the review articles of Refs. [277, 278]).

For reactions involving charged objects, one typically introduces the astrophysical  $S$ -factor, which is related to the radiative capture cross section,  $\sigma_c(E)$ , via

$$S(E) = \sigma_c(E)E \exp[2\pi\eta(E)], \quad (45)$$

where  $E$  is the center of mass energy of the reactants and  $\eta(E)$  is the Sommerfeld parameter, which takes into account the probability of penetrating through the Coulomb barrier.  $S(E)$  is a much more slowly varying function of  $E$  compared to  $\sigma_c(E)$ . The latter falls exponentially due to the Coulomb repulsion. The  $S$ -factors at low (virtually zero) energies is particularly interesting for astrophysical studies, as at these energies nucleosynthesis reactions take place in the stars. For example,  $S$ -factors of radiative capture reactions are used as inputs parameters of (i) theoretical calculations aimed at determining the primordial abundances of light elements [279], and (ii) the standard solar model, relevant for studies on stellar structure and evolution [277, 278]. An accurate knowledge of the pertinent cross sections is then a crucial prerequisite for the above mentioned astrophysical studies. The experimental evaluation of such cross sections is often problematic, leading to scarce and/or inaccurate data. Due to the level of reliability reached by *ab-initio* calculations, cross sections derived

from them are used as inputs, instead. This strategy has been recently implemented in, *e.g.*, Refs. [280, 281], where the calculated  ${}^2\text{H}$  and  ${}^7\text{Li}$  yields of big-bang nucleosynthesis rely on the theoretical estimates of the  $p(n,\gamma)d$  and  $d(p,\gamma){}^3\text{He}$  cross sections, obtained within pionless EFT [282], and the conventional approach [21, 186], respectively.

After the review by Carlson and Schiavilla [23], a number of *ab-initio* calculations of e.m. reactions in light nuclei relevant to astrophysics has appeared in the literature. Some of these calculations have been already reviewed by Marcucci *et al.* in Ref. [283]. Below, we report on a few of the most recent highlights, with emphasis on advances brought in by the use of nuclear  $\chi$ EFTs and by the introduction of novel computational methods.

*4.2.1. Systems with  $A \leq 4$*  – Low-energy proton and neutron captures on few-nucleon systems are particularly interesting from the standpoint of nuclear structure studies. Indeed, MEC effects were at first quantified as a correction to the calculated thermal neutron radiative capture on proton cross section, and were found to provide the 10% contribution needed to resolve the discrepancy with the experimental datum [13].

Thermal neutron radiative captures are induced by the  $M1$  transition operator that connects the initial two-cluster state in relative S-wave and the final bound state. The experimental values of the cross sections for thermal neutron captures on  ${}^1\text{H}$ ,  $d$ , and  ${}^3\text{He}$  in mb are:  $(332.6 \pm 0.7)$  [284],  $(0.508 \pm 0.015)$  [285], and  $(0.055 \pm 0.003)$  [286, 287], respectively. The drop in the values in going from  $A = 2$  to  $A = 3, 4$  is due to the so called ‘pseudo-orthogonality’ between the initial and final wave functions in the reactions involving  $A = 3, 4$  nuclei. In fact, the  ${}^3\text{H}$  and  ${}^4\text{He}$  wave functions,  $\Psi_3$  and  $\Psi_4$  respectively, are approximately eigenfunctions of the LO (or IA) one-body  $M1$  operator  $\mu(\text{IA})$  (see Eq. (26)), namely  $\mu(\text{IA})_z \Psi_3 \simeq \mu_p \Psi_3$  and  $\mu(\text{IA})_z \Psi_4 \simeq 0$ , where  $\mu_p = 2.793$  n.m. is the proton magnetic moment—the experimental value of the  ${}^3\text{H}$  magnetic moment is 2.979 n.m, while  ${}^4\text{He}$  has no magnetic moment. If small components in wave functions, generated by tensor components in the nuclear potentials, are neglected, then the matrix elements  $\langle \Psi_3 | \mu(\text{IA})_z | \Psi_{1+2} \rangle$  and  $\langle \Psi_4 | \mu(\text{IA})_z | \Psi_{1+3} \rangle$  vanish due to orthogonality between the initial and final states. In the case of the deuteron, instead, the  $M1$  operator can connect the large deuteron S-wave component to the  $T=1$   ${}^1\text{S}_0$   $np$  scattering state.

Due to this suppression at the IA level, radiative capture cross sections are particularly sensitive both to small components in the wave functions (and, therefore, indirectly to the nuclear Hamiltonians utilized to generate them), and to many-body components in the e.m. current operators. Early calculations of the  $nd$  and  $n{}^3\text{He}$  radiative capture cross sections in IA predicted only  $\sim 50\%$  [288] and  $\sim 10\%$  [89], respectively, of the corresponding experimental values. Studies that account for corrections due to conventional MEC reported a calculated value of the  $nd$  radiative capture within 15% of the experimental value [87], while the calculated value of the  $n{}^3\text{He}$  cross section was found to be  $86 \mu\text{b}$  [289], to be compared to the experimental value of  $55 \pm 3 \mu\text{b}$ .

In recent years, methods for solving the  $A = 3$  and 4 Schrödinger equations have been refined [290–292], and highly accurate nuclear wave functions for these systems are now available. Theoretical calculations of the  $nd$  and  $n{}^3\text{He}$  radiative capture cross sections [293] based on nuclear wave functions obtained from the HH techniques [58] are shown in Figure 28. The bands represent results from hybrid and chiral calculations that use the  $\chi$ EFT currents developed in Refs. [37, 46]. The thickness of the bands represents the spread in the calculated values corresponding to the two considered nuclear Hamiltonians, namely the AV18+UIX and the NN(N3LO)+3N(N2LO), where the two- and three-body chiral interactions are from Refs. [98] and [100], respectively. The sensitivity to the regularization cutoff  $\Lambda = 500\text{--}700$  MeV is shown on the  $x$ -axis. The procedure implemented to fix the



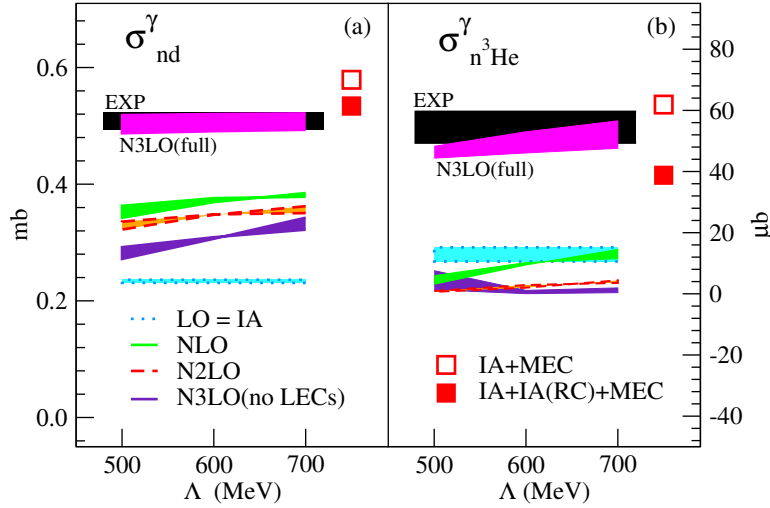


**Figure 28.** (Color online) Results for  $\sigma_{nd}$  (a),  $\sigma_{n^3\text{He}}$  (b) from Ref. [293], obtained by including cumulatively the LO, NLO, N2LO, N3LO(no LECs), and N3LO(full) contributions to the e.m. current operator from  $\chi\text{EFT}$ . Also shown are predictions obtained in the conventional approach (squares labeled IA+MEC and IA+IA(RC)+MEC, which includes relativistic corrections to the IA operator). The experimental data (black) are from Ref. [285] for  $nd$  and Ref. [286] for  $n^3\text{He}$ . The band height represents the experimental error bar.

LECs entering the e.m. currents is different from that one utilized for the calculations of Refs. [48, 123] that have been discussed in Secs. 3.2 and 3.3.2, respectively. In particular, here, the  $\Delta$ -resonant saturation argument has been exploited to infer the ratio between the isovector LECs entering the tree-level current at N3LO ( $\nu = 1$ )—see panel (k) of Figure 3. Therefore, one is left with four e.m. LECs. Namely, an isoscalar and an isovector LEC associated with the tree-level current at N3LO, see panel (k) of Figure 3, plus an isoscalar and an isovector LEC associated with a contact-like current at N3LO, see panel (j) of Figure 3. These four LECs have been fixed so as to reproduce the deuteron magnetic moment, the isoscalar and isovector combinations of the trinucleon magnetic moments, and the  $np \rightarrow d\gamma$  cross section at thermal neutron energy [293]. In addition, LECs of minimal nature entering the N3LO contact currents have been taken from a NLO ( $\nu = 2$ )  $\chi\text{EFT}$  potential [46] rather than from the N3LO ( $\nu = 4$ ) [98]  $\chi\text{EFT}$  potential.

In Figure 28, results obtained with the complete N3LO e.m. operator are shown by the magenta (light) band labeled N3LO(full), and are in very satisfactory agreement with data (black band). Their sensitivity to the cutoff is negligible ( $\sim 10\%$ ) for the  $nd$  ( $n^3\text{He}$ ) capture. As discussed above, these processes are strongly suppressed at IA or LO ( $\nu = -2$ ): the calculated  $\sigma_{nd}^{\gamma}(\text{LO})$  and  $\sigma_{n^3\text{He}}^{\gamma}(\text{LO})$  are less than half and a factor of five smaller than the measured values, respectively. The IA(RC) correction at N2LO ( $\nu = 0$ ), corresponding to the relativistic correction to the LO e.m. current illustrated in panel (d) of Figure 3, along with the correction labeled N3LO(no-LECs), corresponding to the one-loop and minimal contact currents at N3LO, is found to have opposite sign with respect to the LO contribution. The N3LO(full) contributions, corresponding to the tree-level and non-minimal contact currents at N3LO—see panels (j) and (k) of Figure 3—are large and crucially important for bringing theory into agreement with experiment. Results obtained within the conventional model are also shown in Figure 28. These calculations use the MEC of Ref. [21] that have been

constructed from the AV18+UIX nuclear Hamiltonian, along with the  $A = 3, 4$  improved nuclear wave functions [292]. In particular, empty red squares represent calculations obtained with the non-relativistic IA operator plus conventional MEC corrections. The full red squares add to the empty ones the IA(RC) contribution (or, the N2LO current contribution illustrated in panel (d) of Figure 3). These relativistic corrections have been neglected in previous conventional calculations [21, 87, 89, 288, 289], however, they are found to be significant and, at least in the case of the  $nd$  capture, they bring the prediction of the conventional approach within 4% of the experimental data, as opposed to the 15% estimate from previous studies [87]. Despite this satisfactory result, the description of the  $n^3\text{He}$  remains problematic. We note that hybrid studies based on the  $\chi\text{EFT}$  currents by Park *et al.* [45] have reported values for the  $nd$  and  $n^3\text{He}$  capture cross sections about 6% and 15% smaller than measured, with a cutoff sensitivity of about 15% [129, 130, 294].

Proton capture reactions on neutron or few-body nuclei have been calculated in the past with conventional potentials and currents by Viviani *et al.* [186], by Golak *et al.* [237], and by Marcucci *et al.* [21]. At energies of the order of a few MeV and up, where this process is dominated by an  $E1$  transition, conclusions similar to those obtained from studies on photodisintegration reactions are drawn. In particular, the one-body current alone does not suffice to describe the data, however, when MEC contributions are included, explicitly or implicitly via Siegert theorem, an improved description of the data is obtained. At the low energies relevant for astrophysics, the capture process is instead dominated by the  $M1$  multipole. Because there is no Siegert theorem for magnetic transitions, MEC have to be included explicitly. This has been accomplished in Ref. [21], where MEC contributions have been found to be large and necessary for a satisfactory description of the LUNA data for the  $^2\text{H}(p, \gamma)^3\text{He}$  reaction.

The  $d(d, \gamma)^4\text{He}$  reaction has been recently investigated with *ab-initio* methods by Arai *et al.* [295]. This radiative capture can impact studies on the abundances of primordial elements. This process occurs predominantly via an  $E2$  transition at low-energy. In Ref. [295], calculations with a realistic potential and with simple semirealistic central forces, have been compared, and it has been found that the  $S$ -factor for the  $d(d, \gamma)^4\text{He}$  reaction is very sensitive to the tensor forces.

4.2.2. *Systems with  $A > 4$*  – Many of the relevant nuclear reactions in primordial nucleosynthesis and in solar neutrino production involve light nuclei with mass number  $A > 4$  [277, 278]. The first steps towards *ab-initio* calculations of a few key reactions have been taken using Quantum Monte Carlo methods. For example, the  $\alpha$  capture reactions  $^2\text{H}(\alpha, \gamma)^6\text{Li}$ ,  $^3\text{H}(\alpha, \gamma)^7\text{Li}$ , and  $^3\text{He}(\alpha, \gamma)^7\text{Be}$  have been evaluated in Refs. [296, 297] using VMC wave functions for the initial clusters and the final nucleus. However, a phenomenological relative wave function between the two initial clusters was used. Similarly, a first attempt to calculate the  $^7\text{Be}(p, \gamma)^8\text{B}$  reaction was proposed by Navratil *et al.* [298] using the interior overlap functions obtained from NCSM to constrain the tail of a phenomenological Wood-Saxton potential.

A full *ab-initio* calculation requires the use of the same Hamiltonian for both the initial continuum state and the bound final state. This has been only recently achieved for nuclei with  $A > 5$ . Below, we highlight two examples.

The  $^7\text{Be}(p, \gamma)^8\text{B}$   $S$ -factor is an important input in modeling the neutrino flux coming from our Sun [278]. An *ab-initio* calculation of this process has been performed by Navratil *et al.* [299] using the NCSM with the resonating group method [300, 301], which allows to describe continuum states. The used starting interaction is a  $\chi\text{EFT}$  two-body potential at

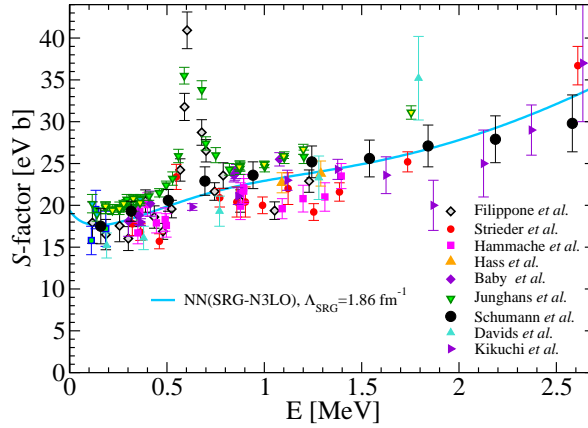


**Figure 29.** (Color online)  ${}^7\text{Be}(p, \gamma){}^8\text{B}$   $S$ -factor: calculation by Navratil *et al.* [299] in comparison to the available experimental data shown as in Ref. [299].

N3LO ( $\nu = 4$ ) [98], which has then been softened by a Similarity Renormalization Group (SRG) transformation [302]. The latter is characterized by an evolution parameter,  $\Lambda_{\text{SRG}}$ , which has been chosen by tuning the calculated  ${}^8\text{B}$  separation energy close to the experimental value. In fact, the low-energy behavior of the  $S$ -factor is very sensitive to the threshold energy.

This process has been investigated using different experimental techniques, including direct measurements with proton beams on  ${}^7\text{Be}$  targets and indirect Coulomb excitations with  ${}^8\text{B}$  beams hitting on a heavy target and breaking into proton and  ${}^7\text{Be}$ . Data are shown in Figure 29 for the astrophysical  $S$ -factor. Even though they are a bit scattered, they clearly display a resonant feature due to the  $1^+$  excitation, which however is very narrow and does not affect much the  $S$ -factor at zero energy, where the process is dominated by a dipole transition. The theoretical curve shown in Figure 29 does not include any  $M1$  transitions, thus it does not show the resonant feature. However, it nicely reproduces the shape of the  $E1$  contribution to the  $S$ -factor. Because the dipole operator is protected by the Siegert theorem, the leading part of the MEC is implicitly included. SRG renormalizations of the dipole operator and overall 3N forces have been conjectured to be small, and omitted for the time being [299].

The  ${}^3\text{He}(\alpha, \gamma){}^7\text{Be}$  radiative capture takes place in the solar Hydrogen burning reaction chains. It is important in determining the high energy solar neutrino flux and in understanding the abundance of primordial  ${}^7\text{Li}$ . It has been measured by several groups, but the difficulty of reaching the very low solar energies makes it hard to extract the needed  $S$ -factor at zero energy. This reaction has been recently calculated by Neff [303] within the Fermionic Molecular Dynamics (FMD) [74], which allows to consistently obtain bound and scattering states from a soft effective interaction. The starting potential used in the calculations is the AV18 two-body force, which has been then softened by using the unitary correlation operator method [242, 310]. Here, the evolution parameter,  $\Lambda_{\text{UCOM}}$ , is tuned so as to reproduce the  ${}^3\text{He}+{}^4\text{He}$  threshold in  ${}^7\text{Be}$ . The calculation carried out with a dipole transition operator is shown in Figure 30 in comparison to recent measurements. As one can see, both the energy dependence and the absolute normalization are in good agreement with experiment. The

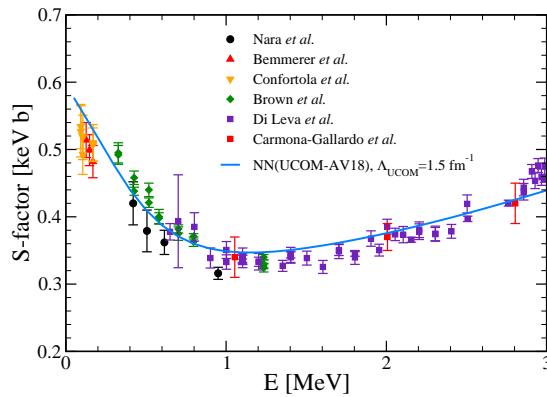


**Figure 30.** (Color online)  ${}^3\text{He}(\alpha, \gamma){}^7\text{Be}$   $S$ -factor: calculation by Neff [303] in comparison to the available recent experimental data from the Weizmann Institute by Nara *et al.* [304], from the LUNA collaboration by Bemmerer *et al.* [305] and Confortola *et al.* [306], from Seattle by Brown *et al.* [307], from Bochum with the recoil separator ERNA by Di Leva *et al.* [308] and from Madrid by Carmona-Gallardo *et al.* [309].

calculation provides a zero-energy  $S$ -factor of 0.592 keVb. Also in this case 3N forces and renormalizations to the dipole operator have been omitted.

The two examples above represent a break-through in the development of calculational techniques that can tackle radiative capture reactions in larger nuclei. However, further studies are needed to assess the theoretical sensitivity of these processes to intermediate and short range physics, entering, *e.g.*, in the form of 3N forces or MEC. In the future, we can expect more investigations along these lines also from the newly developed method to calculate radiative captures from lattice EFT introduced in Ref. [311], and firstly applied to the  $p(n, \gamma)d$  reaction.

Finally, we would like to mention that alternative low-energy effective field theories, such as Halo EFTs, can be applied to the study of radiative capture reactions. This has been recently accomplished, *e.g.*, in Refs. [312–314] for  $A = 8$  systems.

#### 4.3. Electromagnetic transitions in low-lying nuclear states

In this last section we discuss a number of calculated reduced e.m. transition probabilities for  $E2$  and  $M1$  operators in low-lying excited states. The measurement of these observables can involve different nuclear reaction mechanisms. Excited states can be populated, for example, via pure hadronic reactions, or by e.m. induced reactions. To the former class belongs, for example, the  $d+{}^6\text{Li} \rightarrow p+{}^7\text{Li}^*$  reaction, which can be exploited to populate the  ${}^7\text{Li}$  excited states. To the second class belong, for example, radiative capture processes, such as the  $\alpha\alpha$  radiative capture reaction (or *bremstrahlung*) that is used to populate low-lying excited states of  ${}^8\text{Be}$  [315]. Nuclear states' lifetimes and associated reduced transition probabilities are then inferred from the observed photons emitted in the decay process. Transition probabilities for stable targets, *e.g.*,  ${}^7\text{Li}$  and  ${}^9\text{Be}$ , can also be (indirectly) accessed through  $(e, e')$  scattering experiments. Therefore, technically speaking, some of the transitions we discuss do not strictly belong to this part of the review devoted to processes involving real photons.

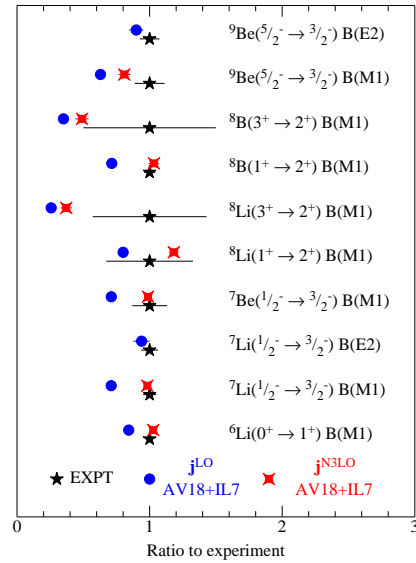


**Figure 31.** (Color online) Transition widths from Ref. [123] normalized to the experimental values [125, 126] for  $A = 7-8$  nuclei. The notation is as in Figure 8.

There are a number of *ab-initio* calculations of e.m. transitions carried out in IA, among which the most notable and recent are, for example, transitions occurring in low-lying states of  $6-7-8\text{Li}$  [316],  $^{10}\text{Be}$  [317, 318],  $^{10}\text{C}$  and  $^{10}\text{B}$  [319],  $^{12}\text{C}$  [106, 320], and  $^{16}\text{O}$  [107]. Because our interest lies in going beyond the IA, which is crucial for magnetic transitions, below we focus the discussion on recent GFMC calculations reported in Ref. [123]. In that work, two-body components in the e.m. current operator have been explicitly accounted for in the  $M1$  transitions induced by the operator defined in Eq. (23). In particular,  $\chi\text{EFT}$  operators developed in Refs. [37, 46–48] have been used in hybrid calculations based on nuclear wave functions obtained from the AV18+IL7 nuclear Hamiltonian. Because the  $M1$  and the  $E2$  operators can connect the same states, it is interesting to compare magnetic dipole and electric quadrupole transitions. The  $E2$  transitions can be easily obtained by using the Siegert theorem, *i.e.*, writing the quadrupole operator of Eq. (22) as

$$Q(\text{IA}) = \sum_i e_{N,i} r_i^2 Y_2(\hat{\mathbf{r}}_i), \quad (46)$$

where  $Y_2$  is the spherical harmonic of rank 2. The decay widths in units of MeV are obtained from the reduced transition probabilities defined in Eqs. (24) and (25), via [119]

$$\Gamma(E2) = 0.241 \left( \frac{\Delta E}{\hbar c} \right)^5 B(E2), \quad (47)$$

$$\Gamma(M1) = 0.890 \left( \frac{\Delta E}{\hbar c} \right)^3 B(M1), \quad (48)$$

where  $\hbar c$  is in units of MeV fm, and  $\Delta E$  is the experimental energy difference between the final and the initial state (in units of MeV), as obtained from the values reported in Refs. [125, 126].

Results from these hybrid calculations in  $A \leq 9$  nuclei are shown in Figure 31. In this figure, we show the ratios to the experimental values of the widths [125, 126], which are represented by the black stars, along with their associated experimental error bars. Predictions in IA are represented by blue dots<sup>†</sup>, while those obtained with the full e.m. current operator are represented by red diamonds. Predictions for the  $A = 6, 7$  nuclei as well as that for the ( $J_i^{\pi_i} = 1^+ \rightarrow J_f^{\pi_f} = 2^+$ ) transition in  ${}^8\text{B}$  are in very good agreement with the experimental data, and corrections from two-body e.m. current operators are essential to reach the agreement with them. For the remaining  $M1$  transitions in  $A = 8$  and  $9$  nuclei, the comparison becomes more difficult, as the experimental errors are too large to allow for conclusive statements on the agreement between theory and experiment. We also note that theoretical description of the two  $E2$  transitions reported in Figure 31 is in good agreement with the experiments. This is presumably due to the fact that two-body effects in the  $E2$  multipole are implicitly accounted for via Siegert theorem. The hybrid GFMC calculational scheme described above has been very recently applied to evaluate about a dozen  $M1$  transitions occurring in low-lying states of  ${}^8\text{Be}$  [321], and corrections from two-body e.m. currents have been found to provide  $\sim 20 - 30\%$  of the total calculated transition matrix elements.

In Ref. [123], a number of predictions (not shown in the figure) for  $E2$  transitions in low-lying excited states along with a prediction for the ( $J_i^{\pi_i} = \frac{1}{2}^- \rightarrow J_f^{\pi_f} = \frac{3}{2}^-$ )  $M1$  transition in  ${}^9\text{Li}$ , obtained with the full  $\chi\text{EFT}$  operator at N3LO ( $\nu = 1$ ), have been provided. The possibility to experimentally verify such predictions on  ${}^9\text{Li}$  is being discussed at TRIUMF [322]. Experimental efforts aimed at both increasing the precision of the existing measured transitions, and at investigating currently unknown transitions would play an important role in assessing the accuracy of the available theoretical nuclear models. Work along these lines has been recently presented in Ref. [315], where the authors have measured the ( $J_i^{\pi_i} = 4^+ \rightarrow J_f^{\pi_f} = 2^+$ )  $E2$  transition in  ${}^8\text{Be}$  via  $\alpha\alpha$  radiative capture reaction, and have reduced the experimental error by more than a factor of three with respect to previous existing measurements. Along with the improved experimental datum, Ref. [315] reported a theoretical GFMC calculation of the  $B(E2)$  associated with that transition. However, the comparison between the experiment and theory was complicated, in this case, by the resonant nature of the  $J^\pi = 2^+$  and  $4^+$  states, which tend to break apart into two  $\alpha$  particles. The effect of the continuum in the resonance has been investigated within a cluster approach (see, e.g., Ref. [323]), and extensions of these studies to the *ab-initio* framework are being presently investigated.

## 5. Summary and outlook

In this review, we provided a summary on the present status of *ab-initio* calculations of e.m. observables in light nuclei. We presented calculations in which nuclei are described in terms of non-relativistic nucleons interacting via many-body potentials and e.m. probes interact with the nucleons via many-body e.m. currents. We discussed reactions occurring at energies below the pion threshold and focused on studies released after the 1998 review article by Carlson and Schiavilla [23]. The years following the publication of that review have witnessed a tremendous progress of computational techniques and resources, as well as the development of novel many-body methods, which have made it possible to extend *ab-initio* studies to nuclei with  $A \sim 16$ . In conjunction with these technological developments, conventional nuclear Hamiltonians and e.m. currents have been improved to reach a high level

<sup>†</sup> Note that the  $E2$  transitions implicitly include the effect of two-body currents via the Siegert theorem, where the charge density is used in IA (which explains the use of the blue color).

of sophistication. Meanwhile, nuclear  $\chi$ EFTs have evolved into an intense and prolific field of research and a description of both nuclear potentials and interactions of nuclei with external e.m. probes is now accessible also from the  $\chi$ EFT perspective.

The study of e.m. reactions presents numerous advantages from the theoretical and experimental points of view. The interaction of light nuclei with e.m. probes is perturbative, and thus it is well described in terms of a single-photon exchange. In addition, nuclear structure effects are present only in the nuclear targets, as opposed to hadronic reactions in which one has to worry about structure effects entering both hadronic probes and hadronic targets. Furthermore, cross sections for e.m. reactions, while being usually smaller than those associated with hadronic reactions, are comparatively bigger than those associated to weak probes, such as neutrinos. These features make e.m. reactions ideal tools to study nuclear dynamics.

Obviously, a theoretical description of this kind of reactions is a demanding task owing to the presence of both strong and e.m. interactions. The *ab-initio* description of e.m. observables is, in general, very satisfactory. Whenever possible, we showed comparisons between calculations performed by various groups using different techniques and/or different dynamical schemes. What can be inferred from such comparisons is that (i) the theoretical accuracy is extremely well under control for very light nuclei (see, *e.g.*, the longitudinal response functions in  $^3\text{He}$ —Figure 16), and (ii) the theoretical prediction is very robust since the conventional and  $\chi$ EFT approaches agree, in most cases, with each other and with experimental data (see, *e.g.*, the low-momentum elastic form factors of deuteron,  $^3\text{He}/^3\text{H}$  and  $^4\text{He}$ —Figures 10, 11, 12, 13, and 14, as well as the photodisintegration cross section of  $^4\text{He}$ —Figure 24).

There are, however, observables for which a solid understanding of the dynamics has not been achieved yet (see, *e.g.*, the inelastic monopole transition form factor of  $^4\text{He}$ —Figure 19). There, calculations with different realistic Hamiltonians disagree with each other and with experiments. Such challenging observables are very interesting, in that they provide an alternative tool to better understand and constrain the present knowledge of the nuclear dynamics.

In general, comparisons of theoretical calculations with available experimental data indicate that, if one aims at a well-founded and accurate description of the experimental data, (iii) many-body components in the e.m. currents and (iv) many-body potentials in the nuclear Hamiltonians need to be accounted for.

Two-body e.m. currents, especially those of one-pion range, are found to be significant in a number of e.m. observables. For example, while they have been found to provide a 15% correction to the calculated nuclear magnetic moments of  $A = 3$  nuclei, their contribution has been found to be as large as 40% of the total calculated magnetic moment of  $^9\text{C}$  (Figure 8), a sizable correction which cannot be neglected. Similarly, two-body e.m. currents have been recently found to provide corrections at the  $\sim 20 - 30\%$  level in a number of calculated  $M1$  transitions between low-lying excited states of  $^8\text{Be}$  [321].

Three-body forces are also found to play a crucial role (see, for example, the longitudinal response functions of  $^3\text{He}$  and  $^4\text{He}$ —Figures 16 and 18). This highlights that the study of e.m. reactions complements that of hadronic reactions in the quest to better understand the role of 3N forces.

Furthermore, the development of new many-body approaches, able to overcome stumbling blocks such as the *ab-initio* description of reactions involving more than four nucleons, has just started to reveal its potential. Recent application of such methods to, for example, the photodisintegration of  $^{16}\text{O}$  (Figure 27) and radiative capture reactions (Figure 29 and 30), are just the first examples of interesting problems that can now be tackled and more

is expected to come in the future. In fact, the inclusion of the important two-body currents and 3N forces is presently being actively pursued by the theoretical community. When these further steps are achieved, the present uncertainty due to the use of truncated dynamical input (for  $A > 4$ ) nuclei will be largely reduced. In the mean time, new experimental activity is being planned, as we referred to whenever possible, and several laboratories in the world are aiming at reducing the error bars of previous measurements and/or measuring new quantities predicted by the theory, with the common aim to further understand nuclear dynamics.

### Acknowledgments

This work was supported by the Natural Sciences and Engineering Research Council (NSERC) and the National Research Council of Canada (S.B.), and by the National Science Foundation, grant No. PHY-1068305 and the U.S. Department of Energy, Office of Nuclear Physics, contract No. DE-FG02-09ER41621 (S.P.).

We would like to thank W. Leidemann, G. Orlandini, R. Schiavilla, M. Schindler and R.B. Wiringa for a critical reading of the manuscript and for useful discussions at various stages of this review. We are grateful to K. Nollett, A. Kievsky, M. Piarulli, S.C. Pieper and M. Viviani for useful discussions. We are thankful to A. Lovato, T. Neff, D.R. Phillips and S. Quaglioni for providing us with their original data and with helpful elucidations on their calculations. We thank Y. Tanaka for helping with the graphics, and B. Davids and E. Ricard-McCutchan for useful discussions on experimental techniques. Finally, we owe sincere thanks to all our colleagues and friends from the various institutions, both experimentalists and theorists, with whom we collaborate on the quest of understanding the nuclear dynamics with e.m. probes.

### Acronyms and abbreviations

#### *Miscellaneous*

3N	Three-nucleon
4N	Four-nucleon
$\chi$ EFT	Chiral effective field theory
CT	Contact term
EFT	Effective field theory
e.m.	Electromagnetic
IA	Impulse approximation
LEC	Low Energy Constant
MEC	Meson exchange currents
NN	Nucleon-nucleon
NR	Non-relativistic
OPE	One-pion exchange
QCD	Quantum chromodynamics
RC	Relativistic correction
SNPA	Standard nuclear physics approach
SRG	Similarity renormalization group
TPE	Two-pion exchange
UCOM	Unitary correlation operator method



*Nuclear potentials*

AV18	Argonne- $v_{18}$ NN potential [76]
AV8'	Argonne- $v'_{8}$ NN potential [65]
IL2	Illinois-2 3N potential [79]
IL7	Illinois-7 3N potential [78]
JISP	$J$ -matrix inverse scattering potential [243]
TM	Tucson-Melbourne 3N potential [194]
UIX	Urbana IX 3N potential [77]

*Computational methods*

CC	Coupled-cluster [73]
EIHH	Effective interaction hyperspherical harmonics [61, 62]
FMD	Fermionic Molecular Dynamics [74]
GFMC	Green's function Monte Carlo [67]
HH	Hyperspherical harmonics [58]
LIT	Lorentz integral transform [59, 60]
NCSM	No-core shell model [69, 70]
VMC	Variational Monte Carlo [67]

**References**

- [1] J. De Forest, T. and J. Walecka, *Adv. Phys.* **15**, 1 (1966).
- [2] T. Donnelly and J. Walecka, *Ann. Rev. Nucl. Part. Sci.* **25**, 329 (1975).
- [3] T. W. Donnelly and I. Sick, *Rev. Mod. Phys.* **56**, 461 (1984).
- [4] A. A. Aguilar-Arevalo, A. O. Bazarko, S. J. Brice, B. C. Brown, L. Bugel, J. Cao, L. Coney, J. M. Conrad, D. C. Cox, A. Curioni, Z. Djurcic, D. A. Finley, B. T. Fleming, R. Ford, F. G. Garcia, G. T. Garvey, C. Green, J. A. Green, T. L. Hart, E. Hawker, R. Imlay, R. A. Johnson, P. Kasper, T. Katori, T. Kobilarcik, I. Kourbanis, S. Koutsoliotas, E. M. Laird, J. M. Link, Y. Liu, Y. Liu, W. C. Louis, K. B. M. Mahn, W. Marsh, P. S. Martin, G. McGregor, W. Metcalf, P. D. Meyers, F. Mills, G. B. Mills, J. Monroe, C. D. Moore, R. H. Nelson, P. Nienaber, S. Ouedraogo, R. B. Patterson, D. Perevalov, C. C. Polly, E. Prebys, J. L. Raaf, H. Ray, B. P. Roe, A. D. Russell, V. Sandberg, R. Schirato, D. Schmitz, M. H. Shaevitz, F. C. Shoemaker, D. Smith, M. Sorel, P. Spentzouris, I. Stancu, R. J. Stefanski, M. Sung, H. A. Tanaka, R. Tayloe, M. Tzanov, R. Van de Water, M. O. Wascko, D. H. White, M. J. Wilking, H. J. Yang, G. P. Zeller, and E. D. Zimmerman (MiniBooNE Collaboration), *Phys. Rev. Lett.* **100**, 032301 (2008).
- [5] A. Gade and T. Glasmacher, *Progress in Particle and Nucl. Phys.* **60**, 161 (2008).
- [6] H. Griesshammer, J. McGovern, D. Phillips, and G. Feldman, *Prog. Part. Nucl. Phys.* **67**, 841 (2012).
- [7] R. Machleidt, *Adv. Nucl. Phys.* **19**, 189 (1989).
- [8] R. Gilman and F. Gross, *J. Phys. G: Nucl. Part. Phys.* **28**, R37 (2002), and references therein.
- [9] S. A. Pinto, A. Stadler, and F. Gross, *Phys. Rev. C* **79**, 054006 (2009).

- [10] L. E. Marcucci, F. Gross, M. Piarulli, and R. Schiavilla, in preparation, to appear on J. Phys. G.
- [11] F. Villars, Phys. Rev. **72**, 256 (1947).
- [12] H. Miyazawa, Progress of Theoretical Physics **6**, 801 (1951).
- [13] D. Riska and G. Brown, Phys. Lett. B **38**, 193 (1972).
- [14] M. Chemtob and M. Rho, Nucl. Phys. A **163**, 1 (1971).
- [15] W. Fabian and H. Arenhövel, Nucl. Phys. A **314**, 253 (1979).
- [16] M. Rho and D. Wilkinson, *Mesons in nuclei*, Mesons in Nuclei No. v. 2 (North Holland Pub. Co., 1979).
- [17] I. Towner, Progress in Particle and Nucl. Phys. **11**, 91 (1984).
- [18] A. Buchmann, W. Leidemann, and H. Arenhövel, Nucl. Phys. A **443**, 726 (1985).
- [19] D. O. Riska, Progress in Particle and Nucl. Phys. **11**, 199 (1984).
- [20] D. O. Riska, Physics Reports **181**, 207 (1989).
- [21] L. E. Marcucci, M. Viviani, R. Schiavilla, A. Kievsky, and S. Rosati, Phys. Rev. C **72**, 014001 (2005).
- [22] L. E. Marcucci, M. Pervin, S. C. Pieper, R. Schiavilla, and R. B. Wiringa, Phys. Rev. C **78**, 065501 (2008).
- [23] J. Carlson and R. Schiavilla, Rev. Mod. Phys. **70**, 743 (1998), and references therein.
- [24] A. Lovato, S. Gandolfi, R. Butler, J. Carlson, E. Lusk, *et al.*, Phys. Rev. Lett. **111**, 092501 (2013).
- [25] S. Weinberg, Phys. Lett. B **251**, 288 (1990).
- [26] S. Weinberg, Nucl. Phys. B **363**, 3 (1991).
- [27] S. Weinberg, Phys. Lett. B **295**, 114 (1992).
- [28] U. van Kolck, Phys. Rev. C **49**, 2932 (1994).
- [29] C. Ordóñez and U. van Kolck, Phys. Lett. B **291**, 459 (1992).
- [30] C. Ordóñez, L. Ray, and U. van Kolck, Phys. Rev. C **53**, 2086 (1996).
- [31] E. Epelbaum, H.-W. Hammer, and U.-G. Meißner, Rev. Mod. Phys. **81**, 1773 (2009), and references therein.
- [32] E. Epelbaum and U.-G. Meißner, Ann. Rev. Nucl. Part. Sci. **62**, 159 (2012), and references therein.
- [33] R. Machleidt and D. Entem, Physics Reports **503**, 1 (2011), and references therein.
- [34] H. Krebs and E. Epelbaum, Few-Body Systems **50**, 295.
- [35] H. Krebs, PoS **CD12**, 014 (2013).
- [36] M. Piarulli and R. Schiavilla, in preparation.
- [37] S. Pastore, R. Schiavilla, and J. L. Goity, Phys. Rev. C **78**, 064002 (2008).
- [38] U. V. Kolck, Progress in Particle and Nucl. Phys. **43**, 337 (1999).
- [39] V. Bernard, N. Kaiser, and U.-G. Meißner, International Journal of Modern Physics E **04**, 193 (1995).
- [40] S. R. Beane, P. F. Bedaque, W. C. Haxton, D. R. Phillips, and M. J. Savage, (2000).
- [41] P. F. Bedaque and U. van Kolck, Ann. Rev. Nucl. Part. Sci. **52**, 339 (2002).
- [42] S. Scherer and M. R. Schindler, Lect. Notes Phys. **830**, pp.1 (2012).

- [43] L. Platter, *Few-Body Systems* **46**, 139.
- [44] T.-S. Park, D.-P. Min, and M. Rho, *Physics Reports* **233**, 341 (1993).
- [45] T.-S. Park, D.-P. Min, and M. Rho, *Nucl. Phys. A* **596**, 515 (1996).
- [46] S. Pastore, L. Girlanda, R. Schiavilla, M. Viviani, and R. B. Wiringa, *Phys. Rev. C* **80**, 034004 (2009).
- [47] S. Pastore, L. Girlanda, R. Schiavilla, and M. Viviani, *Phys. Rev. C* **84**, 024001 (2011).
- [48] M. Piarulli, L. Girlanda, L. Marcucci, S. Pastore, R. Schiavilla, *et al.*, *Phys. Rev. C* **87**, 014006 (2013).
- [49] S. Kölling, E. Epelbaum, H. Krebs, and U. G. Meißner, *Phys. Rev. C* **80**, 045502 (2009).
- [50] S. Kölling, E. Epelbaum, H. Krebs, and U.-G. Meißner, *Phys. Rev. C* **84**, 054008 (2011).
- [51] W. Leidemann and G. Orlandini, *Prog. Part. Nucl.* **68**, 158 (2013).
- [52] O. Yakubovsky, *Sov. J. Nucl. Phys.* **5**, 937 (1967).
- [53] A. Kievsky, S. Rosati, and M. Viviani, *Nucl. Phys.* **A551**, 241 (1993).
- [54] A. Kievsky, M. Viviani, and S. Rosati, *Nucl. Phys.* **A577**, 511 (1994).
- [55] A. Kievsky, L. E. Marcucci, S. Rosati, and M. Viviani, *Few-Body Systems* **22**, 1 (1997).
- [56] M. Viviani, A. Kievsky, and S. Rosati, *Phys. Rev. C* **71**, 024006 (2005).
- [57] M. Viviani, L. Marcucci, S. Rosati, A. Kievsky, and L. Girlanda, *Few Body Syst.* **39**, 159 (2006).
- [58] A. Kievsky, S. Rosati, M. Viviani, L. Marcucci, and L. Girlanda, *J. Phys.* **G35**, 063101 (2008).
- [59] V. D. Efros, W. Leidemann, and G. Orlandini, *Phys. Lett. B* **338**, 130 (1994).
- [60] V. D. Efros, W. Leidemann, G. Orlandini, and N. Barnea, *Journal of Physics G: Nuclear and Particle Physics* **34**, R459 (2007).
- [61] N. Barnea, W. Leidemann, and G. Orlandini, *Phys. Rev. C* **61**, 054001 (2000).
- [62] N. Barnea, W. Leidemann, and G. Orlandini, *Nucl. Phys. A* **693**, 565 (2001).
- [63] J. Carlson, *Phys. Rev. C* **36**, 2026 (1987).
- [64] R. B. Wiringa, *Phys. Rev. C* **43**, 1585 (1991).
- [65] B. S. Pudliner, V. R. Pandharipande, J. Carlson, S. C. Pieper, and R. B. Wiringa, *Phys. Rev. C* **56**, 1720 (1997).
- [66] R. B. Wiringa, S. C. Pieper, J. Carlson, and V. Pandharipande, *Phys. Rev. C* **62**, 014001 (2000).
- [67] S. C. Pieper and R. B. Wiringa, *Annual Review of Nuclear and Particle Science* **51**, 53 (2001), and references therein.
- [68] M. Pervin, S. C. Pieper, and R. B. Wiringa, *Phys. Rev. C* **76**, 064319 (2007).
- [69] P. Navrátil, S. Quaglioni, I. Stetcu, and B. R. Barrett, *Journal of Physics G: Nuclear and Particle Physics* **36**, 083101 (2009), and references therein.
- [70] B. R. Barrett, P. Navrátil, and J. P. Vary, *Prog. Part. Nucl. Phys.* **69**, 131 (2013), and references therein.
- [71] D. J. Dean and M. Hjorth-Jensen, *Phys. Rev. C* **69**, 054320 (2004).

- [72] G. Hagen, T. Papenbrock, D. J. Dean, and M. Hjorth-Jensen, *Phys. Rev. C* **82**, 034330 (2010).
- [73] G. Hagen, T. Papenbrock, M. Hjorth-Jensen, and D. J. Dean, accepted for publication in *Reports on Progress in Physics* (2013), and references therein, arXiv:1312.7872 [nucl-th].
- [74] T. Neff and H. Feldmeier, *The European Physical Journal Special Topics* **156**, 69 (2008).
- [75] R. Machleidt, *Phys. Rev. C* **63**, 024001 (2001).
- [76] R. B. Wiringa, V. G. J. Stoks, and R. Schiavilla, *Phys. Rev. C* **51**, 38 (1995).
- [77] B. Pudliner, V. Pandharipande, J. Carlson, and R. B. Wiringa, *Phys. Rev. Lett.* **74**, 4396 (1995).
- [78] S. C. Pieper, V. R. Pandharipande, R. B. Wiringa, and J. Carlson, *Phys. Rev. C* **64**, 014001 (2001).
- [79] S. C. Pieper, *AIP Conference Proceedings* **1011**, 143 (2008).
- [80] J.-i. Fujita and H. Miyazawa, **17**, 360 (1957).
- [81] J.-i. Fujita and H. Miyazawa, **17**, 366 (1957).
- [82] S. C. Pieper, K. Varga, and R. B. Wiringa, *Phys. Rev. C* **66**, 044310 (2002).
- [83] S. C. Pieper, R. B. Wiringa, and J. Carlson, *Phys. Rev. C* **70**, 054325 (2004).
- [84] S. C. Pieper, *Nucl. Phys.* **A751**, 516 (2005).
- [85] R. G. Sachs, *Phys. Rev.* **126**, 2256 (1962).
- [86] T. Ericson and W. Weise, *Pions and nuclei*, Oxford Science Publications (Clarendon Press, 1988).
- [87] M. Viviani, R. Schiavilla, and A. Kievsky, *Phys. Rev.* **C54**, 534 (1996).
- [88] R. Schiavilla, V. Pandharipande, and D.-O. Riska, *Phys. Rev.* **C40**, 2294 (1989).
- [89] J. Carlson, D. O. Riska, R. Schiavilla, and R. B. Wiringa, *Phys. Rev. C* **42**, 830 (1990).
- [90] L. Marcucci, D. Riska, and R. Schiavilla, *Phys. Rev.* **C58**, 3069 (1998).
- [91] W. Fabian and H. Arenhövel, *Nucl. Phys. A* **258**, 461 (1976).
- [92] H. Weber and H. Arenhövel, *Physics Reports* **36**, 277 (1978).
- [93] M. Schwamb, *Physics Reports* **485**, 109 (2010).
- [94] E. Epelbaum, W. Glöckle, and U.-G. Meißner, *Nucl. Phys. A* **637**, 107 (1998).
- [95] E. Epelbaum, W. Glöckle, and U.-G. Meißner, *Nucl. Phys. A* **671**, 295 (2000).
- [96] E. Epelbaum, W. Glöckle, and U.-G. Meißner, *Nucl. Phys. A* **747**, 362 (2005).
- [97] D. Entem and R. Machleidt, *Phys. Lett.* **B524**, 93 (2002).
- [98] D. R. Entem and R. Machleidt, *Phys. Rev. C* **68**, 041001 (2003).
- [99] L. Girlanda, S. Pastore, R. Schiavilla, and M. Viviani, *Phys. Rev.* **C81**, 034005 (2010).
- [100] D. Gazit, S. Quaglioni, and P. Navrátil, *Phys. Rev. Lett.* **103**, 102502 (2009).
- [101] “Lenpic collaboration,” [www.lenpic.org](http://www.lenpic.org).
- [102] R. Roth, J. Langhammer, A. Calci, S. Binder, and P. Navrátil, *Phys. Rev. Lett.* **107**, 072501 (2011).
- [103] E. Epelbaum, H. Krebs, D. Lee, and U.-G. Meißner, *Phys. Rev. Lett.* **104**, 142501 (2010).

- [104] E. Epelbaum, H. Krebs, D. Lee, and U.-G. Meißner, *Phys. Rev. Lett.* **106**, 192501 (2011).
- [105] T. A. Lähde, E. Epelbaum, H. Krebs, D. Lee, U.-G. Meiner, *et al.*, (2013), arXiv:1311.0477 [nucl-th] .
- [106] E. Epelbaum, H. Krebs, T. A. Lähde, D. Lee, and U.-G. Meißner, *Phys. Rev. Lett.* **109**, 252501 (2012).
- [107] E. Epelbaum, H. Krebs, T. A. Lähde, D. Lee, U.-G. Meiner, *et al.*, *Phys. Rev. Lett.* **112**, 102501 (2014).
- [108] A. Nogga, R. Timmermans, and U. van Kolck, *Phys. Rev. C* **72**, 054006 (2005).
- [109] M. Pavon Valderrama and E. Ruiz Arriola, *Phys. Rev. C* **74**, 054001 (2006).
- [110] E. Epelbaum and U.-G. Meißner, *Few Body Syst.* **54**, 2175 (2013).
- [111] D. R. Phillips, *PoS CD12*, 013 (2013).
- [112] E. Epelbaum, *PoS ConfinementX*, 014 (2012).
- [113] M. Walzl and U.-G. Meißner, *Phys. Lett. B* **513**, 37 (2001).
- [114] D. R. Phillips, *Phys. Lett. B* **567**, 12 (2003).
- [115] D. R. Phillips, *J. Phys.* **G34**, 365 (2007).
- [116] L. Girlanda, S. Pastore, R. Schiavilla, and M. Viviani, *EPJ Web Conf.* **3**, 01004 (2010).
- [117] J. L. Friar, *Annals of Physics* **104**, 380 (1977).
- [118] J. Eisenberg and W. Greiner, *Nuclear Theory: Excitation Mechanisms of the Nucleus*.
- [119] P. Ring and P. Schuck, *The nuclear many-body problem* (Springer-Verlag, 1980).
- [120] S. Boffi, C. Giusti, F. D. Pacati, and M. Radici, *Electromagnetic response of Atomic Nuclei* (Oxford University Press, 1996).
- [121] I. Sick, *Prog. Part. Nucl. Phys.* **47**, 245 (2001).
- [122] A. J. F. Siegert, *Phys. Rev.* **52**, 787 (1937).
- [123] S. Pastore, S. C. Pieper, R. Schiavilla, and R. Wiringa, *Phys. Rev.* **C87**, 035503 (2013).
- [124] A. Amroun, V. Breton, J. Cavedon, B. Frois, D. Goutte, *et al.*, *Nucl. Phys.* **A579**, 596 (1994).
- [125] D. Tilley, C. Cheves, J. Godwin, G. Hale, H. Hofmann, J. Kelley, C. Sheu, and H. Weller, *Nucl. Phys. A* **708**, 3 (2002).
- [126] D. Tilley, J. Kelley, J. Godwin, D. Millener, J. Purcell, C. Sheu, and H. Weller, *Nucl. Phys. A* **745**, 155 (2004).
- [127] G. Audi, A. Wapstra, and C. Thibault, *Nucl. Phys.* **A729**, 337 (2002).
- [128] J. Purcell, J. Kelley, E. Kwan, C. Sheu, and H. Weller, *Nucl. Phys.* **A848**, 1 (2010).
- [129] Y.-H. Song, R. Lazauskas, T.-S. Park, and D.-P. Min, *Phys. Lett. B* **656**, 174 (2007).
- [130] Y.-H. Song, R. Lazauskas, and T.-S. Park, *Phys. Rev. C* **79**, 064002 (2009).
- [131] P. Maris and J. P. Vary, *Int. J. Mod. Phys.* **E22**, 1330016 (2013).
- [132] D. Borremans, D. Yordanov, D. Balabanski, G. Neyens, J. Lassen, *et al.*, *Phys. Rev. C* **72**, 044309 (2005).
- [133] R. B. Wiringa, *Phys. Rev.* **C73**, 034317 (2006).
- [134] M. Garcon and J. Van Orden, *Adv. Nucl. Phys.* **26**, 293 (2001).
- [135] H. Arenhövel, F. Ritz, and T. Wilbois, *Phys. Rev.* **C61**, 034002 (2000).

- [136] R. Schiavilla and V. Pandharipande, *Phys. Rev.* **C65**, 064009 (2002).
- [137] D. R. Phillips and T. Cohen, *Nucl. Phys.* **A668**, 45 (2000).
- [138] D. R. Phillips, *J. Phys.* **G31**, S1263 (2005).
- [139] M. P. Valderrama, A. Nogga, E. Ruiz Arriola, and D. R. Phillips, *Eur. Phys. J.* **A36**, 315 (2008).
- [140] S. Kolling, E. Epelbaum, and D. Phillips, *Phys. Rev.* **C86**, 047001 (2012).
- [141] C. Buchanan and M. Yearian, *Phys. Rev. Lett.* **15**, 303 (1965).
- [142] D. Benaksas, D. Drickey, and D. Frerejacque, *Phys. Rev.* **148**, 1327 (1966).
- [143] J. Elias, J. Friedman, G. Hartmann, H. Kendall, P. Kirk, *et al.*, *Phys. Rev.* **177**, 2075 (1969).
- [144] S. Galster, H. Klein, J. Moritz, K. Schmidt, D. Wegener, *et al.*, *Nucl. Phys.* **B32**, 221 (1971).
- [145] R. Berard, F. Buskirk, E. Dally, J. Dyer, X. Maruyama, *et al.*, *Phys. Lett.* **B47**, 355 (1973).
- [146] R. Arnold, B. Chertok, E. Dally, A. Grigorian, C. Jordan, *et al.*, *Phys. Rev. Lett.* **35**, 776 (1975).
- [147] G. Simon, C. Schmitt, and V. Walther, *Nucl. Phys.* **A364**, 285 (1981).
- [148] R. Cramer, M. Renkhoff, J. Drees, U. Ecker, D. Jagoda, *et al.*, *Z. Phys.* **C29**, 513 (1985).
- [149] S. Platchkov, A. Amroun, S. Auffret, J. Cavedon, P. Dreux, *et al.*, *Nucl. Phys.* **A510**, 740 (1990).
- [150] D. Abbott *et al.* (Jefferson Lab t(20) Collaboration), *Phys. Rev. Lett.* **82**, 1379 (1999).
- [151] L. Alexa *et al.* (Jefferson Lab Hall A Collaboration), *Phys. Rev. Lett.* **82**, 1374 (1999).
- [152] M. Schulze, D. Beck, M. Farkhondeh, S. Gilad, R. Goloskie, *et al.*, *Phys. Rev. Lett.* **52**, 597 (1984).
- [153] I. The, J. Arvieux, D. Beck, E. Beise, A. Boudard, *et al.*, *Phys. Rev. Lett.* **67**, 173 (1991).
- [154] C. Zhang, M. Kohl, T. Akdogan, R. Alarcon, W. Bertozzi, *et al.*, *Phys. Rev. Lett.* **107**, 252501 (2011).
- [155] V. Dmitriev, D. Nikolenko, S. Popov, I. Rachek, Y. Shatunov, *et al.*, *Phys. Lett.* **B157**, 143 (1985).
- [156] B. Voitsekhovskiy, D. Nikolenko, K. Ospanov, S. Popov, I. Rachek, *et al.*, *JETP Lett.* **43**, 733 (1986).
- [157] R. A. Gilman, R. Holt, E. Kinney, R. Kowalczyk, S. Mishnev, *et al.*, *Phys. Rev. Lett.* **65**, 1733 (1990).
- [158] D. Nikolenko, H. Arenhövel, L. Barkov, S. Belostotsky, V. Dmitriev, *et al.*, *Phys. Rev. Lett.* **90**, 072501 (2003).
- [159] B. Boden, V. Burkert, G. Knop, G. Kroesen, M. Leenen, *et al.*, *Z. Phys.* **C49**, 175 (1991).
- [160] M. Ferro-Luzzi, M. Bouwhuis, E. Passchier, Z. Zhou, R. Alarcon, *et al.*, *Phys. Rev. Lett.* **77**, 2630 (1996).
- [161] M. Bouwhuis, R. Alarcon, T. Botto, J. van den Brand, H. Bulten, *et al.*, *Phys. Rev. Lett.* **82**, 3755 (1999).

- [162] D. Abbott *et al.* (JLAB t(20) Collaboration), Phys. Rev. Lett. **84**, 5053 (2000).
- [163] S. Auffret, J. Cavedon, J. Clemens, B. Frois, D. Goutte, *et al.*, Phys. Rev. Lett. **54**, 649 (1985).
- [164] P. E. Bosted, A. Katramatou, R. Arnold, D. Benton, L. Clogher, *et al.*, Phys. Rev. **C42**, 38 (1990).
- [165] E. Epelbaum, A. Gasparyan, J. Gegelia, and M. Schindler, Eur. Phys. J. **A50**, 51 (2014).
- [166] E. Epelbaum and J. Gegelia, Phys. Lett. **B716**, 338 (2012).
- [167] A. Amroun, V. Breton, J. Cavedon, B. Frois, D. Goutte, *et al.*, Nucl. Phys. **A579**, 596 (1994).
- [168] J. Golak, R. Skibinski, H. Witala, W. Glockle, A. Nogga, *et al.*, Phys.Rept. **415**, 89 (2005).
- [169] R. Schiavilla, V. R. Pandharipande, and D. O. Riska, Phys. Rev. C **41**, 309 (1990).
- [170] M. Viviani, R. Schiavilla, B. Kubis, R. Lewis, L. Girlanda, A. Kievsky, L. E. Marcucci, and S. Rosati, Phys. Rev. Lett. **99**, 112002 (2007).
- [171] R. F. Frosch, J. S. McCarthy, R. E. Rand, and M. R. Yearian, Phys. Rev. **160**, 874 (1967).
- [172] S. Bacca, N. Barnea, W. Leidemann, and G. Orlandini, Phys. Rev. Lett. **110**, 042503 (2013).
- [173] P. Navrátil, Few-Body Systems **41**, 117 (2007).
- [174] D. Gazit, S. Bacca, N. Barnea, W. Leidemann, and G. Orlandini, Phys. Rev. Lett. **96**, 112301 (2006).
- [175] M. Brodeur, T. Brunner, C. Champagne, S. Ettenauer, M. J. Smith, A. Lapierre, R. Ringle, V. L. Ryjkov, S. Bacca, P. Delheij, G. W. F. Drake, D. Lunney, A. Schwenk, and J. Dilling, Phys. Rev. Lett. **108**, 052504 (2012).
- [176] A. Camsonne *et al.* (Jefferson Lab Hall A Collaboration), Phys. Rev. Lett. **112**, 132503 (2014), arXiv:1309.5297 [nucl-ex] .
- [177] R. B. Wiringa and R. Schiavilla, Phys. Rev. Lett. **81**, 4317 (1998).
- [178] H. D. Vries, C. D. Jager, and C. D. Vries, Atomic Data and Nuclear Data Tables **36**, 495 (1987).
- [179] M. N. Rosenbluth, Phys. Rev. **79**, 615 (1950).
- [180] H. Arenhövel, W. Leidemann, and E. Tomusiak, .
- [181] C.-J. Yang and D. R. Phillips, Eur. Phys. J. **A49**, 122 (2013).
- [182] C. J. Yang, C. Elster, and D. R. Phillips, Phys. Rev. C **80**, 034002 (2009).
- [183] H. Arenhövel, W. Leidemann, and E. L. Tomusiak, Phys. Rev. C **46**, 455 (1992).
- [184] R. Machleidt, K. Holinde, and C. Elster, Physics Reports **149**, 1 (1987).
- [185] W. Gloeckle, J. Golak, R. Skibinski, H. Witala, H. Kamada, and A. Nogga, Eur. Phys. J. A **21**, 335 (2004).
- [186] M. Viviani, A. Kievsky, L. E. Marcucci, S. Rosati, and R. Schiavilla, Phys. Rev. C **61**, 064001 (2000).
- [187] A. Deltuva, L. P. Yuan, J. Adam, and P. U. Sauer, Phys. Rev. C **70**, 034004 (2004).
- [188] L. Yuan, W. Leidemann, V. D. Efros, G. Orlandini, and E. L. Tomusiak, Phys. Lett. B **706**, 90 (2011).

- [189] G. A. Retzlaff, H. S. Caplan, E. L. Hallin, D. M. Skopik, D. Beck, K. I. Blomqvist, G. Dobson, K. Dow, M. Farkhondeh, J. Flanz, S. Kowalski, W. W. Sapp, C. P. Sargent, D. Tieger, W. Turchinets, C. F. Williamson, W. Dodge, X. K. Maruyama, J. W. Lightbody, R. Goloskie, J. McCarthy, T. S. Ueng, R. R. Whitney, B. Quinn, S. Dytman, K. Von Reden, R. Schiavilla, and J. A. Tjon, *Phys. Rev. C* **49**, 1263 (1994).
- [190] J. Carlson, J. Jourdan, R. Schiavilla, and I. Sick, *Phys. Rev. C* **65**, 024002 (2002).
- [191] V. D. Efros, W. Leidemann, G. Orlandini, and E. L. Tomusiak, *Phys. Rev. C* **69**, 044001 (2004).
- [192] W. Leidemann, V. Efros, G. Orlandini, and E. Tomusiak, *Few-Body Systems* **47**, 157 (2010).
- [193] S. Della Monaca, V. D. Efros, A. Khugaev, W. Leidemann, G. Orlandini, E. L. Tomusiak, and L. P. Yuan, *Phys. Rev. C* **77**, 044007 (2008).
- [194] S. A. Coon and H. K. Hahn, *Few-Body Syst.* **30**, 131 (2001).
- [195] H. Arenhövel and M. Schwamb, *Eur. Phys. Jour. A* **12**, 207 (2001).
- [196] D. O. Riska, *Phys. Scr.* **31**, 471 (1985).
- [197] V. D. Efros, W. Leidemann, G. Orlandini, and E. L. Tomusiak, *Phys. Rev. C* **81**, 034001 (2010).
- [198] V. D. Efros, W. Leidemann, G. Orlandini, and E. L. Tomusiak, *Phys. Rev. C* **83**, 057001 (2011).
- [199] V. D. Efros, W. Leidemann, and G. Orlandini, *Phys. Rev. C* **58**, 582 (1998).
- [200] S. Bacca, N. Barnea, W. Leidemann, and G. Orlandini, *Phys. Rev. Lett.* **102**, 162501 (2009).
- [201] S. A. Dytman, A. M. Bernstein, K. I. Blomqvist, T. J. Pavel, B. P. Quinn, R. Altemus, J. S. McCarthy, G. H. Mechtel, T. S. Ueng, and R. R. Whitney, *Phys. Rev. C* **38**, 800 (1988).
- [202] D. J. Zgheche, A. and, M. Bernheim, M. Brussel, *et al.*, *Nucl. Phys. A* **572**, 513 (1994).
- [203] J. Carlson and R. Schiavilla, *Phys. Rev. Lett.* **68**, 3682 (1992).
- [204] J. Carlson and R. Schiavilla, *Phys. Rev. C* **49**, R2880 (1994).
- [205] V. D. Efros, W. Leidemann, and G. Orlandini, *Phys. Rev. Lett.* **78**, 4015 (1997).
- [206] D. Andreasi, W. Leidemann, C. Reiß, and M. Schwamb, *The European Physical Journal A - Hadrons and Nuclei* **24**, 361 (2005).
- [207] S. Bacca, N. Barnea, W. Leidemann, and G. Orlandini, *Phys. Rev. C* **80**, 064001 (2009).
- [208] S. Bacca, *Few Body Syst.* **54**, 903 (2013).
- [209] S. Bacca, H. Arenhövel, N. Barnea, W. Leidemann, and G. Orlandini, *Phys. Rev. C* **76**, 014003 (2007).
- [210] R. Frosch, R. Rand, M. Yearian, H. Crannell, and L. Suelzle, *Phys. Lett.* **19**, 155 (1965).
- [211] T. Walcher, *Phys. Lett. B* **31**, 442 (1970).
- [212] G. Köbschall, C. Ottermann, K. Maurer, K. Roehrich, V. Schmitt, and V. Walter, *Nucl. Phys. A* **405**, 648 (1983).
- [213] E. Hiyama, B. Gibson, and M. Kamimura, *Phys. Rev. C* **70**, 031001 (2004).



- [214] S. Bacca, N. Barnea, W. Leidemann, and G. Orlandini, (2014), arXiv:1403.6961 [nucl-th] .
- [215] N. Pietralla *et al.*, Preliminary Funding Proposal to the DFG for a Collaborative Research Centre at TU Darmstadt, Project A1 , p. 31 (2013).
- [216] F. Cappuzzello *et al.*, Nucl. Instr. and Meth. **A638**, 74 (2011).
- [217] S. Quaglioni, V. D. Efros, W. Leidemann, and G. Orlandini, Phys. Rev. C **72**, 064002 (2005).
- [218] W. H. Dickoff and D. Van Neck, *Many-body theory exposed!* (World Scientific, 2005).
- [219] S. Quaglioni, W. Leidemann, G. Orlandini, N. Barnea, and V. D. Efros, Phys. Rev. C **69**, 044002 (2004).
- [220] W. Ford, R. Schiavilla, and J. Van Orden, Phys. Rev. C **89**, 034004 (2014).
- [221] D. Andreasi, S. Quaglioni, V. D. Efros, W. Leidemann, and G. Orlandini, Eur. Phys. J. A **27**, 47 (2006).
- [222] G. Orlandini and M. Traini, Reports on Progress in Physics **54**, 257 (1991).
- [223] J. Jourdan, Nucl. Phys. A **603**, 117 (1996).
- [224] A. Lovato, S. Gandolfi, J. Carlson, S. C. Pieper, and R. Schiavilla, Phys. Rev. Lett. **112**, 182502 (2014).
- [225] H. Arenhövel and M. Sanzone, Few-Body Syst. Suppl. **3**, 1 (1991).
- [226] D. Rozpedzik, J. Golak, S. Kölling, E. Epelbaum, R. Skibiński, H. Witała, and H. Krebs, Phys. Rev. C **83**, 064004 (2011).
- [227] S. Ying, E. M. Henley, and G. A. Miller, Phys. Rev. C **38**, 1584 (1988).
- [228] G. Bampa, W. Leidemann, and H. Arenhövel, Phys. Rev. C **84**, 034005 (2011).
- [229] E. Epelbaum, Prog. Part. Nucl. Phys. **57**, 654 (2006).
- [230] K.-M. Schmitt and H. Arenhvel, Few-Body Systems **11**, 33 (1991).
- [231] A. Nogga, H. Kamada, and W. Glöckle, Phys. Rev. Lett. **85**, 944 (2000).
- [232] A. Nogga, S. K. Bogner, and A. Schwenk, Phys. Rev. C **70**, 061002 (2004).
- [233] K. Sekiguchi, H. Sakai, H. Witała, W. Glöckle, J. Golak, M. Hatano, H. Kamada, H. Kato, Y. Maeda, J. Nishikawa, A. Nogga, T. Ohnishi, H. Okamura, N. Sakamoto, S. Sakoda, Y. Satou, K. Suda, A. Tamii, T. Uesaka, T. Wakasa, and K. Yako, Phys. Rev. C **65**, 034003 (2002).
- [234] J. Kuroś-Zołnierczuk, H. Witała, J. Golak, H. Kamada, A. Nogga, R. Skibiński, and W. Glöckle, Phys. Rev. C **66**, 024004 (2002).
- [235] R. Skibiński, J. Golak, H. Witała, W. Glöckle, H. Kamada, and A. Nogga, Phys. Rev. C **67**, 054002 (2003).
- [236] J. Golak, R. Skibinski, W. Gloeckle, H. Kamada, A. Nogga, *et al.*, Nucl. Phys. **A707**, 365 (2002).
- [237] J. Golak, H. Kamada, H. Witała, W. Glöckle, J. Kuroś Zolnierczuk, R. Skibiński, V. V. Kotlyar, K. Sagara, and H. Akiyoshi, Phys. Rev. C **62**, 054005 (2000).
- [238] V. D. Efros, W. Leidemann, G. Orlandini, and E. L. Tomusiak, Phys. Lett. **B484**, 223 (2000).
- [239] S. Bacca, Phys. Rev. C **75**, 044001 (2007).
- [240] D. D. Faul, B. L. Berman, P. Meyer, and D. L. Olson, Phys. Rev. C **24**, 849 (1981).

- [241] V. Fetisov, A. Gorbunov, and A. Varfolomeev, Nucl. Phys. A **71**, 305 (1965).
- [242] R. Roth, T. Neff, H. Hergert, and H. Feldmeier, Nucl. Phys. A **745**, 3 (2004).
- [243] A. M. Shirokov, A. I. Mazur, S. A. Zaytsev, J. P. Vary, and T. A. Weber, Phys. Rev. C **70**, 044005 (2004).
- [244] N. Barnea, W. Leidemann, and G. Orlandini, Phys. Rev. C **74**, 034003 (2006).
- [245] R. Skibiński, J. Golak, H. Witała, W. Glöckle, A. Nogga, and H. Kamada, Phys. Rev. C **72**, 044002 (2005).
- [246] M. Lenkewitz, E. Epelbaum, H.-W. Hammer, and U.-G. Meißner, Phys. Lett. B **700**, 365368 (2011).
- [247] H. Kamada, A. Nogga, W. Glöckle, E. Hiyama, M. Kamimura, K. Varga, Y. Suzuki, M. Viviani, A. Kievsky, S. Rosati, J. Carlson, S. C. Pieper, R. B. Wiringa, P. Navrátil, B. R. Barrett, N. Barnea, W. Leidemann, and G. Orlandini, Phys. Rev. C **64**, 044001 (2001).
- [248] J. Carbonell, A. Deltuva, A. C. Fonseca, and R. Lazauskas, to appear in Progress in Particle and Nucl. Phys. (2014).
- [249] R. Raut, W. Tornow, M. Ahmed, A. Crowell, J. Kelley, *et al.*, Phys. Rev. Lett. **108**, 042502 (2012).
- [250] W. Tornow, J. Kelley, R. Raut, G. Rusev, A. Tonchev, *et al.*, Phys. Rev. C **85**, 061001 (2012).
- [251] S. Nakayama, E. Matsumoto, R. Hayami, K. Fushimi, H. Kawasuso, K. Yasuda, T. Yamagata, H. Akimune, H. Ikemizu, M. Fujiwara, M. Yosoi, K. Nakanishi, K. Kawase, H. Hashimoto, T. Oota, K. Sagara, T. Kudoh, S. Asaji, T. Ishida, M. Tanaka, and M. B. Greenfield, Phys. Rev. C **76**, 021305 (2007).
- [252] B. Nilsson *et al.*, Phys. Lett. B **626**, 65 (2005).
- [253] T. Shima, S. Naito, Y. Nagai, T. Baba, K. Tamura, *et al.*, Phys. Rev. C **72**, 044004 (2005).
- [254] S. Quaglioni and P. Navrátil, Phys. Lett. B **652**, 370 (2007).
- [255] I. Stetcu, S. Quaglioni, S. Bacca, B. R. Barrett, C. W. Johnson, P. Navrátil, N. Barnea, W. Leidemann, and G. Orlandini, Nucl. Phys. A **785**, 307 (2007).
- [256] W. Horiuchi, Y. Suzuki, and K. Arai, Phys. Rev. C **85**, 054002 (2012).
- [257] T. Shima *et al.*, AIP Conf. Proc. **1235**, 315 (2010).
- [258] N. Nevo Dinur, N. Barnea, and W. Leidemann, Few-Body Systems, **1** (2013).
- [259] Y. M. Arkatov *et al.*, Yad. Konst. **4**, 55 (1979).
- [260] I. Tanihata, J. Phys. G: Nucl. Part. Phys. **22**, 157 (1996).
- [261] S. Bacca, N. Barnea, W. Leidemann, and G. Orlandini, Phys. Rev. C **69**, 057001 (2004).
- [262] S. Bacca, M. A. Marchisio, N. Barnea, W. Leidemann, and G. Orlandini, Phys. Rev. Lett. **89**, 052502 (2002).
- [263] R. B. Wiringa and S. C. Pieper, Phys. Rev. Lett. **89**, 182501 (2002).
- [264] T. Aumann, D. Aleksandrov, L. Axelsson, T. Baumann, M. J. G. Borge, L. V. Chulkov, J. Cub, W. Dostal, B. Eberlein, T. W. Elze, H. Emling, H. Geissel, V. Z. Goldberg, M. Golovkov, A. Grünschloß, M. Hellström, K. Hencken, J. Holeczek, R. Holzmann, B. Jonson, A. A. Korshennikov, J. V. Kratz, G. Kraus, R. Kulesa, Y. Leifels,

- A. Leistenschneider, T. Leth, I. Mukha, G. Münzenberg, F. Nickel, T. Nilsson, G. Nyman, B. Petersen, M. Pfützner, A. Richter, K. Riisager, C. Scheidenberger, G. Schrieder, W. Schwab, H. Simon, M. H. Smedberg, M. Steiner, J. Stroth, A. Surowiec, T. Suzuki, O. Tengblad, and M. V. Zhukov, *Phys. Rev. C* **59**, 1252 (1999).
- [265] J. Wang, A. Galonsky, J. J. Kruse, E. Tryggestad, R. H. White-Stevens, P. D. Zecher, Y. Iwata, K. Ieki, A. Horváth, F. Deák, A. Kiss, Z. Seres, J. J. Kolata, J. von Schwarzenberg, R. E. Warner, and H. Schelin, *Phys. Rev. C* **65**, 034306 (2002).
- [266] J. Ahrens, H. Borchert, K. Czock, H. Eppler, H. Gimm, H. Gundrum, M. Kröning, P. Riehn, G. S. Ram, A. Zieger, and B. Ziegler, *Nucl. Phys. A* **251**, 479 (1975).
- [267] S. Bacca, H. Arenhövel, N. Barnea, W. Leidemann, and G. Orlandini, *Phys. Lett. B* **603**, 159 (2004).
- [268] W. A. Wurtz, R. E. Pywell, B. E. Norum, S. Kucuker, B. D. Sawatzky, H. R. Weller, M. W. Ahmed, and S. Stave, *Phys. Rev. C* **84**, 044601 (2011).
- [269] M. Borselli, *Total photoabsorption cross section of  ${}^6\text{Li}$*  (M.Sci. Thesis, Trento University, 2012).
- [270] D. Middleton, private communication (2013).
- [271] J. Erler, P. Klüpfel, and P.-G. Reinhard, *J. Phys. G: Nucl. Part. Phys.* **38**, 033101 (2011), and references therein.
- [272] T. Nakatsukasa, *Prog. Theor. Exp. Phys.* **01A207** (2012).
- [273] H.-W. Hammer and D. Phillips, *Nucl. Phys. A* **865**, 17 (2011).
- [274] S. Bacca, N. Barnea, G. Hagen, G. Orlandini, and T. Papenbrock, *Phys. Rev. Lett.* **111**, 122502 (2013).
- [275] S. Bacca, N. Barnea, G. Hagen, G. Orlandini, and T. Papenbrock, in preparation (2014).
- [276] I. J. Thompson and F. M. Nunes, *Nuclear Reactions for Astrophysics* (Cambridge University Press, 2009).
- [277] E. G. Adelberger, S. M. Austin, J. N. Bahcall, A. B. Balantekin, G. Bogaert, L. S. Brown, L. Buchmann, F. E. Cecil, A. E. Champagne, L. de Braekeleer, C. A. Duba, S. R. Elliott, S. J. Freedman, M. Gai, G. Goldring, C. R. Gould, A. Gruzinov, W. C. Haxton, K. M. Heeger, E. Henley, C. W. Johnson, M. Kamionkowski, R. W. Kavanagh, S. E. Koonin, K. Kubodera, K. Langanke, T. Motobayashi, V. Pandharipande, P. Parker, R. G. H. Robertson, C. Rolfs, R. F. Sawyer, N. Shaviv, T. D. Shoppa, K. A. Snover, E. Swanson, R. E. Tribble, S. Turck-Chièze, and J. F. Wilkerson, *Rev. Mod. Phys.* **70**, 1265 (1998).
- [278] E. G. Adelberger, A. García, R. G. H. Robertson, K. A. Snover, A. B. Balantekin, K. Heeger, M. J. Ramsey-Musolf, D. Bemmerer, A. Junghans, C. A. Bertulani, J.-W. Chen, H. Costantini, P. Prati, M. Couder, E. Uberseder, M. Wiescher, R. Cyburt, B. Davids, S. J. Freedman, M. Gai, D. Gazit, L. Gialanella, G. Imbriani, U. Greife, M. Hass, W. C. Haxton, T. Itahashi, K. Kubodera, K. Langanke, D. Leitner, M. Leitner, P. Vetter, L. Winslow, L. E. Marcucci, T. Motobayashi, A. Mukhamedzhanov, R. E. Tribble, K. M. Nollett, F. M. Nunes, T.-S. Park, P. D. Parker, R. Schiavilla, E. C. Simpson, C. Spitaleri, F. Strieder, H.-P. Trautvetter, K. Suemmerer, and S. Typel, *Rev. Mod. Phys.* **83**, 195 (2011), and references therein.
- [279] M. S. Smith, L. H. Kawano, and R. A. Malaney, *Astrophys. J. Suppl.* **85**, 219 (1993).
- [280] K. M. Nollett and G. P. Holder, (2011), arXiv:1112.2683 [astro-ph.CO] .

- [281] K. M. Nollett and G. Steigman, *Phys. Rev. D* **89**, 083508 (2014).
- [282] G. Rupak, *Nucl. Phys.* **A678**, 405 (2000).
- [283] L. Marcucci, K. M. Nollett, R. Schiavilla, and R. B. Wiringa, *Nucl. Phys.* **A777**, 111 (2006), and references therein.
- [284] S. Mughabghab and N. Holden, *Neutron resonance parameters and thermal cross sections*, Neutron cross sections series No. v. 1, pt. 1.
- [285] E. T. Jurney, P. J. Bendt, and J. C. Browne, *Phys. Rev. C* **25**, 2810 (1982).
- [286] F. L. H. Wolfs, S. J. Freedman, J. E. Nelson, M. S. Dewey, and G. L. Greene, *Phys. Rev. Lett.* **63**, 2721 (1989).
- [287] R. Wervelman, K. Abrahams, H. Postma, J. Booten, and A. V. Hees, *Nucl. Phys. A* **526**, 265 (1991).
- [288] J. Friar, B. Gibson, and G. Payne, *Phys. Lett. B* **251**, 11 (1990).
- [289] R. Schiavilla, R. B. Wiringa, V. Pandharipande, and J. Carlson, *Phys. Rev. C* **45**, 2628 (1992).
- [290] A. Deltuva and A. Fonseca, *Phys. Rev. C* **76**, 021001 (2007).
- [291] R. Lazauskas, *Phys. Rev. C* **79**, 054007 (2009).
- [292] M. Viviani, R. Schiavilla, L. Girlanda, A. Kievsky, and L. E. Marcucci, *Phys. Rev. C* **82**, 044001 (2010).
- [293] L. Girlanda, A. Kievsky, L. E. Marcucci, S. Pastore, R. Schiavilla, and M. Viviani, *Phys. Rev. Lett.* **105**, 232502 (2010).
- [294] R. Lazauskas, Y.-H. Song, and T.-S. Park, *Phys. Rev. C* **83**, 034006 (2011).
- [295] K. Arai, S. Aoyama, Y. Suzuki, P. Descouvemont, and D. Baye, *Phys. Rev. Lett.* **107**, 132502 (2011).
- [296] K. M. Nollett, R. B. Wiringa, and R. Schiavilla, *Phys. Rev. C* **63**, 024003 (2001).
- [297] K. M. Nollett, *Phys. Rev. C* **63**, 054002 (2001).
- [298] P. Navrátil, C. Bertulani, and E. Caurier, *Phys. Lett. B* **634**, 191 (2006).
- [299] P. Navrátil, R. Roth, and S. Quaglioni, *Phys. Lett. B* **704**, 379 (2011).
- [300] S. Quaglioni and P. Navrátil, *Phys. Rev. Lett.* **101**, 092501 (2008).
- [301] S. Quaglioni and P. Navrátil, *Phys. Rev. C* **79**, 044606 (2009).
- [302] S. Bogner, R. Furnstahl, and R. Perry, *Phys. Rev. C* **75**, 061001 (2007).
- [303] T. Neff, *Phys. Rev. Lett.* **106**, 042502 (2011).
- [304] B. S. N. Singh, M. Hass, Y. Nir-El, and G. Haquin, *Phys. Rev. Lett.* **93**, 262503 (2004).
- [305] D. Bemmerer, F. Confortola, H. Costantini, A. Formicola, G. Gyürky, R. Bonetti, C. Broggini, P. Corvisiero, Z. Elekes, Z. Fülöp, G. Gervino, A. Guglielmetti, C. Gustavino, G. Imbriani, M. Junker, M. Laubenstein, A. Lemut, B. Limata, V. Lozza, M. Marta, R. Menegazzo, P. Prati, V. Roca, C. Rolfs, C. R. Alvarez, E. Somorjai, O. Straniero, F. Strieder, F. Terrasi, and H. P. Trautvetter (LUNA Collaboration), *Phys. Rev. Lett.* **97**, 122502 (2006).
- [306] F. Confortola, D. Bemmerer, H. Costantini, A. Formicola, G. Gyürky, P. Bezzon, R. Bonetti, C. Broggini, P. Corvisiero, Z. Elekes, Z. Fülöp, G. Gervino, A. Guglielmetti, C. Gustavino, G. Imbriani, M. Junker, M. Laubenstein, A. Lemut, B. Limata, V. Lozza, M. Marta, R. Menegazzo, P. Prati, V. Roca, C. Rolfs, C. R. Alvarez, E. Somorjai, O. Straniero, F. Strieder, F. Terrasi, and H. P. Trautvetter (LUNA Collaboration), *Phys. Rev. C* **75**, 065803 (2007).

- [307] T. A. D. Brown, C. Bordeanu, K. A. Snover, D. W. Storm, D. Melconian, A. L. Sallaska, S. K. L. Sjue, and S. Triambak, *Phys. Rev. C* **76**, 055801 (2007).
- [308] A. Di Leva, L. Gialanella, R. Kunz, D. Rogalla, D. Schürmann, F. Strieder, M. De Cesare, N. De Cesare, A. D’Onofrio, Z. Fülöp, G. Gyürky, G. Imbriani, G. Mangano, A. Ordine, V. Roca, C. Rolfs, M. Romano, E. Somorjai, and F. Terrasi, *Phys. Rev. Lett.* **102**, 232502 (2009).
- [309] M. Carmona-Gallardo, B. S. Nara Singh, M. J. G. Borge, J. A. Briz, M. Cubero, B. R. Fulton, H. Fynbo, N. Gordillo, M. Hass, G. Haquin, A. Maira, E. Nácher, Y. Nir-El, V. Kumar, J. McGrath, A. Muñoz-Martín, A. Perea, V. Pesudo, G. Ribeiro, J. Sánchez del Rio, O. Tengblad, R. Yaniv, and Z. Yungreis, *Phys. Rev. C* **86**, 032801 (2012).
- [310] R. Roth, T. Neff, and H. Feldmeier, *Progress in Particle and Nucl. Phys.* **65**, 50 (2010).
- [311] G. Rupak and D. Lee, *Phys. Rev. Lett.* **111**, 032502 (2013).
- [312] G. Rupak and R. Higa, *Phys. Rev. Lett.* **106**, 222501 (2011).
- [313] X. Zhang, K. M. Nollett, and D. R. Phillips, *Phys. Rev. C* **89**, 024613 (2014).
- [314] X. Zhang, K. M. Nollett, and D. R. Phillips, *Phys. Rev. C* **89**, 051602 (2014).
- [315] V. Datar, D. Chakrabarty, S. Kumar, V. Nanal, S. Pastore, *et al.*, *Phys. Rev. Lett.* **111**, 062502 (2013).
- [316] C. Cockrell, J. P. Vary, and P. Maris, *Phys. Rev. C* **86**, 034325 (2012).
- [317] E. A. McCutchan, C. J. Lister, R. B. Wiringa, S. C. Pieper, D. Seweryniak, J. P. Greene, M. P. Carpenter, C. J. Chiara, R. V. F. Janssens, T. L. Khoo, T. Lauritsen, I. Stefanescu, and S. Zhu, *Phys. Rev. Lett.* **103**, 192501 (2009).
- [318] L. Liu, T. Otsuka, N. Shimizu, Y. Utsuno, and R. Roth, *Phys. Rev. C* **86**, 014302 (2012).
- [319] E. McCutchan, C. Lister, S. C. Pieper, R. Wiringa, D. Seweryniak, *et al.*, *Phys. Rev. C* **86**, 014312 (2012).
- [320] P. Maris, J. Vary, A. Calci, J. Langhammer, S. Binder, *et al.*, (2014), arXiv:1405.1331 [nucl-th] .
- [321] S. Pastore, S. C. Pieper, R. Schiavilla, and R. Wiringa, (2014), arXiv:1406.2343 [nucl-th] .
- [322] E. Ricard-McCutchan *et al.*, TRIUMF proposal No. S1545 (2014).
- [323] J. Dohet-Eraly and D. Baye, *Phys. Rev. C* **88**, 024602 (2013).